INVERSION OF ACOUSTIC WAVEFORMS FOR VELOCITY AND ATTENUATION

A DISSERTATION SUBMITTED TO THE GRADUATE DIVISION OF THE UNIVERSITY OF HAWAI'I IN PARTIAL FULFILLMENT OF THE REQUIREMENTS FOR THE DEGREE OF

DOCTOR OF PHILOSOPHY

IN

GEOLOGY AND GEOPHYSICS

DECEMBER 1999

By

Xinhua Sun

Dissertation Committee:

L.Neil Frazer, Chairperson
Fred K. Duennebier
Gerard J. Fryer
Roy H. Wilkens
Xiaoming Tang
Eric Firing

We certify that we have read this dissertation and that, in our opinion, it is satisfactory in scope and quality as a dissertation for the degree of Doctor of Philosophy in Geology and Geophysics.

DISSERTATION COMMITTEE

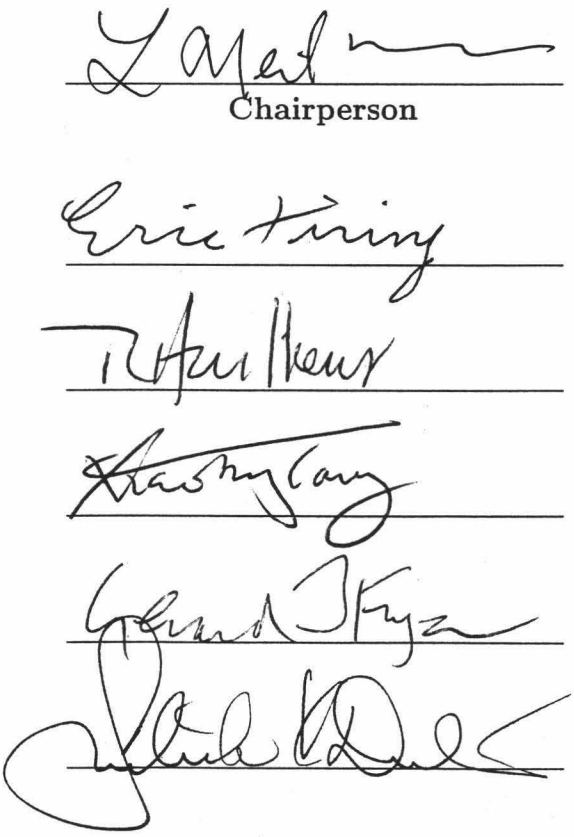

Chairperson

ACKNOWLEDGMENTS

I would like to thank my advisor Professor L. Neil Frazer for all his guidance, patience and for all of the things he taught me about science. It is his support and encouragement that sustain me throughout these years. I also thank Dr. Roy Wilkens for his advice, support, and offering me an opportunity to visit the Earth Resources Laboratory at Massachusetts Institute of Technology in 1994, which makes me interested in borehole acoustics.

I wish to thank the departmental professors for their invaluable classes. Professor Fred Duennebier and the late Professor Eduard Berg taught me a great deal of geophysical theory. I thank Fred for his working on my committee and for his helpful comments and encouragement.

Thanks also go to Drs. Gerard Fryer and Eric Firing for their expert guidance and for their work on my committee.

Finally, I gratefully acknowledge Baker Atlas Logging Services for the opportunity to spend a half year (1998) working with Drs. Arthur Cheng and Xiaoming Tang. I thank them for their support and interest in my work, and I thank Xiaoming for his willingness to be a member of my dissertation committee.

ABSTRACT

In this dissertation, I present some new schemes and techniques for processing of acoustic waveform data. New objective functions are developed for waveform inversion. I use synthetic acoustic borehole waveform data to demonstrate their novel features. These schemes require neither prior deconvolution nor knowledge of the source-receiver wavelet. The most powerful of them is the fourwise processor, which is applicable to data sets from multiple shots and receivers even when each shot has a different unknown signature and each receiver has a different unknown impulse response. I apply this scheme to inversion for shear wave velocity from the ODP sonic data measured by an LSS tool, containing two uncalibrated transmitters and receivers. A 3-D search of waveform inversion gives stable results of formation S-wave velocity inverted from the monopole sonic data in a slow formation.

In addition, I develop new techniques to extract P- and S-wave attenuation from sonic logging data. The success of the techniques lies in the separation of attenuation-related wave attributes from other effects unrelated to attenuation. The wave attributes related to borehole diameter, formation density, and velocity changes are removed by use of synthetic sonograms. The novelty of the techniques is first to use a single receiver data set to extract a relative attenuation profile, then

to correct it to absolute attenuation using multiple receiver data sets. The techniques are applicable to both monopole and dipole waveform log data for either P- or S-wave attenuation.

TABLE OF CONTENTS

LIST OF FIGURES

Chapter 1
Introduction

Acoustic waveform processing is critical for quantitative and qualitative understanding of formation properties. The objective of this dissertation is to present some new schemes and techniques for processing acoustic waveform data.

In seismic surveys or acoustic well logging, a recorded waveform or seismogram is a convolution of a source function, a propagation function, and an instrument recording function. Of most interest to geophysicists is the propagation function because it is related to the earth formation properties. Waveform inversion provides an effective means to extract the earth formation parameters from the waveform data.

Let the vector $\mathbf{m}$ represent the earth model parameters. These parameters may not all be directly measurable. We can operationally define some observable parameters whose actual values hopefully depend on the values of the model parameters. To solve the forward problem, we predict the values of the observable parameters, beginning with arbitrary values of the model parameters. To solve the inverse problem, we infer the values of the model parameters from observed values of the observable parameters.

The goal of waveform inversion is to infer the values of the formation parameters from the observed waveform data. The problem with most inversion schemes is that the observed waveform data depend not only on the values of the formation parameters but also on the source-receiver wavelets. In other words, different source-receiver wavelets generate different waveforms even if the values of the earth formation parameters are kept identical. Occasionally, the source-receiver wavelet is known in the waveform. For this case, the observed waveform data set can usually be treated as an overdetermined problem to solve for the formation parameters, pro-

vided the number of the unknown formation parameters is less than that of observed waveform data. In many cases, the source-receiver wavelet is taken to be identical in each waveform but it is unknown. Those cases are often handled as overdetermination if the observed waveform data are redundant. This is because the number of unknown parameters including formation parameters and source-receiver wavelets is limited. In reality, the coupling between the transmitter or receiver and the earth changes with its position. On the other hand, the source signature or the receiver impulse response might not be the same for each source or each receiver. In other words, the source-receiver wavelet can not be assumed identical in each waveform. To recover formation parameters as well as the source wavelet, the receiver response and the coupling function is almost impossible due to the large number of unknowns. This is an underdetermined problem. Fortunately, we are not interested in the source wavelet, receiver impulse response, and coupling function. All we are interested in is the formation parameters.

Most geophysical inversion problems are of the mixed type, i.e. the observed data overdetermine some model parameters while leaving others underdetermined. In waveform inversion, the observed waveform data set usually overdetermines the formation parameters while the values of the wavelets of receiver, source, and coupling are underdetermined.

In seismic inversion, one usually begins with a waveform data set $\mathbf{d}$, a vector of earth model parameters $\mathbf{m_s}$, and an earth modeling algorithm $\mathbf{H}$ which generates the model response in the form of synthetic waveform $\mathbf{s} = \mathbf{H}(\mathbf{m_s})$. Inversion proceeds by searching for the value of $\mathbf{m_s}$ that makes synthetic data $\mathbf{s}$ agree with data $\mathbf{d}$. The degree of agreement of $\mathbf{s}$ and $\mathbf{d}$ is measured by a scalar objective function $\phi(\mathbf{d}, \mathbf{s})$ with values between zero and one. It can be seen that inversion has three independent elements: the earth modeling algorithm $\mathbf{H}$, the search algorithm used to vary parameter vector $\mathbf{m_s}$, and the choice of the objective function ϕ. Chapter 2 is concerned almost

exclusively with the last item, the definition of the objective function or processor. Three new objective functions were derived for waveform inversion. These objective functions are blind to the source-receiver functions. One need not consider what the source and receiver functions are during inversion. The variation of the source and receiver functions with their positions due to coupling is also accounted for. Although these processors were developed in response of a problem that arose in the inversion of acoustic waveform logging data, they are also applicable to other waveform inversion problems.

Chapter 3 concerns the application of the fourwise processor to the inversion for S-wave velocity from ODP sonic data. The waveform data were measured by the Schlumberger Long Spaced Sonic (LSS) tool with two transmitter and two receiver pairs. The two source functions and the two receiver functions in the waveform data are not consistent with each other. Because of the slow formation environment, there are no directly refracted S-wave arrivals in the waveform data and the S-wave velocity must be obtained from inversion. A 3-D search has been used to extract S-wave velocity from the ODP sonic data in marine soft sediments. Three parameters, formation S-wave and P-wave velocities, as well as sonic borehole radius, were simultaneously inverted from the four waveforms at one depth. The details of inversion for S-wave velocity are discussed there.

Chapters 4, 5 and 6 are concerned with the extraction of formation intrinsic attenuations from acoustic waveform logging data. Wave amplitudes through an inelastic medium decrease during outward propagation due to two major causes: geometrical spreading as the area of the entire wavefront expands, and intrinsic attenuation attributed to dissipational mechanisms that convert elastic wave energy to heat. A dimensionless quantity, called quality factor Q, is used to measure the

intrinsic attenuation

$$\frac{1}{Q} = -\frac{1}{2\pi}\frac{\Delta E}{E} \tag{1}$$

where ΔE is the loss of strain energy in one cycle of wave oscillation, the loss being caused by the imperfection in the elasticity of the medium; E is the peak strain energy stored in one cycle. For a medium with a linear stress-strain relation, wave amplitude A is proportional to $E^{\frac{1}{2}}$. In terms of wave amplitude, Q is also written as

$$\frac{1}{Q} = -\frac{1}{\pi}\frac{\Delta A}{A} \tag{2}$$

where ΔA is the decrease in amplitude over one cycle, and A is the maximum amplitude during the cycle. Q can denote the quality factor for either P- or S-wave.

Chapter 4 is focused on how to extract P-wave attenuation from ODP sonic waveform logging data measured in soft marine sediments with the LSS tool. Conventional methods of extraction of P-wave attenuation from acoustic waveform logging data were unsuccessful on our ODP sonic waveform logging data. The reasons for their failure on our data set are discussed in Chapter 4. A robust scheme for the extraction of relative intrinsic P-wave attenuation and its application to ODP sonic waveform data processing are presented also in Chapter 4. P-wave attenuation profiles at ODP sites 806 and 807 are obtained from the data.

Chapter 5 presents a modification of the method presented in Chapter 4. The reason why the original method does not work for the data measured in fast formations is explained in this Chapter. Also described in some detail are effects of window size, borehole fluid velocity, source-receiver offsets and source wavelets etc. on the results of derived attenuation. Applications of the modified method to both P- and S-wave attenuation estimations are also presented.

Attenuation characteristics reveal much information, such as lithology, physical state, and degree of saturation of rocks. The phenomenon of attenuation is much more complex than the elastic aspects of seismic wave propagation. In Chapter 5, in-situ

P- and S-wave attenuation profiles and their comparisons are presented for three oil reservoirs. Their correlations with formation lithology, permeability, and fractures are also presented.

In Chapter 6, the appropriate method for estimating shear wave attenuation from acoustic dipole logging data is proposed. Synthetic tests and applications to the field data are presented and comparisons between the S-wave attenuation profiles from both the monopole waveform data and the dipole waveform data are also described.

Chapter 2
New objective functions for waveform inversion

2.1 SUMMARY

Unknown source-receiver wavelets make waveform inversion complicated or even difficult. Here three new objective functions, which I refer to as processors, are derived. Using these processors, neither prior deconvolution nor knowledge of the source-receive wavelet is required in the waveform inversion.

The *pairwise* processor is applicable to a data set consisting of two or more traces with the same unknown wavelet but possibly different gains. The *fourwise* processor is applicable to data sets from multiple shots and receivers even when each shot has a different unknown signature and each receiver has a different unknown impulse response. When only one seismogram exists, the *partition* processor can be used. It is also applicable when there is only one shot(receiver) and each receiver(shot) has a different signature.

2.2 INTRODUCTION

A seismogram is a convolution of source wavelet, formation response and receiver impulse response. In the frequency domain, it can be expressed as the product of the source and receiver spectra and the Green's function of propagation. The most useful information of the seismogram is the Green's function of propagation, which is a function of formation parameters. Inversion provides an effective means to extract the formation parameters from seismograms. However, the unknown source wavelet and receiver impulse response make it complicated or even difficult to extract the pa-

rameters from the seismogram. The problem at hand arose from our Ocean Drilling Program (ODP) sonic waveform logging data. We tried to use these data to invert formation shear wave velocity. On the waveform, there is no directly refracted S-head wave because the formation S-wave velocity is less than the borehole fluid velocity. The problem with inversion is that the source-receiver wavelets in the waveforms are unknown because the two transmitters and two receivers on the LSS tool (shown in Figure 2.1) were uncalibrated. Figure 2.2 shows the four waveforms recorded at a depth of 200 meters below seafloor on ODP Site 806B. It can be seen that a significant difference exists between the two waveforms with the same source-receiver offset. This is because source wavelets or receiver responses are inconsistent. In response to this problem, the new objective functions, referred to here as processors, have been developed. In order to test the behavior of these processors, we use acoustic logging synthetic waveforms as an example. The main data application will be presented in Chapter 3. The synthetic waveforms were computed by the frequency-wavenumber method of Cheng (1989) with various enhancements such as causal attenuations and complex frequencies (Mallick and Frazer 1987), and Filon integration (Frazer and Gettrust 1984, Frazer 1988). Figure 2.3 shows two source-receiver wavelets and their spectra. Wavelet 1 is used below as a 'data' wavelet $b_d(t)$, while wavelet 2 is used as a 'guess' wavelet $b_s(t)$, sometimes referred to as the 'wrong' wavelet. Figure 2.4 shows synthetic waveforms made with the two different wavelets; it can be seen that at each distance the wavelet 1 waveform is quite different from the wavelet 2 waveform. The formation parameters used in synthetic waveforms, except for V_s, Q_s, and Q_{fl} which are guessed, are taken from an analysis of ODP data at hole 806B. They are: borehole radius 0.136 m; formation compressional velocity $V_p = 2.265$ km/s; borehole fluid velocity $V_{\text{fl}} = 1.5$ km/s; fluid density $\rho_{\text{fl}} = 1.0$ Mg/m^3; formation density $\rho = 1.834$ Mg/m^3; and formation compressional quality factor $Q_p = 25.45$. The formation shear quality factor Q_s is considered to be a half of Q_p. The fluid quality factor is guessed

as 150, because the sea water was used as a drilling mud. It is usually observed that the acoustic waveform propagating through the sea water is less attenuated.

In order to show the behavior of processors, a search for a single formation parameter, Poisson's ratio, is performed. It should be noted that in our earth model, the formation is slow because the formation S-wave velocity is less than the borehole fluid velocity. So the inversion for Poisson's ratio is a nontrivial process.

2.3 OBJECTIVE FUNCTIONS

Let D be the Fourier spectrum of a waveform(trace) which could be either synthetic or observed data with subscript *syn* or *dat*. The spectra of source wavelet and receiver response are denoted by T and R. G is formation Green's function. Their dependence of angular frequency ω is understood. For an earth model of $\mathbf{m}$, $D(\omega, \mathbf{m}) = T(\omega)R(\omega)G(\omega, \mathbf{m})$. In order to search for an earth model $\mathbf{m}$, we need define a measure as a processor giving a value between zero and one. The processor equals 1 indicates that the true earth model is found from the model space.

2.3.1 Conventional processor

Consider a comparison in the frequency domain between a synthetic and an observed data. Usually, an inner product is used. Let D_{syn} and D_{dat} be the spectra of synthetic and observed waveforms. The inner product is given by $\langle D_{syn}|D_{dat}\rangle_\chi = \sum_\omega \chi_\omega D_{syn}(\omega)\, D_{dat}(\omega)^*$, in which $\chi_\omega = \chi(\omega)$ is some positive real weight function satisfying $\sum_\omega \chi_\omega = 1$, and $D(\omega)^*$ is the complex conjugate of a spectrum $D(\omega)$. When D_{syn} is matched with D_{dat}, the module of the inner product reaches maximum.

A conventional processor for a single waveform is given by

$$\phi_1(\mathbf{m_s}) = \frac{|\langle D_{syn}|D_{dat}\rangle_\chi|^2}{\langle D_{syn}|D_{syn}\rangle_\chi \langle D_{dat}|D_{dat}\rangle_\chi}, \tag{1}$$

where $\chi(\omega)$ can be taken to be proportional to $|\frac{G(\mathbf{m_s}+\delta\mathbf{m_s},\omega)-G(\mathbf{m_s},\omega)}{G(\mathbf{m_s},\omega)}|$.

When and only when a searched earth model $\mathbf{m_s}$ is matched with the true earth model $\mathbf{m}$, the conventional processor ϕ_1 is equal to 1 provided that the source-receiver wavelet in the synthetic waveform is identical with that in the data trace. In reality, however, the source-receiver wavelet in the data trace is unknown and will, in general, vary with different traces. When the source-receiver wavelet in the synthetic trace is inconsistent with that in the data trace, the inverted earth model will be biased from the true earth model. Figure 2.5 shows that when the conventional processor reaches maximum, the wrong shear wave velocity is given if the wavelet in the synthetic waveforms mismatches that in the data trace. To solve this problem, the following processors are derived.

2.3.2 Pairwise processor

Suppose a receiver array data set with n receivers, each of which has the same property in the frequency domain, has the same unknown wavelet in terms of source and receiver. A source gather in the seismic survey will fall in this category provided their wavelets in the data set are the same. In reality, the wavelets are unknown.

The basic idea of the pairwise processor is to make two new pairs with the same source-receiver wavelets. Each of the new pairs consists of a synthetic trace and a data trace. To see why we can do so, suppose that we have two distinct source-receiver offset waveform data, say, D^i_{dat} and D^j_{dat}. We can make two synthetic traces D^i_{syn} and D^j_{syn}. It should be noted that the source-receiver wavelet in the synthetic traces might be different from that in the data traces because we do not exactly know what the wavelet in the data traces is. Combining a data trace with a synthetic trace, we have $F^{ij} = D^i_{dat}D^j_{syn}$. Similarly, we have another pair $F^{ji} = D^j_{dat}D^i_{syn}$. It can be seen that both F^{ij} and F^{ji} have the same term $(T_{syn}R_{syn}T_{dat}R_{dat})$ in relation to source

and receiver. If and only if $\mathbf{m_s}$ equals $\mathbf{m}$, $F^{ij} = F^{ji}$, provided the wavelet used in synthetics is in the same frequency band as the data trace. The pairwise processor can be defined as

$$\phi_2^{ij}(\mathbf{m_s}) = \frac{|\langle F^{ij}|F^{ji}\rangle_{\chi^{ij}}|^2}{\langle F^{ij}|F^{ij}\rangle_{\chi^{ij}}\langle F^{ji}|F^{ji}\rangle_{\chi^{ij}}}, \tag{2}$$

where χ^{ij} is a real positive weighting function of frequency. For multiple traces, the pairwise can be denoted as

$$\phi_2(\mathbf{m_s}) = |\sum_{i<j} \xi^{ij}\langle \hat{F}^{ij}|\hat{F}^{ji}\rangle_{\chi^{ij}}|^2 \tag{3}$$

where ξ^{ij} is an optional weighting function, $\sum_{i<j}\xi^{ij} = 1$, and the normalized spectrum $\hat{F}^{ij}$ is taken as $\frac{F^{ij}}{\sqrt{\langle F^{ij}|F^{ij}\rangle_{\chi^{ij}}}}$. It can be seen that when $\mathbf{m_s} = \mathbf{m}$, the pairwise equals 1. It is worthy of mention that we did not denote the pairwise processor for multiple traces as

$$\phi_2(\mathbf{m_s}) = \sum_{i<j} \xi^{ij}\phi_2^{ij}(\mathbf{m_s}). \tag{4}$$

This is because equation (4) usually has lower resolution on model parameters than equation (3). To see why it is, think about the case that suppose $\langle \hat{F}^{ij}|\hat{F}^{ji}\rangle_{\chi^{ij}} = \frac{1}{\sqrt{2}} + \frac{1}{\sqrt{2}}i$ and, $\langle \hat{F}^{ik}|\hat{F}^{ki}\rangle_{\chi^{ik}} = \frac{1}{\sqrt{2}} - \frac{1}{\sqrt{2}}i$, with the best choice of $\mathbf{m_s}$, then $\phi_2^{ij} = 1$ and $\phi_2^{ik} = 1$. Obviously, they are not fitting well. Taking an average weighting function, we can derive that equation (4) equals 1, while equation (3) equals 0.5. Equation (4) tells us that the fitting is perfect, while equation (3) tells us that the fitting is not perfect. Hence, equation (3) is better than equation (4).

The two right panels in Figure 2.6 show the results of processing with the pairwise processor. The 'data' were the same as those used for the conventional processor whose output is shown in the left panels. Comparison of panel (b) with the solid line in panel (a) shows that the pairwise processor has lower resolution on the model parameters, i.e., Poisson's ratio, than the conventional processor. This

is to be expected, as the pairwise processor has less information to work with than the conventional processor. On the other hand, comparison of panel (b) with panel (d) shows that the pairwise processor is nearly unchanged when the wrong wavelet is used. The small differences between panels (b) and (d) are due to the change in frequency weighting that results from a change of wavelet.

The pairwise processor does not need to know the source-receiver wavelet in the data trace. All that is required is that each data trace have the same source-receiver wavelet. In addition, the source-receiver wavelet used in synthetic traces should be in the same frequency band as those in data traces.

In real data, the source-receiver wavelet changes with different traces due to uncalibrated receivers or variation of coupling at the source or receiver to the formation. For instance, the Schlumberger LSS tool has two sources and two receivers. None are well calibrated. To solve such a problem, we developed the fourwise processor.

2.3.3 Fourwise processor

In a typical seismic surveying, multiple shots and multiple receivers are used. The source wavelet and receiver response may not be consistent across all traces due to changes of the coupling of the source and the receiver to the ground with their positions. In other words, the source wavelet and receiver response vary in each of the traces. To handle this case, the fourwise processor can be used. As shown schematically in Figure 2.7 we use indices i, j for sources and indices p, q for receivers. Thus the data trace D^{ip}_{dat} can be expressed as

$$D^{ip}_{dat} = T^{i}_{dat} R^{p}_{dat} G^{ip}(\mathbf{m}) \tag{5}$$

Then, we make four corresponding synthetic waveforms. Combining two data traces

with two synthetic traces, we have a new couple as the following

$$F_{pq}^{ij} = D_{dat}^{ip} D_{dat}^{jq} D_{syn}^{iq} D_{syn}^{jp} \tag{6}$$

$$F_{qp}^{ij} = D_{dat}^{iq} D_{dat}^{jp} D_{syn}^{ip} D_{syn}^{jq} \tag{7}$$

The terms regarding sources and receivers in both F_{qp}^{ij} and F_{pq}^{ij} are identical no matter what differences of the source and receiver wavelets in both data traces and synthetic traces are, provided the wavelets are located in the same frequency band. Like the pairwise processor, the fourwise processor for multiple traces is denoted as

$$\phi_4(\mathbf{m_s}) = \frac{|\sum_{p<q}^{i<j} \xi_{pq}^{ij} \langle \hat{F}_{pq}^{ij} | \hat{F}_{qp}^{ij} \rangle_{\chi_{pq}^{ij}}|^2}{(\sum_{p<q}^{i<j} \xi_{pq}^{ij})^2}. \tag{8}$$

For this processor the frequency weights χ_{pq}^{ij} should be a finite difference version of $|\partial_{m_k} \ln[G^{ip} G^{jq} G^{iq} G^{jp}|$, where m_k is the component of $\mathbf{m_s}$ to which increased sensitivity is sought.

Figure 2.8 shows the two transmitter signatures and two receiver impulse responses used to make the 'data' traces for testing. Each wavelet was minimum phase, with an amplitude spectrum generated by smoothing a sequence of random numbers from the uniform distribution on $[0, 1]$. The left column of Figure 2.9 shows the output of the conventional processor with the correct wavelets (upper panel) and wrong wavelets (lower panel). Wavelet 2 of Figure 2.9 was used as the wrong wavelet. As noted above, a fair comparison requires raising the output of the conventional processor to the fourth power. The right column of Figure 2.9 is similar to the left column, except that the fourwise processor was used. In these calculations the conventional processor had four terms in its summation whereas the fourwise processor had only one term. It can be seen that the conventional processor is considerably degraded by incorrect wavelets whereas the fourwise processor is hardly degraded at all by them. However, the fourwise processor has much lower resolution, as expected. From the

solid lines in Figure 2.9, it can be seen that the difference in resolution between the fourwise processor and the conventional processor is greater than the difference in resolution between the pairwise processor and the conventional processor. Thus, in general, the pairwise processor has greater resolution than the fourwise processor, a result expected from the fact that the pairwise processor has more information—it uses the important fact that the wavelet is the same on every waveform.

Figure 2.10 shows an example using real data from Ocean Drilling Project hole 806B. Densities, velocities and attenuations were the same as those used to compute the waveforms in Figure 2.4. In this example two of the offsets are the same, so two of the Green's functions are the same. In equation (6), the first and second factors in F_{pq}^{ij} were, respectively, the two ten-foot (3.05 m) source-receiver pairs, while the third and fourth terms were, respectively, the eight-foot (2.44 m) and twelve-foot (3.66 m) source-receiver pairs.

2.3.4 Partition processor

When a single waveform with unknown source-receiver wavelet is available, neither pairwise processor nor fourwise processor can be used for such a data set, because the pairwise processor requires that two waveforms have the same wavelets and the fourwise processor requires at least two sources and two receivers. The partition processor can be used for such a data set. A data set from one source and multiple receivers, each receiver with a different unknown impulse response, or from one receiver and multiple sources, each source with different unknown wavelet, belongs to this category.

Commonly, a seismogram has a time duration significantly longer than the source-receiver wavelet. Recall that a seismogram is a convolution of formation Green function response and the source-receiver wavelet. Thus it consists of a sequence of

replicas of the source-receiver wavelet, each replica having its own delay time and amplitude, possibly with its own phase shift. Thus we are able to separate it into two seismograms by windowing, each of them with the same source-receiver function $B(= TR)$, provided that appropriate windows are chosen. As shown on the left side of Figure 2.11, we multiply the seismogram separately by each window to get two new seismograms $d_1(t) = W_1(t)\, d(t)$ and $d_2(t) = W_2(t)\, d(t)$. Fourier transforming the new traces gives their spectra D_1 and D_2, as

$$D_i = B_{dat} G_i\,(\mathbf{m}); \qquad i = 1, 2. \tag{9}$$

It can be seen that Green's functions G_1 and G_2 in the two windowed seismograms differ from each other, because the two time window sizes are different. The two windows $W_1(t)$ and $W_2(t)$ may or may not overlap. Note that although G_1 and G_2 have the same argument $\mathbf{m}$, G_1 may be independent of some parameters in $\mathbf{m}$, while G_2 may be independent of other parameters in $\mathbf{m}$. It will be seen that, for any given component m_j of $\mathbf{m}$, if at least one of the G_i depends on m_j, then the value of m_j can be recovered by the procedure below.

Next we make a synthetic seismogram, with model vector, say, $\mathbf{m_s}$ and then use the synthetic seismogram to test whether $\mathbf{m_s} = \mathbf{m}$. The synthetic seismogram is

$$S = B_{syn}\, G_{syn}(\mathbf{m_s}), \tag{10}$$

in which B_{syn} is a bandpass filter that includes the band of the data. We window the synthetic seismogram in the same manner as the actual seismogram to obtain two synthetic seismograms S_1 and S_2, given by

$$S_i = B_{syn} G_{si}, \qquad i = 1, 2; \tag{11}$$

where, G_{si} is the Green's function for interval i and the trial value $\mathbf{m_s}$ of the parameter vector.

We now have two data spectra D_1 and D_2 and their two corresponding synthetic spectra S_1 and S_2. To obtain the partition processor, we apply the same principle that was used to get the pairwise processor. We multiply the spectrum of the first data trace by the spectrum of the second synthetic trace to get the spectrum of the first mixed trace, $F_1 = D_1 S_2$, and similarly to get the second mixed trace, $F_2 = D_2 S_1$. To a good approximation, the two mixed traces have the same unknown wavelet spectrum $B_{dat}B_{syn}$, and they agree with each other only if $\mathbf{m_s}$ equals $\mathbf{m}$. Hence we seek the earth model $\mathbf{m_s}$ that maximizes the agreement of F_1 and F_2. A partition processor for a single trace is

$$\phi_{\frac{1}{2},1}(\mathbf{m_s}) = |\langle \hat{F}_1 | \hat{F}_2 \rangle_\chi|^2. \tag{12}$$

Figure 2.12 compares conventional processing with partition processing for a single trace, and for a data set consisting of three traces at different offsets. The weight function used in the partition processor was a finite difference approximation of $\chi(\omega) = |\partial_\sigma \ln[G(\mathbf{m_s}, \omega)]|$. It can be seen, as expected, that the partition processor has lower resolution than the conventional processor, but that the conventional processor is biased by an incorrect guess at the unknown wavelet. If there are multiple traces, each with a different wavelet, then $\phi_{\frac{1}{2},1}$ can be applied to each trace separately and the outputs averaged—these are the dashed lines shown on the right panels of Figure 2.12—but it is better to combine the inversions at an earlier stage. A processor that does this is

$$\phi_{\frac{1}{2}}(\mathbf{m_s}) = \frac{|\sum_j \xi^j \langle \hat{F}_1^j | \hat{F}_2^j \rangle_\chi|^2}{(\sum_j \xi^j)^2}, \tag{13}$$

in which $\hat{F}_1^j$ and $\hat{F}_2^j$ are the normalized mixed traces corresponding to data trace j, and the ξ^j are optional real trace weights. Results from $\phi_{\frac{1}{2}}$ are the solid lines on the right side of Figure 2.11.

2.4 DISCUSSION AND CONCLUSIONS

The proposed three new processors can, in theory, eliminate the effect of unknown source-receiver wavelets on the waveform inversion, the loss of information from the data due to the band-limiting effect of the source-receiver wavelet may not, to some extent, be fully recovered, because the data are contaminated with noise and band-limited by the source-receiver response.

In addition, all three processors have different resolutions to the parameters to be searched. From this point, the pairwise processor is better than the fourwise processor. But the fourwise processor is more appropriate to the real case than the pairwise processor. The resolution of the partition processor depends on Green's functions and wavelets. Not all cases can the partition be used. It requires that the window length be approximately equal to that of the source-receiver wavelet in the waveform. Furthermore, the waveform has a significant separation at the window cut. In other words, some of the problems can be solved by the partition procedure even if the source-receiver wavelet is unknown.

In summary, if there is just one seismogram for an event of unknown source spectrum, recorded by an instrument of unknown transfer function, then the partition procedure can be used to invert for unknown parameters provided the source-receiver wavelet is shorter in time than the Green's function of the seismogram. No minimum phase assumption is required. Similarly, if one event, with unknown source spectrum, is recorded by a receiver array (number of the receivers ≥ 2) with the same (unknown) transfer function, then the pairwise procedure can be used. Finally, for ≥ 2 events with different unknown transfer functions, then the fourwise procedure can be used. In the pairwise and fourwise procedures there is no limit on source-receiver signature length.

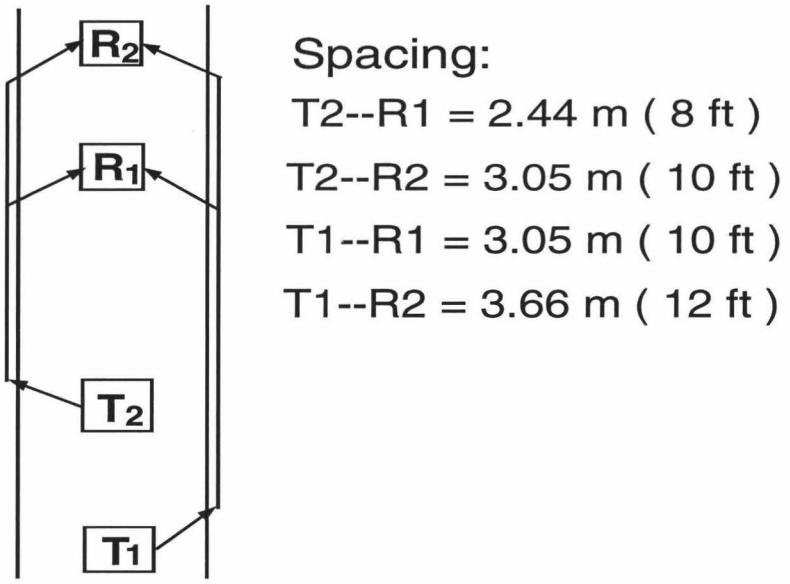

Figure 2.1: Schematic diagram of Schlumberger long spaced sonic tool with two transmitters and two receivers.

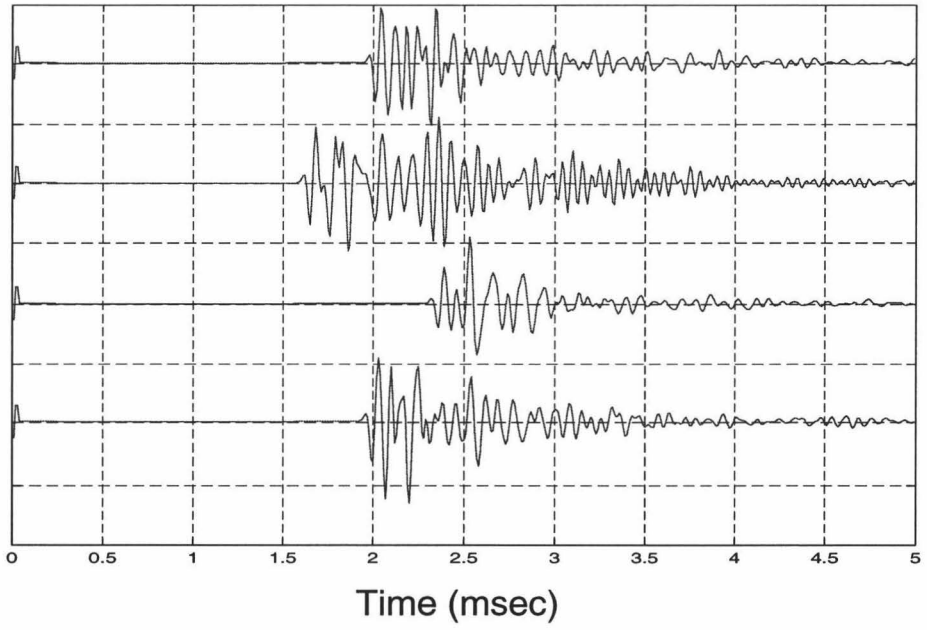

Figure 2.2: Waveforms recorded with an LSS tool at depth 200 meters below seafloor on ODP site 806B. From top to bottom, traces are 10, 8, 12, and 10 ft source-receiver offset waveforms, respectively.

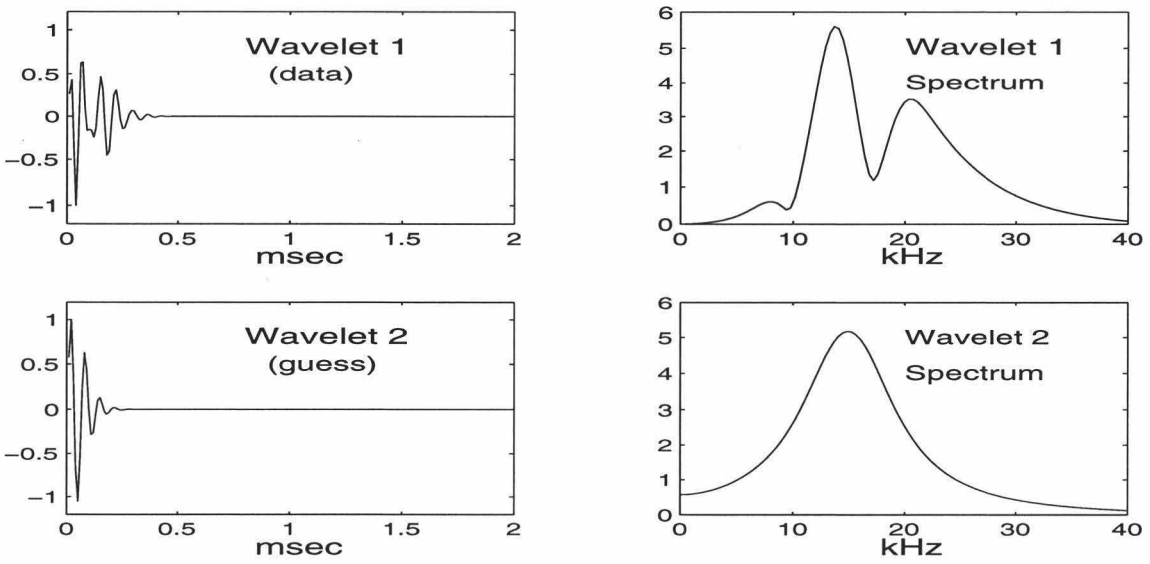

Figure 2.3: Two different source-receiver wavelets to be used in synthetics.

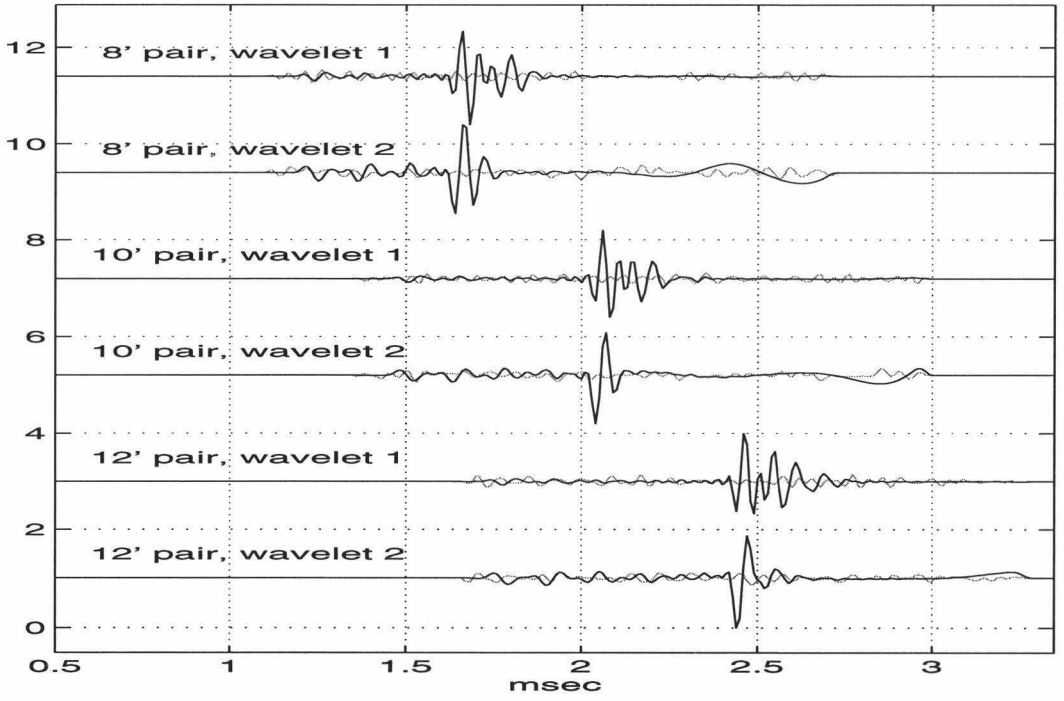

Figure 2.4: Synthetic waveforms for source-receiver offset 8, 10, and 12 ft. with two different source-receiver wavelets. The dotted lines are the 15% colored noise added to synthetic waveforms before processing experiments.

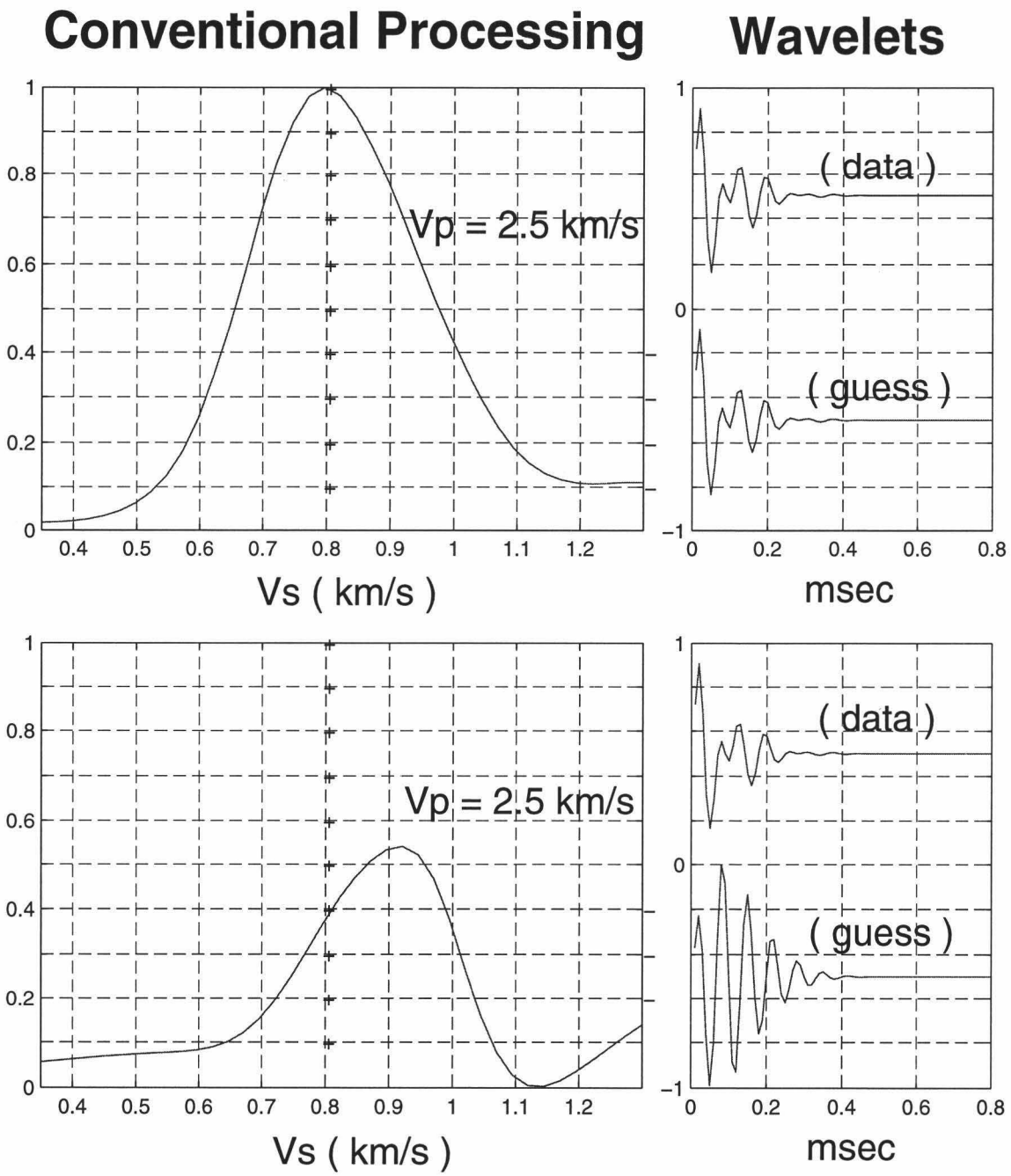

Figure 2.5: The upper panel shows that the conventional processor gives a true value of the searched v_S, only if the (guess) wavelet in the synthetic data is identical to that in the data. If the (guess) wavelet in the synthetic is inconsistent with that in the data (in the lower panel), the v_S inverted by the conventional processor is biased from the true value.

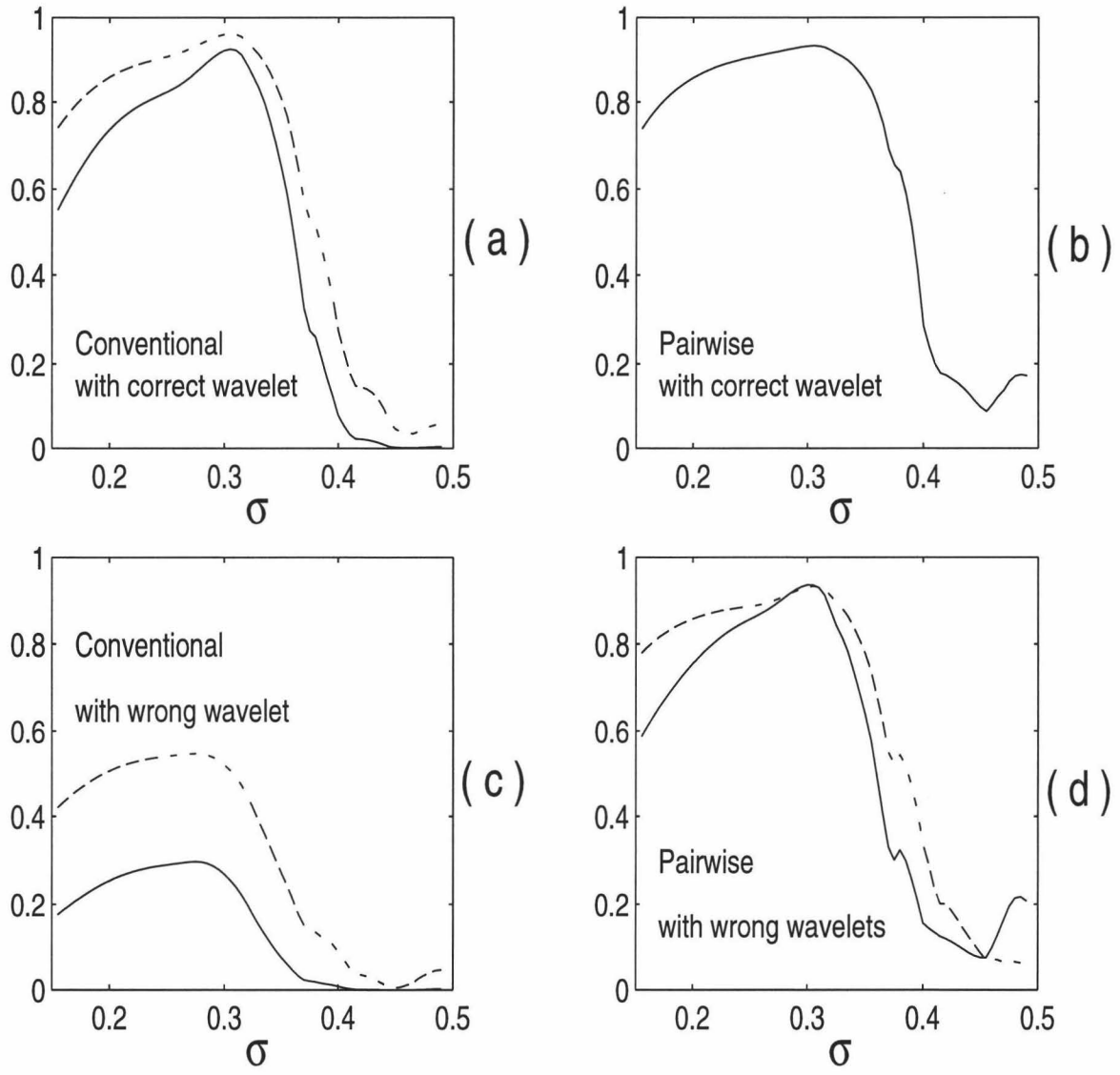

Figure 2.6: Comparison of pairwise processing with conventional processing. (a) Conventional processing with the correct source wavelet (wavelet # 1), and (c) with incorrect source wavelet (wavelet # 1 versus wavelet # 2); The dashed lines in both (a) and (c) are ϕ_1; the solid lines are $(\phi_1)^2$, comparative to the pairwise processor. (b) pairwise processing ϕ_2 (solid lines) with correct wavelet (# 1), and (d) with wrong wavelet (# 2). The dashed line in panel (d) is the result when a wavelet with a boxcar spectrum was used in the synthetic waveforms. Each processor used all three data traces(source-receiver offset 8, 10, and 12 ft). 15% colored noise was added to each data trace before processing.

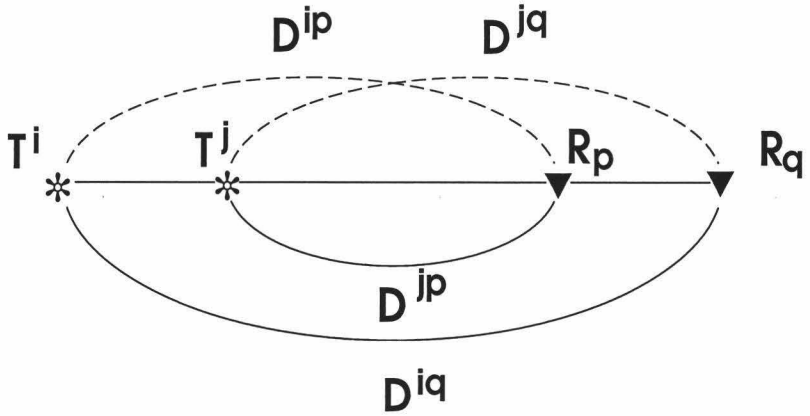

Figure 2.7: Comparison of the product of two upper trace spectra with that of two lower trace spectra. It is important to note that both products are identical with regard to source wavelets, receiver responses, and their couplings with formations.

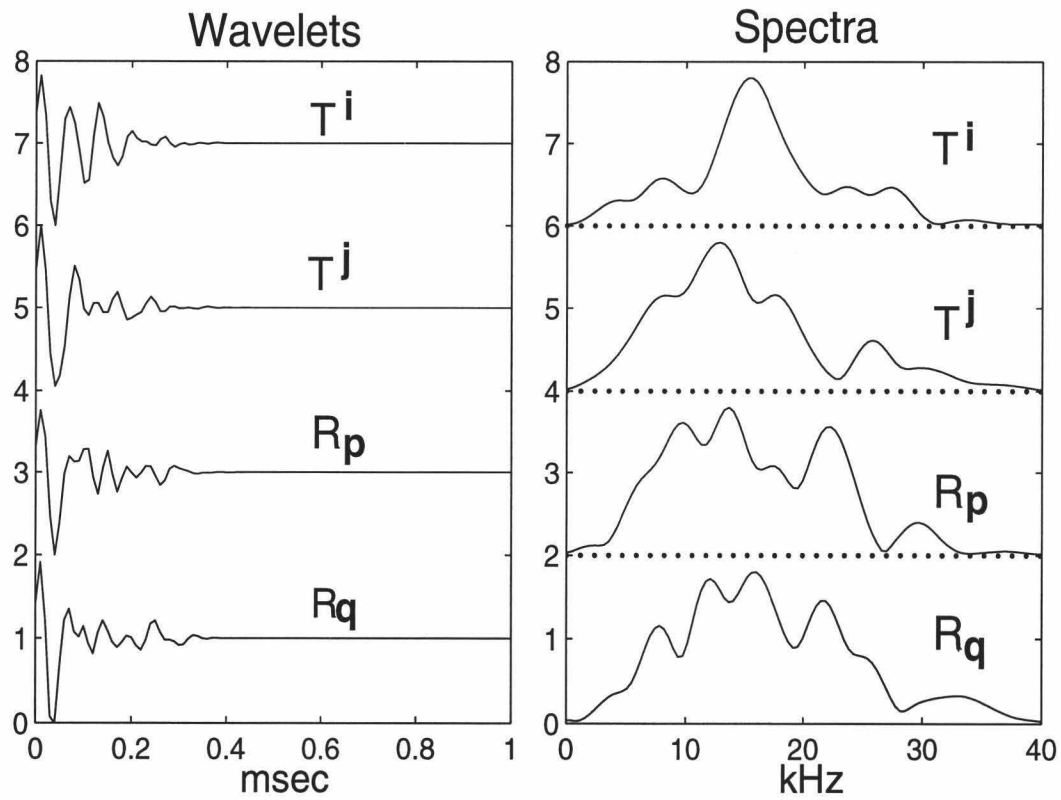

Figure 2.8: Source wavelets and receiver responses used to generate test data for the fourwise processor.

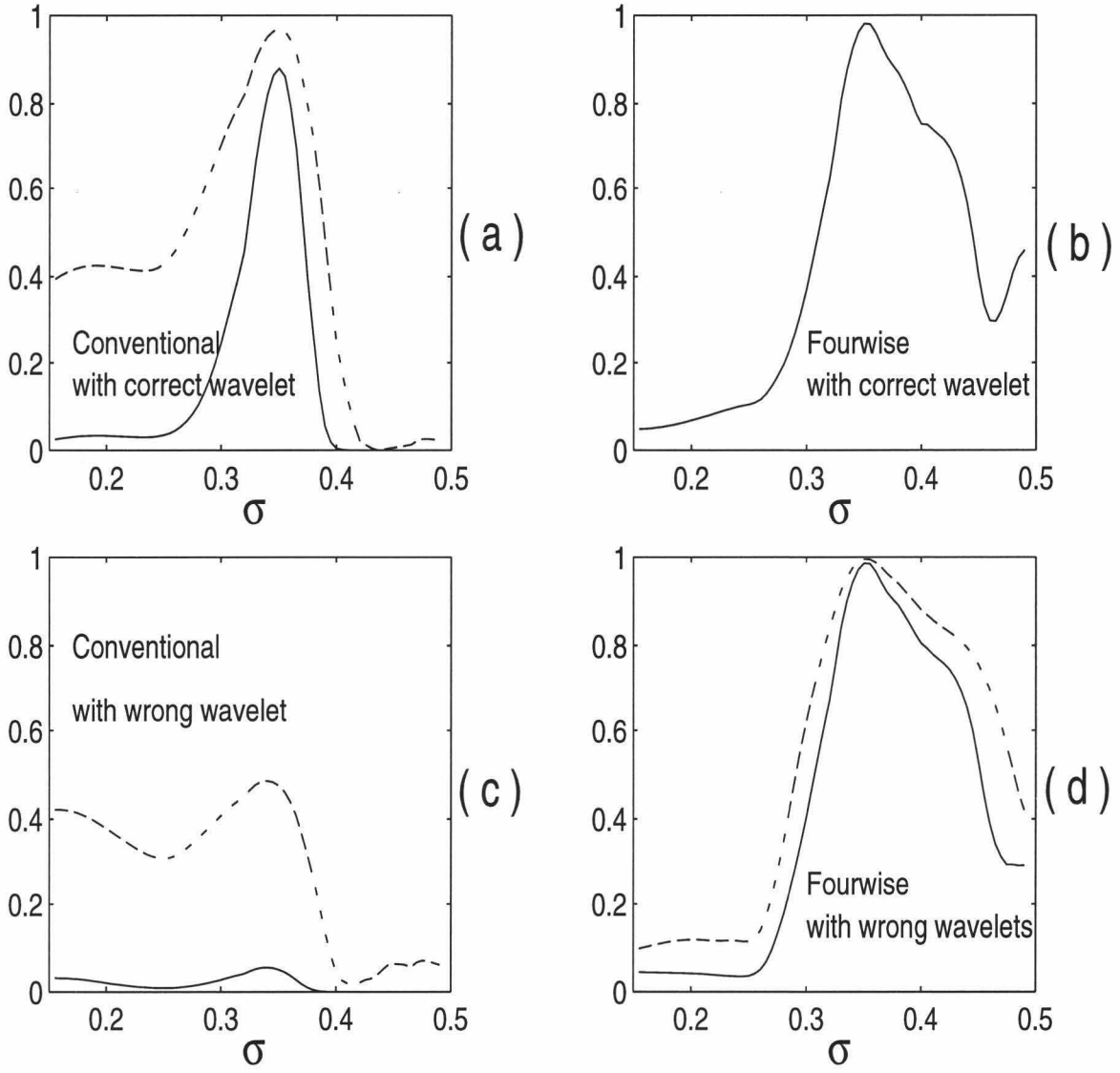

Figure 2.9: Comparison of fourwise processing with conventional processing. (a) Conventional processing with the correct source wavelet (wavelet # 1), and (c) with incorrect source wavelet (wavelet # 1 versus wavelet # 2); The dashed lines in both (a) and (c) are ϕ_1; the solid lines are $(\phi_1)^4$, for comparison to the fourwise processor. (b) fourth processing ϕ_4 (solid lines) with correct wavelet (# 1), and (d) with wrong wavelet (# 2). The dashed line in panel (d) is the result when a wavelet with a boxcar spectrum was used in the synthetics. Each processor used all three data traces. We also added 15% colored noise to each data trace before processing.

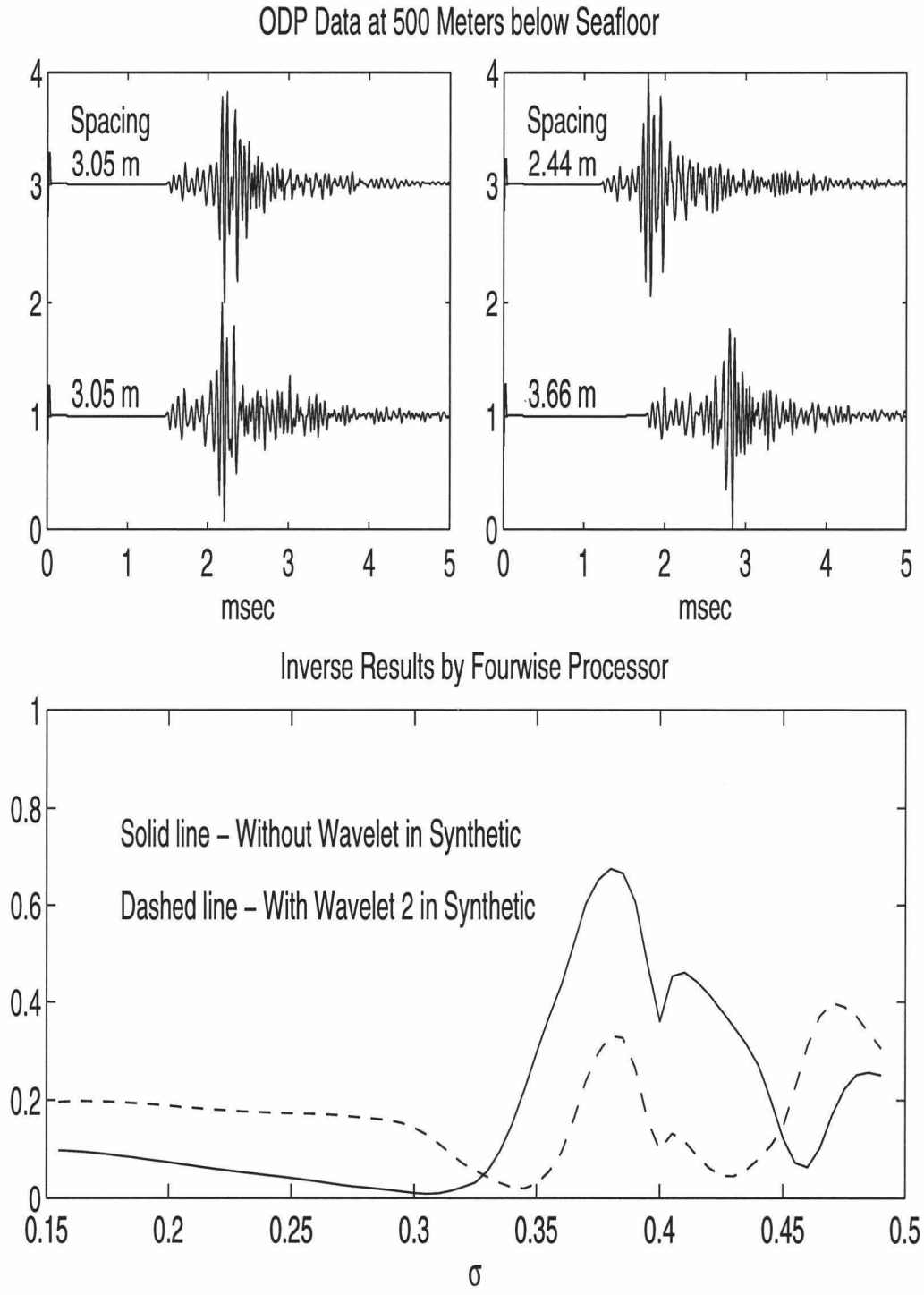

Figure 2.10: An example of the fourwise processing of the ODP hole 806B data. The inverted Poisson's ratio is around 0.37.

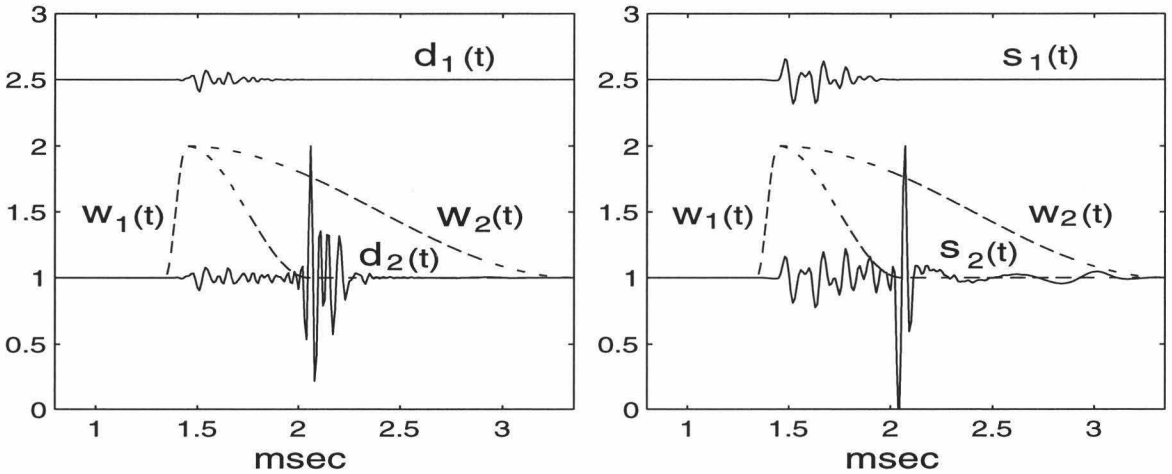

Figure 2.11: Schematic of partition processor. Two windows are used for both synthetic and data traces. The upper traces display the waveforms after using window 1, the lower traces are the waveforms after using window 2.

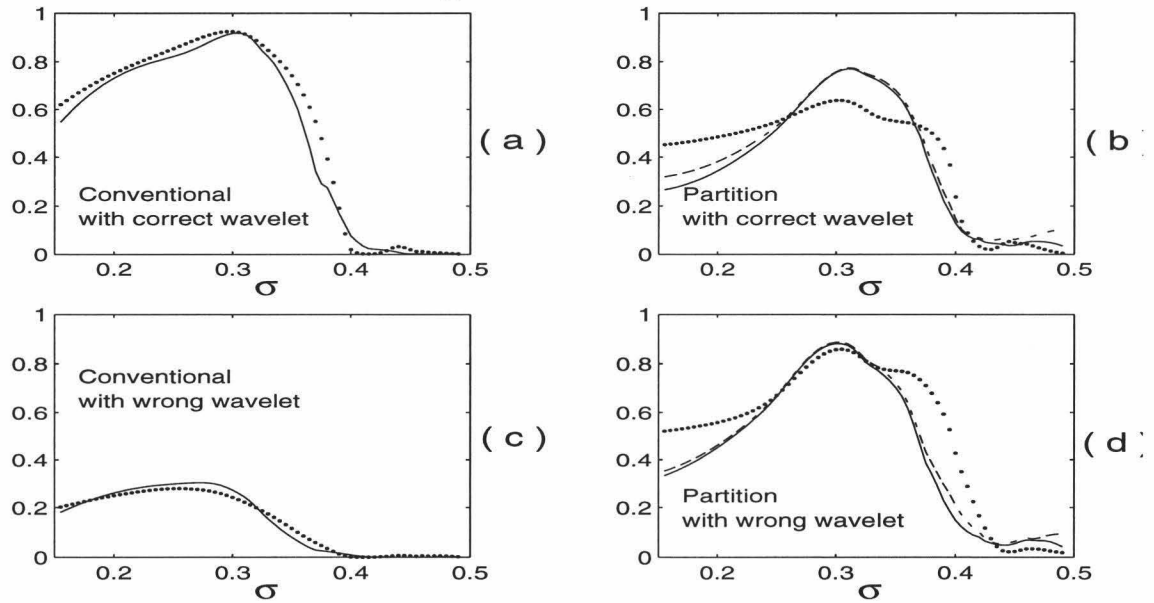

Figure 2.12: Comparison of partition processing with conventional processing. (a) Conventional processing with the correct source wavelet (wavelet # 1), and (c) with incorrect source wavelet (wavelet # 1 versus wavelet # 2); In the left column, the dotted lines are the results calculated with signal trace from the source-receiver offset 10 ft by ϕ_1; the solid lines are the results calculated with three different source-receiver offset (8,10, and 12 ft) traces by ϕ_1. In the right column, (b) partition processing $\phi_{\frac{1}{2}}$ (solid lines) with correct wavelet (# 1), and (d) with wrong wavelet (# 2), the dotted lines are the results calculated from single trace, the dashed lines are the results of averaged $\phi_{\frac{1}{2}}$ from three different source-receiver offset traces, and the solid lines are the results calculated from three different traces simultaneously. All of the data traces were added by 15% colored noise before processing.

2.5 REFERENCES

Cheng, C. H., 1989, Full waveform inversion of P-waves for V_s and Q_p, *J. Geophys. Res.*, **94**, 15,619-15626.

Frazer, L. N., 1988, Quadrature of wavenumber integrals, *in* Doornbos, D. J., Ed., Seismological Algorithms: Academic Press Inc.

Frazer, L. N., Sun, X.,1998, New objective functions for waveform inversion: *Geophysics*, **63**, 213-222.

Frazer, L. N., Sun, X., and Wilkens, R. H., 1997, Inversion of sonic waveforms with unknown source and receiver functions: *Geophys. J. Int.*,**129**, 579-586.

Mallick, S. and Frazer, L. N., 1987, Practical aspects of reflectivity modeling: *Geophysics*, **52**, 1355-1364.

Chapter 3
Inversion for S-wave velocity from ODP sonic logging data

3.1 SUMMARY

A 3-D search of waveform inversion has been used to extract shear wave velocity from sonic logging data in marine soft sediments. S-wave and P-wave velocities as well as sonic borehole radius were simultaneously inverted from the four waveforms at each depth. A priori information for P-wave velocity and sonic borehole radius R as well as a weighting sensitive to S-wave velocity were used in the objective function to enhance the resolution of S-wave velocity. Applications of the algorithm to synthetic data produce v_S, v_P and R close to true parameters. Our results show that inversion of sonic data with a properly designed objective function can extract S-wave velocity from monopole waveform data even in slow formations.

The technique used here is fourwise processing(Frazer and Sun, 1998), which does not require estimates of the source and receiver transfer functions, and allows the source-receiver transfer functions to be different for different source-receiver pairs. The fourwise scheme thus allows variation with depth, as would be expected from changes of coupling with depth in the hole.

Although our algorithm was developed with the reference to Schlumberger Long Spaced Sonic tool (LSS) used in the Ocean Drilling Program operations, the method is applicable to other waveform inversion problems.

3.2 INTRODUCTION

Tools such as the Schlumberger Long Spaced Sonic tool (LSS), with just a few

monopole sources and receivers, are still used in the Ocean Drilling Program. The sources and receivers in the LSS tool are uncalibrated, and the frequency band is not low enough to include significant Stoneley wave energy. Figure 3.1 shows four waveforms and their amplitude spectra at depth 615 mbsf (meters below sea floor). In a soft formation, such as ocean bottom sediments, S-wave velocity is less than the borehole fluid velocity, and there is no directly refracted S-wave arrival on waveforms excited by a monopole source. Thus it is difficult to extract S-wave velocities of soft formations from LSS data.

Nevertheless, Toksöz, Wilkens & Cheng (1985) demonstrated the possibility of inverting for S-wave velocity v_s and for compressional attenuation Q_P^{-1} in a slow formation. They utilized the complete P-wavetrain, whose coda is rich in shear-sensitive PL waves, extracting formation parameters by comparison with synthetic seismograms. Their technique requires accurate estimates of source wavelets and receiver transfer functions. Stevens and Day (1986) used Stoneley waves in the 1-3 kHz band to extract S-wave velocity from a monopole source with two receivers; in their technique the transfer functions of the two receivers must be identical, and the source-receiver transfer function is estimated from the data by deconvolution. Cheng (1989) compared the spectral ratio of the P-wave trains at two different receivers with an analogous spectral ratio for synthetic seismograms; agreement of the data ratio with the synthetic ratio was maximized with respect to v_s and Q_P to find their actual values. Although Cheng's spectral ratio eliminates the effects of the unknown source spectrum, it requires that the two receiver transfer functions be identical.

The technique outlined below is based on fourwise processing (Frazer and Sun, 1998). Multiple forms of fourwise processing were developed for the LSS data. Like the original fourwise technique, all of them are blind to the source wavelet and receiver transfer function. Secondly, a 3-D search of waveform inversion was used in order to obtain a stable result of v_s. We demonstrate this technique first with synthetic

waveform data, and then apply it to field data.

3.3 THEORY

Let the transfer functions of the two transmitters be, T_1 and T_2, and the transfer functions of the two receivers be, R_1 and R_2. The transmitter and receiver coupling functions in the borehole are denoted by C_T and C_R respectively, which are believed to change with both frequency and depth. For later convenience, the borehole transfer function is given as $B = TC_TRC_R$. Hence the spectra of the four source-receiver pairs are

$$\begin{aligned} S_{d_1}(f, m_d) &= T_1(f)C_{T_1}(f, z_{T_1})G_{10}(f, m_d)C_{R_1}(f, z_{R_1})R_1(f), \\ S_{d_2}(f, m_d) &= T_2(f)C_{T_2}(f, z_{T_2})G_{8}(f, m_d)C_{R_1}(f, z_{R_1})R_1(f), \\ S_{d_3}(f, m_d) &= T_1(f)C_{T_1}(f, z_{T_1})G_{12}(f, m_d)C_{R_2}(f, z_{R_2})R_2(f), \\ S_{d_4}(f, m_d) &= T_2(f)C_{T_2}(f, z_{T_2})G_{10}(f, m_d)C_{R_2}(f, z_{R_2})R_2(f), \end{aligned} \tag{1}$$

where G is the Green's function of both the frequency (f) and the parameters (m_d) for the borehole and formation. A subscript 8, 10, or 12 on G indicates the distance between the transmitter and the receiver is 8, 10, or 12 feet, respectively. The coupling functions C_{T_i} for the transmitters and C_{R_i} for the receivers are here treated as functions of depth (z) and frequency (f). It is apparent that the borehole transfer functions $(B_{ij} = T_iC_{T_i}R_jC_{R_j}; i, j = 1, 2)$ in the four spectra are not identical. Therefore it is incorrect to simplify our problem by omitting coupling effects and assuming two receiver transfer functions or two source transfer functions to be identical. The difference of either two receiver or two source transfer functions in our problem can not be ignored, otherwise the wrong information about formation S-wave velocity may be obtained from our ODP data set. Moreover, since there is neither direct arrival of the shear wave, nor the Stoneley wave, it is very difficult to extract the S-wave velocity from the waveforms in soft formations by conventional methods. We

use the following procedure to overcome these difficulties due to the differences among transmitters and the two receivers. In the frequency domain, we take the products

$$\begin{aligned} X_{14} = \quad S_{d_1} S_{d_4} \quad &= B_{11} G_{10} B_{22} G_{10}, \\ X_{23} = \quad S_{d_2} S_{d_3} \quad &= B_{21} G_8 B_{12} G_{12}. \end{aligned} \tag{2}$$

Notice that the transmitter-receiver factors in X_{14} and X_{23} are identical because

$$B_{11} B_{22} = B_{21} B_{12} = T_1 C_{T_1} R_1 C_{R_1} T_2 C_{T_2} R_2 C_{R_2}. \tag{3}$$

Using synthetic Green's functions G_{s8}, G_{s10} and G_{s12} for 8, 10 and 12 foot pairs, we introduce the products

$$\begin{aligned} F1 \quad &= X_{14} G_{s8}(m_s) G_{s12}(m_s), \\ F2 \quad &= X_{23} G_{s10}(m_s) G_{s10}(m_s). \end{aligned} \tag{4}$$

It can be seen from equation (4) that if the synthetic Green's functions match those in the data, then F_1 and F_2 will be identical. Now, we introduce a scalar objective function $\phi(F_1, F_2)$ given by

$$\phi(F_1, F_2) = \frac{|\langle F_1 | F_2 \rangle|^2}{\langle F_1 | F_1 \rangle \langle F_2 | F_2 \rangle}, \tag{5}$$

where,

$$\langle F_i | F_j \rangle = \sum_f \chi(f) F_i(f) F_j^*(f), \quad i = (1,2); j = (1,2),$$

in which χ is a real weighting function, and F_j^* is the complex conjugate of the spectrum F_j.

Inversion proceeds by searching for the value of m_s that makes F_1 agree with F_2. The degree of agreement of F_1 and F_2 is given by the scalar objective function $\phi(F_1, F_2)$ with values between zero and one.

Our purpose is to extract the S-wave velocity of the formation from our ODP data set. However, the data are relatively insensitive to formation shear velocity, because the S-wave velocity is less than the borehole fluid velocity so that there is no

directly refracted S-wave on the waveform, and because the Stoneley waves are mostly missing within the frequency band of 5-25 kHz. In addition, the objective function $\phi(F_1, F_2)$ has a low sensitivity to parameter v_P/v_S , because each F_i includes four Green's functions. Furthermore, only one ϕ can be calculated from four waveforms at each depth. Therefore it is difficult to get a reliable estimate of v_s at each depth.

In order to improve the above situation, a few measures are taken during inversion. First of all, we construct multiple forms of F_1 and F_2 by transferring one term of either a synthetic Green's function or the data from F_1 or F_2 to F_2 or F_1, as in the following,

$$
\begin{array}{ll}
F_1 = S_{d_2} G_{s10} G_{s10}; & F_2 = S_{d_1} S_{d_4} G_{s8} G_{s12} / S_{d_3}, \quad (6.1) \\
F_1 = S_{d_3} G_{s10} G_{s10}; & F_2 = S_{d_1} S_{d_4} G_{s8} G_{s12} / S_{d_2}, \quad (6.2) \\
F_1 = S_{d_1} G_{s8} G_{s12}; & F_2 = S_{d_2} S_{d_3} G_{s10} G_{s10} / S_{d_4}, \quad (6.3) \\
F_1 = S_{d_4} G_{s8} G_{s12}; & F_2 = S_{d_2} S_{d_3} G_{s10} G_{s10} / S_{d_1}, \quad (6.4) \\
F_1 = S_{d_1} S_{d_4} G_{s12}; & F_2 = S_{d_2} S_{d_3} G_{s10} G_{s10} / G_{s8}, \quad (6.5) \\
F_1 = S_{d_1} S_{d_4} G_{s8}; & F_2 = S_{d_2} S_{d_3} G_{s10} G_{s10} / G_{s12}, \quad (6.6) \\
F_1 = S_{d_2} S_{d_3} G_{s10}; & F_2 = S_{d_1} S_{d_4} G_{s8} G_{s12} / G_{s10}; \quad (6.7) \\
F_1 = S_{d_2} S_{d_3} G_{s10} G_{s10}; & F_2 = S_{d_1} S_{d_4} G_{s8} G_{s12}; \quad (6.8)
\end{array}
\tag{6}
$$

The purpose of making multiple pairs is to enhance the resolution of objective functions to v_s by reducing the number of Green's functions in each pair. One can generate of other forms of F_i by dividing two or more terms of synthetic Green's functions or data. The problem is that the error of the objective functions to the unknown parameter $v_s$is increased by dividing. Spectral division is always unstable. The trade-off between the parameter resolutions and the error depends on our field data set. We found from our field data processing that the error in the inverted v_s is, to a great extent, increased over most of the depth range by using the forms of F_i with two terms in the denominator. That is why each pair of F_i, which we will use for inversion of v_s, is at most allowed to be divided by one term.

It is easy to see that F_1 and F_2 in each pair are equal if $\bar{m}_s$ matches $\bar{m}_d$. Thus, by comparing F_1 with F_2, we can find $\bar{m}_d$.

In practice, the data are always contaminated by noise. Hence noise was added to the synthetic data used for testing.

Using the above pairs of F_1 and F_2, we can calculate eight objective functions (i.e. $\phi_i : i = 1, \ldots, 8$) from the four waveforms at each depth. In order to enhance the sensitivity of the objective functions to v_S, we introduce different weighting functions for different pairs as

$$\chi_s = \frac{\partial_{m_k} \varphi(f, m_s)}{\varphi(f, m_s)} \tag{7}$$

where $\varphi = |G_{s8} G_{s10} G_{s12}|$ for pair 1, and $\varphi = |G_{s8} G_{s10} G_{s10} G_{s12}|$ for pair 2, etc. m_k is for v_P/v_S . In addition, we use the known v_P and sonic R as the a priori information by defining weighting functions χ_c for v_P , and χ_r for R,

$$\chi_c = \exp(-\frac{|v_P - v_P{}^{prior}|}{\sigma_c}); \qquad \chi_r = \exp(-\frac{|R - R^{prior}|}{\sigma_r}), \tag{8}$$

where $\sigma_c = 0.8$ and $\sigma_r = 0.2$. Figure 3.2 shows the weight functions of χ_c for v_P and χ_r for R. The total weighting function χ in the objective function is calculated by

$$\chi = \chi_s \chi_c \chi_r. \tag{9}$$

From each of the pairs of F_1 and F_2, we obtain the v_P , v_S, and R corresponding to a maximum of the objective function. The goodness of the estimates v_S^i, $(i = 1, \ldots, 8)$ depends on the value of the ϕ_i^{max}. Consequentially, we take a weighted average of all v_S^i as the solution of v_S,

$$v_S = \frac{\sum_i \phi_i^{max} v_S^i}{\sum_i \phi_i^{max}}. \tag{10}$$

Estimates of v_P and borehole radius R are obtained by similar procedures.

3.4 SYNTHETIC DATA TESTS

The method was first tested on synthetic data with added noise. The synthetic model consists of an axisymmetric fluid filled borehole, extended to infinity

in z-direction, embedded in an isotropic solid formation. The synthetic data were computed by the frequency-wavenumber method of Cheng(1989) with various enhancements such as causal attenuation, complex frequency, and Filon integration.

To simulate the LSS waveform data, we used four different wavelets (Figure 2.8) as signatures of the two transmitters and the two receivers in the LSS tool. We generated 512 points of a synthetic waveform, then added 5% colored noise to produce "data" traces for processing.

To test the sensitivity of our inversion to parameters such as formation to fluid density ratio, P-wave attenuation of formation and the borehole fluid attenuation to our inversion procedure, we inverted first for only one unknown parameter–the formation shear velocity(v_s). The other parameter values used in our test are: borehole radius $R = 0.08$ m; formation compressional velocity $v_P = 2.40$ km/s; borehole fluid velocity $V_{fl} = 1.5$ km/s; fluid density $\rho_{fl} = 1.0$ Mg/m^3; formation density $\rho_b = 1.88$ Mg/m^3, i.e., formation to fluid density ratio is 1.88; fluid quality factor $Q_{fl} = 100$; formation quality factor $Q_P = 22$; and formation shear quality factor Q_S is taken as a half of Q_P.

For synthetic tests, the borehole parameters were taken from depth 615 mbsf of hole 806B (Frazer, Sun and Wilkens 1997a). In order to examine the effect of Q_P^{-1} on the inversion for v_P/v_S , a joint inversion for v_P/v_S and Q_P^{-1} was carried out. Q_S was set to one half of Q_P. The variation of Q_P^{-1} was from 0.01 ($Q = 100$) to 0.068 ($Q = 15$) with an increment of 0.0025 while the variation of v_P/v_S was from 1.8 to 4.5 with an increment of 0.1. The range of the variation for Q_P^{-1} corresponded to that of calculated from the sonic well logging data of hole 806B. Figure 3.3 (upper panel) shows that the scalar objective function ϕ, which was constructed with F_1 and F_2 from equation (6.1), is sensitive to v_P/v_S but less sensitive to the formation attenuation Q_P^{-1}. This may have resulted from using full waveforms where the P-wave train, although sensitive to Q_P^{-1}, has a small contribution because its duration

is short in the entire waveform. Our procedure was performed at 103 frequencies ranging from 5 to 25 kHz. Thus the Stoneley waves, although sensitive to v_S, are almost absent with the frequency band of the ODP data set.

What is the sensitivity of the inversion to Q_{fl}^{-1}? A joint inversion for Q_{fl}^{-1} and v_P/v_S was carried out. In the test, Q_{fl}^{-1} was stepped from 0.006 ($Q = 166$) to 0.025 ($Q = 40$) with an increment of 0.001, corresponding to the attenuation of the borehole fluid of sea water. Figure 3.3 (middle panel) shows that the inversion for v_P/v_S is not sensitive to Q_{fl}^{-1}. Like Q_{fl}^{-1}, the formation density (ρ) has little effect on the inversion for v_P/v_S as shown in Figure 3.3 (lower panel), where the variation of the formation density corresponds to that of the density log of hole 806B.

The other two parameters which have significant effects on the inversion for v_S are the P-wave velocity v_P and the borehole radius R. Small variations in v_P and R may result in a significant change of the estimate of v_S. When the transmitter emits a pulse, propagating in the borehole fluid toward formations, part of its energy is converted back into P-waves in the fluid to be detected by the receiver, and another part of its energy is radiated out into the formation as shear waves. The amount of the wave energy converted into shear waves depends on the formation Poisson's ratio, and thus on the shear wave velocity of the formation. So the data are sensitive to the ratio of v_P over v_S.

To effectively account for the effect of v_P and R on the inversion, we use a 3-D search to simultaneously extract three parameters (i.e., v_P , v_P/v_S , and R) from the four waveforms at each depth.

To make the inversion efficient, we first generated a table of synthetic Green's functions in which v_P varies from 2.3 km/s to 2.7 km/s with an increment of 0.02, v_P/v_S varies from 1.8 to 4.5 with an increment of 0.1, and R varies from 0.059 m to 0.161 m with an increment of 0.003. The other parameters were fixed in the synthetic Green's functions. The P-wave attenuation and formation density were taken as an

average over a depth range of 500 to 700 meters below sea floor, because the data are relatively insensitive to those two parameters.

To test the feasibility of the technique outlined above to field data, we first applied it to the synthetic data at a depth range of 500-700 mbsf with an depth increment of 1 meter. The synthetic data used information from well logging field data. The S-wave velocity was taken as v_P minus 1.5, and P-wave attenuation was estimated as from Chapter 4. The other parameters such as v_{fl} and Q_f were the same as above.

Figure 3.4 shows the v_P , v_S, and R found from the 3-D search with a weighted average given by equation (10). It is worthy of mention that the variations of Q_P, Q_S, and ρ_b are not accounted for during the 3-D search. In other words, while these parameters change with depth in the "data", they are assumed to be constant in our inversion procedure. So it is not surprising that the inverted results are imperfect. Nevertheless it can be seen from Figure 3.4 that the inverted v_P and R are in good agreement with the true values while the inverted v_S has a small variation around the true values. This is because the waveform data resolve v_P and R better than that v_S. The average of eight objective functions along the three cross sections is shown in Figure 3.5. It is important to note that at depth ranges with higher P-wave velocities, the objective function is more sensitive to v_P/v_S . This is because the information about S-velocity is mostly from the wavetrain between the P-wave first arrival and the end of the fluid wave. If the P-wave velocity is higher or R is smaller, the wave train becomes relatively longer, thus more information about v_S is included.

3.5 FIELD DATA TESTS

3.5.1 ARCO data results

The theoretical logging model may not exactly simulate the actual logging case because of the presence of the tool in the bore hole. In addition, it is reasonable to doubt whether there is any information about formation S-wave velocity in the frequency band of 5-25 kHz for monopole waveforms in soft formations. To address these two questions, a test was performed with a logging data set collected by the ARCO array sonic tool with 12 receivers and two monopole sources. In the same borehole, the formation S-wave velocity was directly measured by the ARCO dipole S-wave logging tool. In order to extract formation shear velocities from this data set, we used a pairwise processor (Frazer and Sun, 1998), in which the two source transfer functions are considered identical. The reason for using a pairwise processor rather than a fourwise processor is that the frequency band of the monopole ARCO data is much narrower than that of the ODP data. Figure 3.6 shows good agreement among the 12-pair results at depth 3100 feet. Figure 3.7 shows that our inverted v_S profile is similar to that obtained with the ARCO S-wave logging tool.

3.5.2 ODP data results

To check the fourwise inversion procedure on field data, we first use it to invert the ODP data only for formation P-wave velocity v_P . As noted above, tests with synthetic data show that errors in assumed values of Q_P, Q_S, Q_{fl} and ρ_b do not affect the inversion for v_P/v_S very much. However, errors in assumed values of v_P and of borehole radius R may bias the inversion for v_P/v_S . Fortunately v_P and R are not independent. The P-wave arrival time T_a is related to the formation velocity v_P , the borehole fluid velocity v_{fl}, the borehole radius R and the distance Z between source

and receiver by the ray theory formula

$$\begin{aligned} T_a &= \frac{2R}{\cos(\theta)v_{fl}} + \frac{Z-2R\tan(\theta)}{v_P}, \\ \theta &= \arcsin(\frac{v_{fl}}{v_P}). \end{aligned} \tag{11}$$

It can be seen that for a given v_P , an R, referred to here as sonic R, is determined by the first arrival time T_a and v_{fl}. In order to verify the v_P from the sonic log, we searched over v_P with ϕ, while varying R so as to preserve arrival time. Figure 3.8 shows good agreement between v_P found in this way (+) and v_P from the log (solid line) in the depth range from 500 to 700 mbsf. Above 550 mbsf, the hole is very large and the tool may not have been centered in the hole.

Although the profiles of v_P and sonic R are available, a 3-D search for v_P , v_P/v_S , and R is used instead of a simple 1-D search for v_P/v_S , because a small error of v_P or R might significantly degrade the inversion for v_P/v_S . The known v_P and sonic R are taken as the a priori information in the inversion. Figure 3.9 shows ϕ averaged with eight pairs from equation (6) with changes of v_P , v_P/v_S , and R. The features of ϕ in terms of v_P , v_P/v_S , and R in Figure 3.9 look similar to those in Figure 3.6 except for the difference of values of ϕ. The maximum value of ϕ corresponds to the optimum values of v_P , v_P/v_S , and R. Changes of Φ with both v_P and v_P/v_S , or both R and v_P/v_S at the depth of 540 mbsf and 600 mbsf are shown in Figure 3.10. It can be seen that in the v_P and v_P/v_S domain, ϕ normally has only one peak while in the v_P/v_S and R domain ϕ usually has multiple peaks. This phenomenon can also be observed in the synthetic processing. The maximum value of ϕ at depth 600 mbsf is greater than that at depth 540 mbsf. The greater the maximum value of ϕ, the more confidence we have in the inverted results. The results of v_S, v_P , and R calculated in the manner of equation (10) show that the inversion is stable (Figure 3.11). The inverted v_P agrees well with the sonic v_P . The reasonableness of the inverted v_S profile is supported by the fact it changes with depth, in a similar way to the v_P profile.

3.6 CONCLUSIONS

In this study, we first tested the feasibility of inverting for S-wave velocity from the monopole sonic waveforms. Although neither Stoneley waves nor direct refracted S-waves are present in these data, the S-wave velocity can be inverted by using a pairwise or fourwise procedure. The test for the ARCO data set shows that within the frequency band of 5–20 kHz, the inverted S-wave velocity is in good agreement with that measured by the S-wave logging tool, showing that it is feasible to extract S-wave velocity from the ODP data set recorded by the Schlumberger LSS tool.

Second, the fourwise procedure was successfully applied to the LSS data set to invert for P-wave velocity, although the sources and receivers in the tool were not well calibrated. It was not necessary to estimate the source-receiver transfer functions, which in practice may be quite different from each other. The inverted P-wave velocities are in good agreement with those calculated by P-wave first arrivals in the depth range from 550 mbsf to 700 mbsf, suggesting that the tool was probably centered during logging in this depth range. Our synthetic model assumes that the tool is centered so if the tool is not centered then the inversion may be biased.

Finally, the 3-D search for v_P , v_P/v_S , and R gives stable results for v_S and v_P . The inverted P-wave velocity profile agrees well with the sonic v_P . The inverted v_S profile seems to change with depth in a similar way to the v_P profile, as expected, indicating that the inverted v_S is reasonable. In general, shear velocities are more reliably determined for greater depth. First, the waveform at deep depths includes more information about S-wave velocity than that at shallow depths due to relatively high P-wave velocity. This is because the shear information is mostly contained in the wave train between P-wave arrival and borehole fluid wave arrival. The longer the wave train, the more information about S-wave velocity is contained. Second, at deep depths, the borehole size is smaller and does not change much with depth.

The tool was therefore probably reliably centered in the hole. Similarly, the inversion might be problematic at shallow depths because centering the tool might be difficult due to the large borehole.

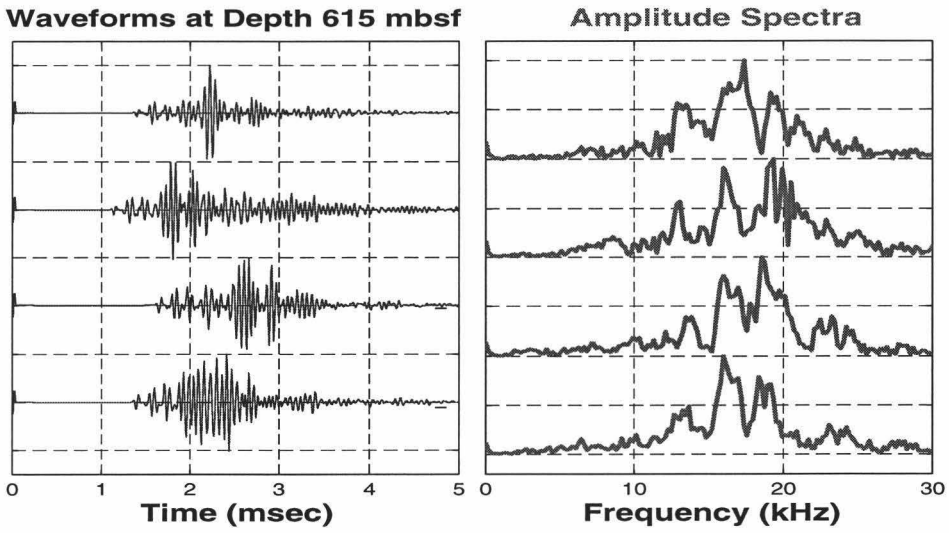

Figure 3.1: Four waveforms and their amplitude spectra with the source-receiver spacing of 10, 8, 12, and 10 ft, respectively, recorded by the Schlumberger LSS sonic tool at 615 mbsf in hole 806B, Ontong Java Plateau.

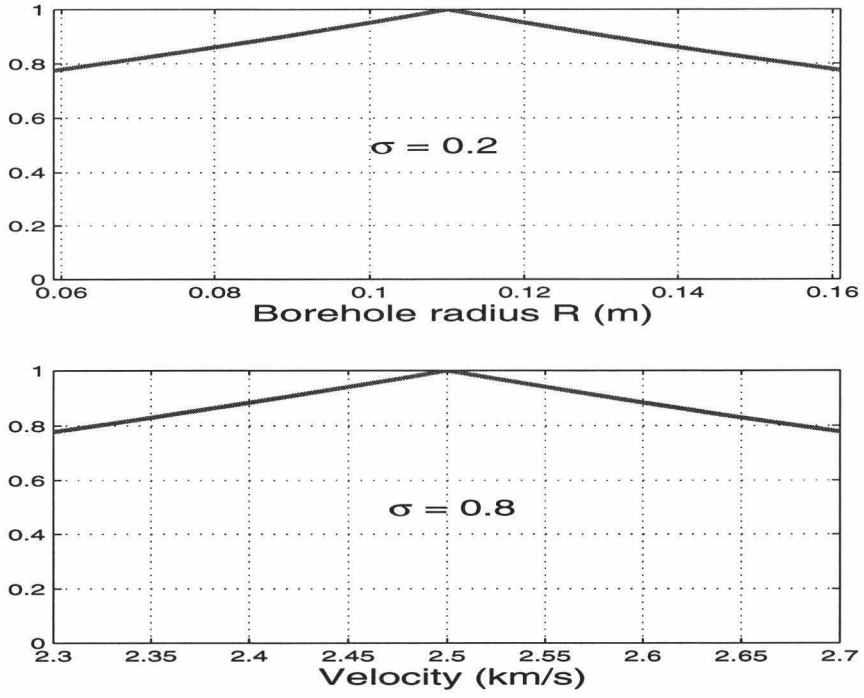

Figure 3.2: Exponential weighting functions used as a priori information in 3-D search for P-wave velocity and the borehole radius R.

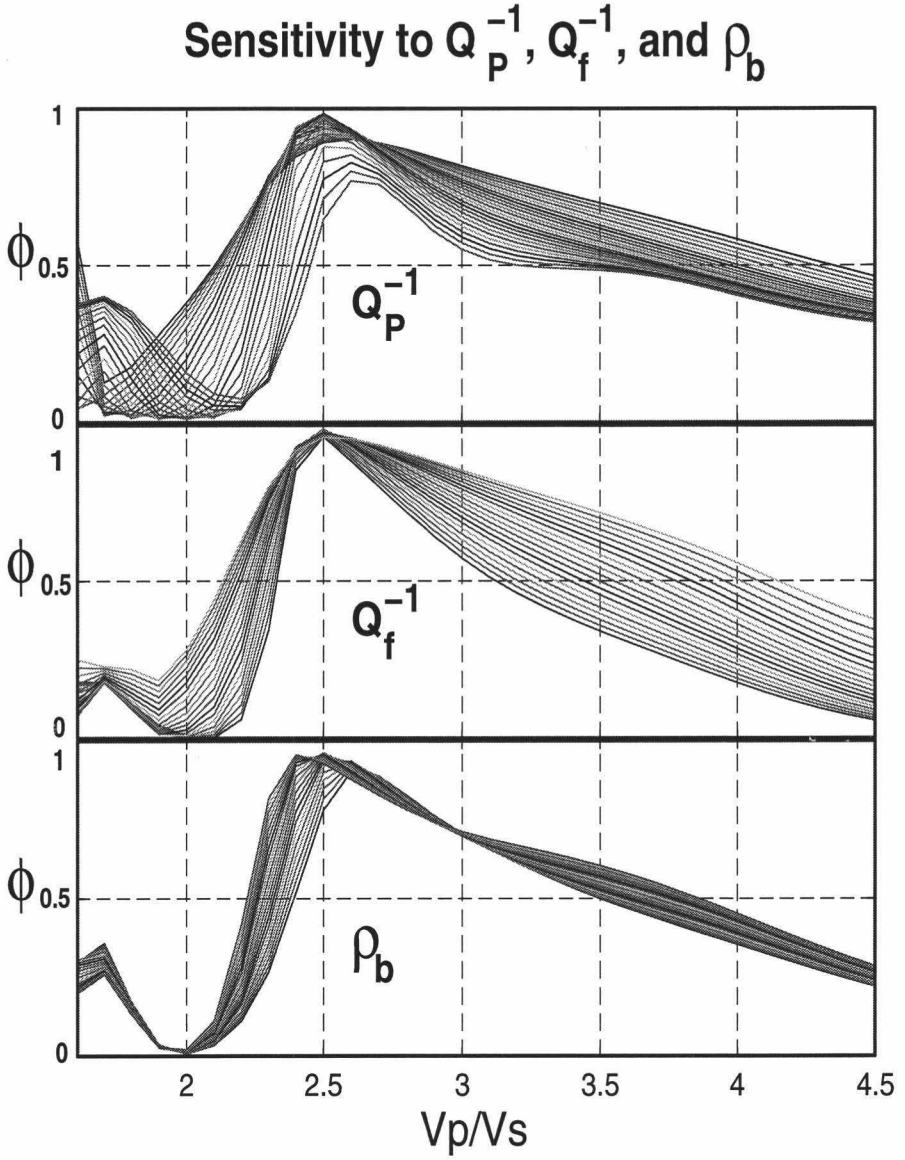

Figure 3.3: Ssensitivity of ϕ with v_P/v_S to Q_P^{-1}, Q_f^{-1} and formation density ρ_b. Q_P^{-1} changes from 0.01 to 0.0675 with an increment 0.0025. Each curve in the upper panel was calculated with one value of the Q_P^{-1}. Similarly, in the middle panel, Q_f^{-1} changes from 0.006 to 0.0025 with an increment 0.0025, and in the bottom panel, ρ_b changes from 1.6 Mg/m^3 to 2.0 Mg/m^3 with an increment 0.2.

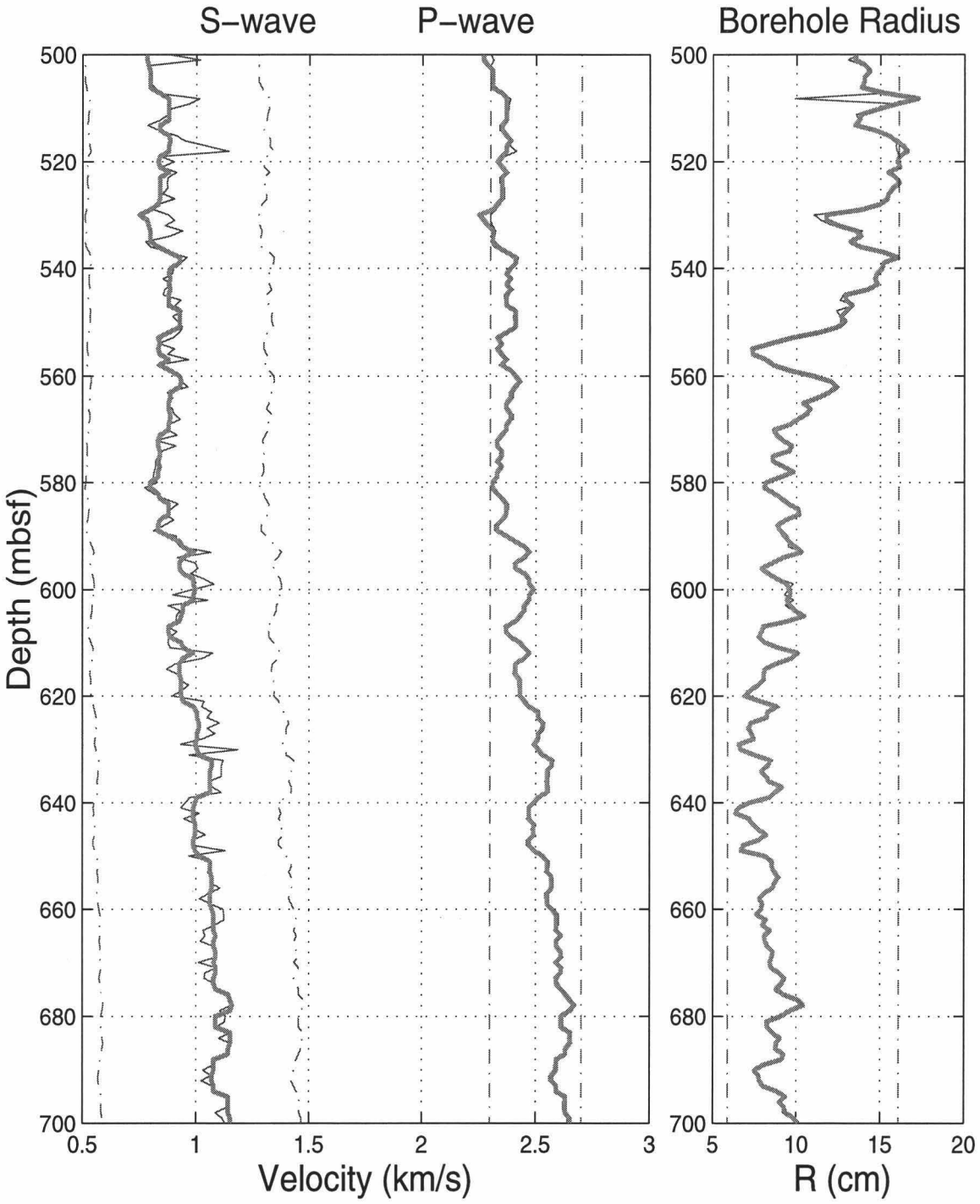

Figure 3.4: The profiles of v_P, v_S, and R inverted from the synthetic data by the 3-D search inversion. The dashdot lines are search boundaries and solid thin lines are the results inverted from inversion. The solid thick lines are respectively true values of R, v_P, and v_S input into the model.

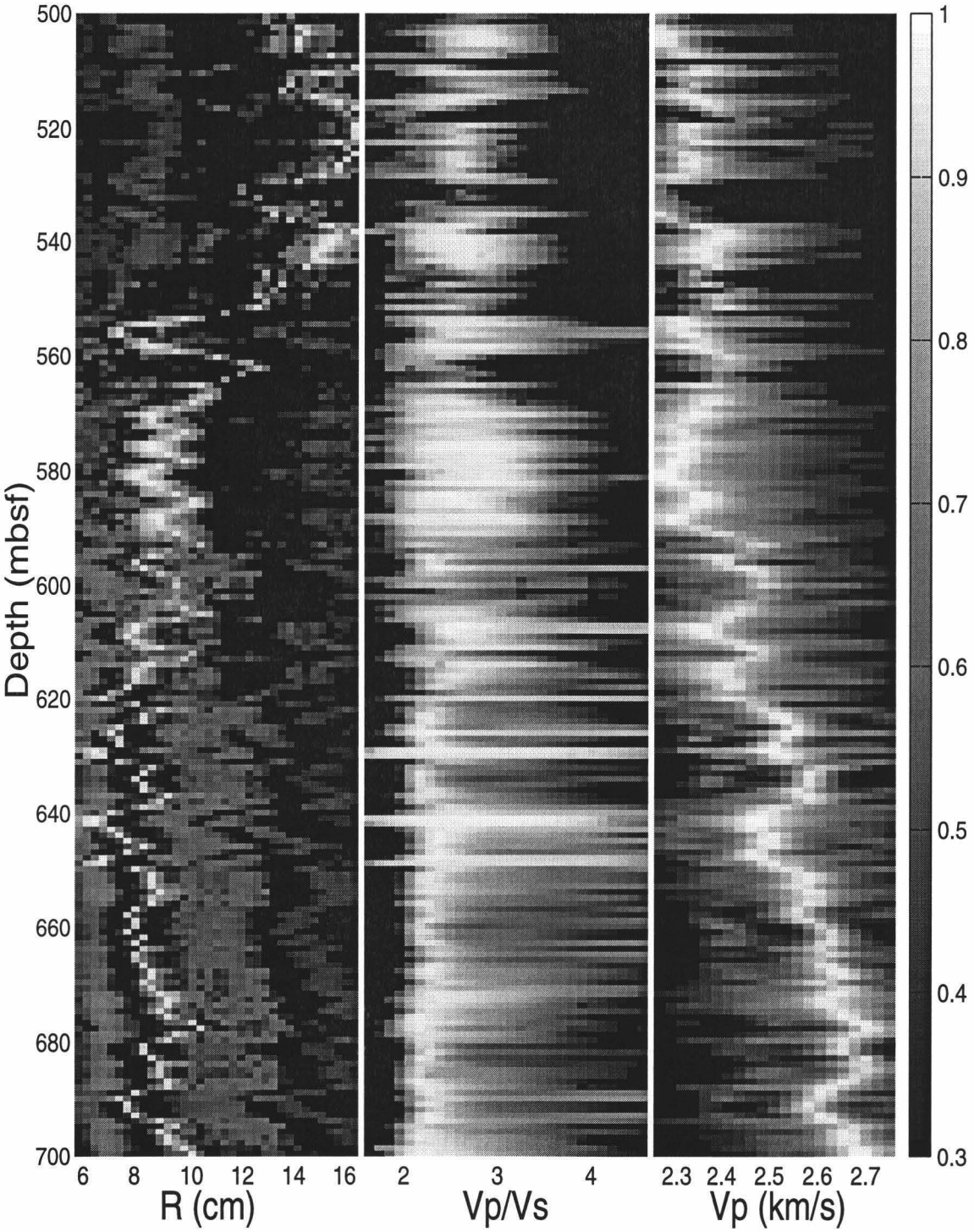

Figure 3.5: 3-D inversion image of ϕ averaged with the eight objective function from the synthetic data. This image is a display of the value of ϕ along R, v_P/v_S, and v_P, respectively.

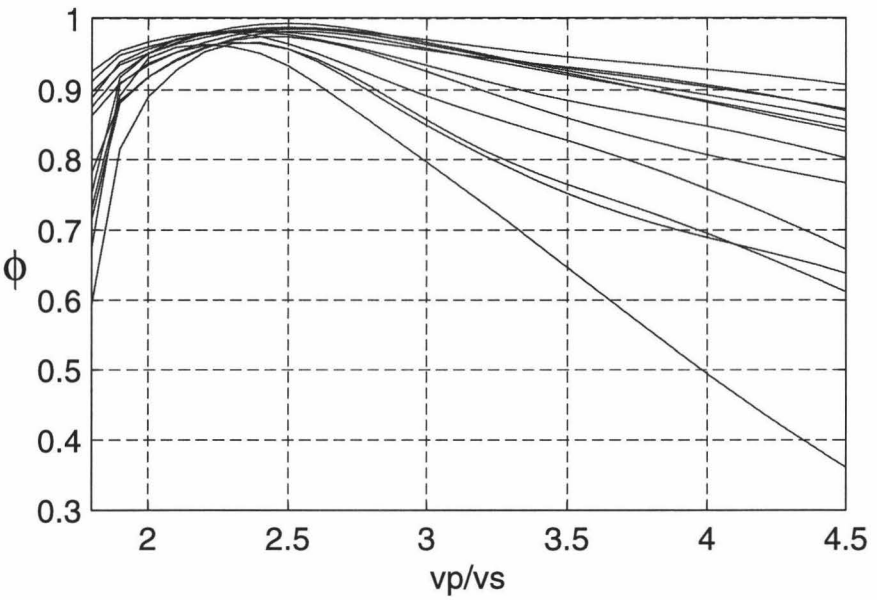

Figure 3.6: ϕ for each of 12 pairs from the arco array sonic waveforms with a frequency band of 5-20 kHz at depth 3100 ft, where v_P/v_S equals 2.35 from the S-wave log. 12 pairwise processors were independently performed from 12 pairs with the same receiver and two sources at one depth.

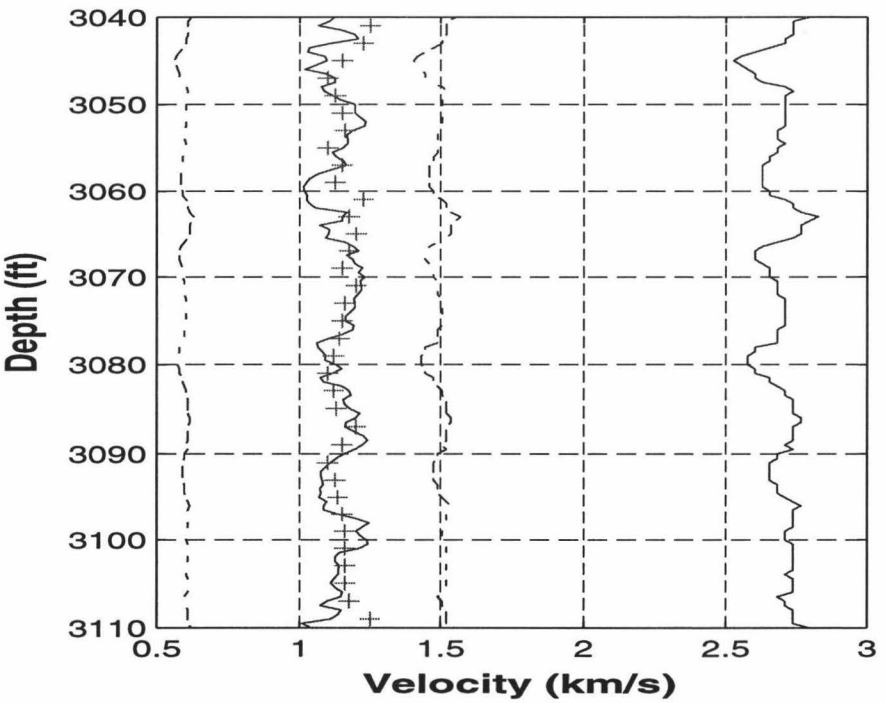

Figure 3.7: Comparison between inverted v_S (left solid line) and $v_S(+)$ obtained with the ARCO S-wave logging tool. The right solid line is v_P and the dashed lines are v_S search boundaries.

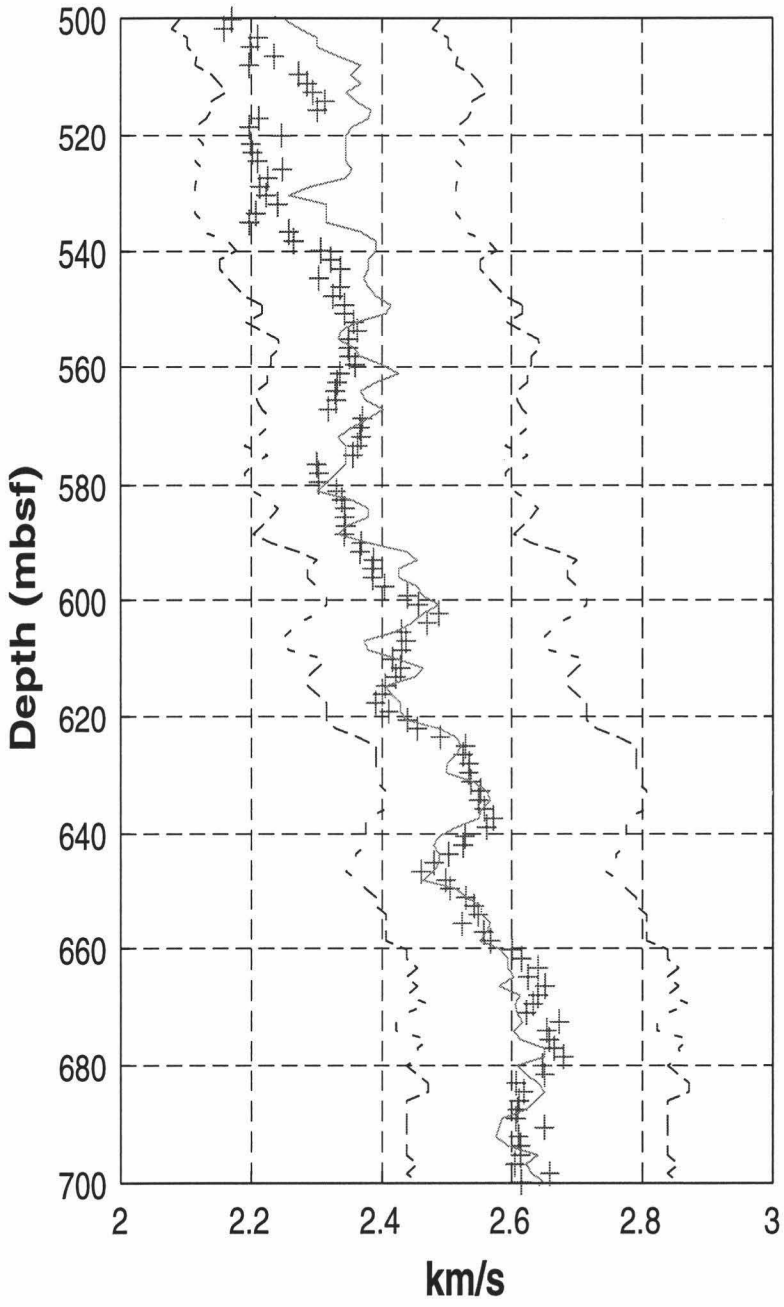

Figure 3.8: Comparison between v_P found using ϕ (+) and sonic v_P (solid line). Dashed lines are search boundaries. The objective function was constructed with equation (6.1).

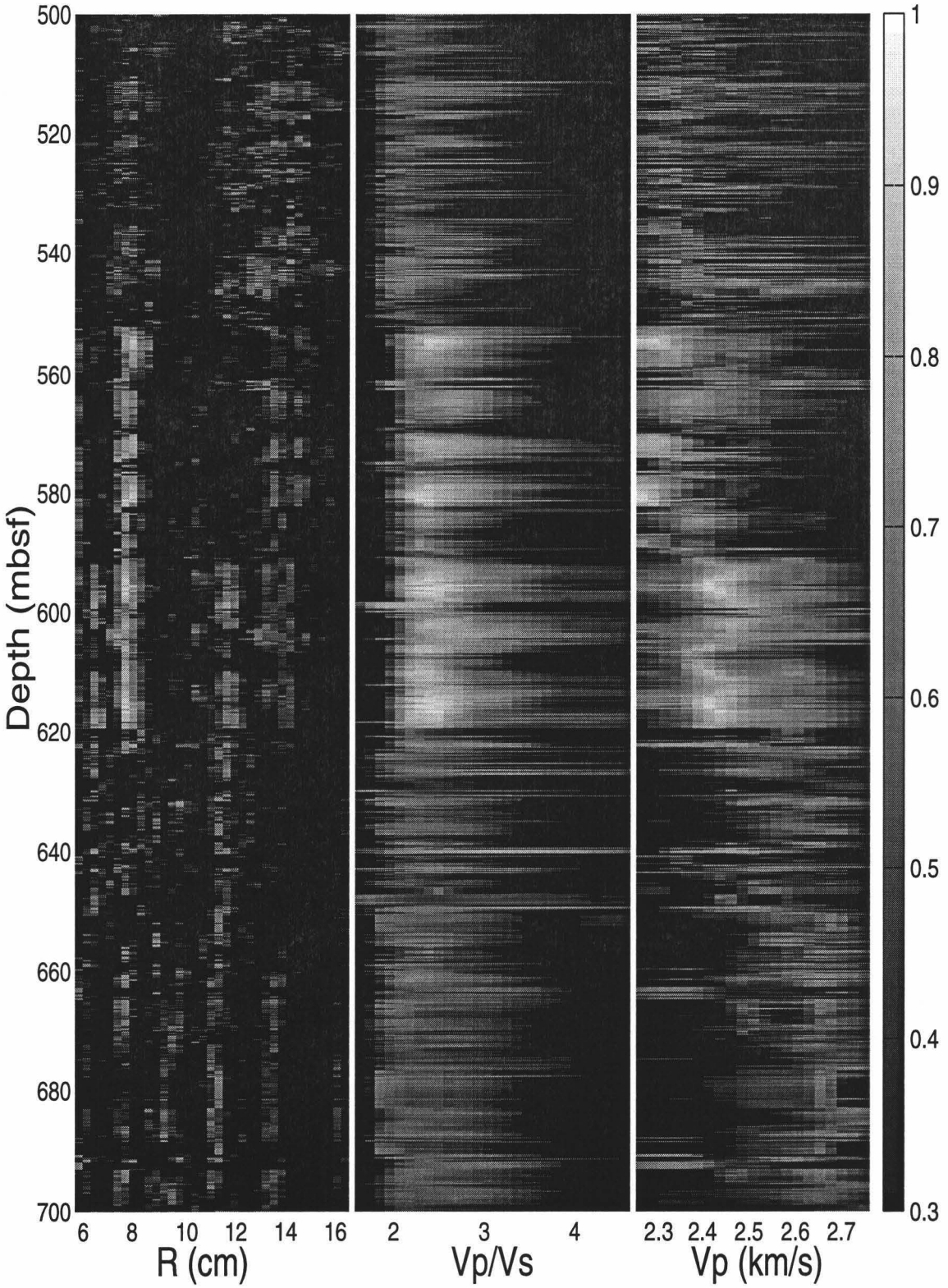

Figure 3.9: 3-D inversion image of ϕ averaged with the eight objective function from the ODP data. This image is a display of the value of ϕ along R, v_P/v_S, and v_P, respectively.

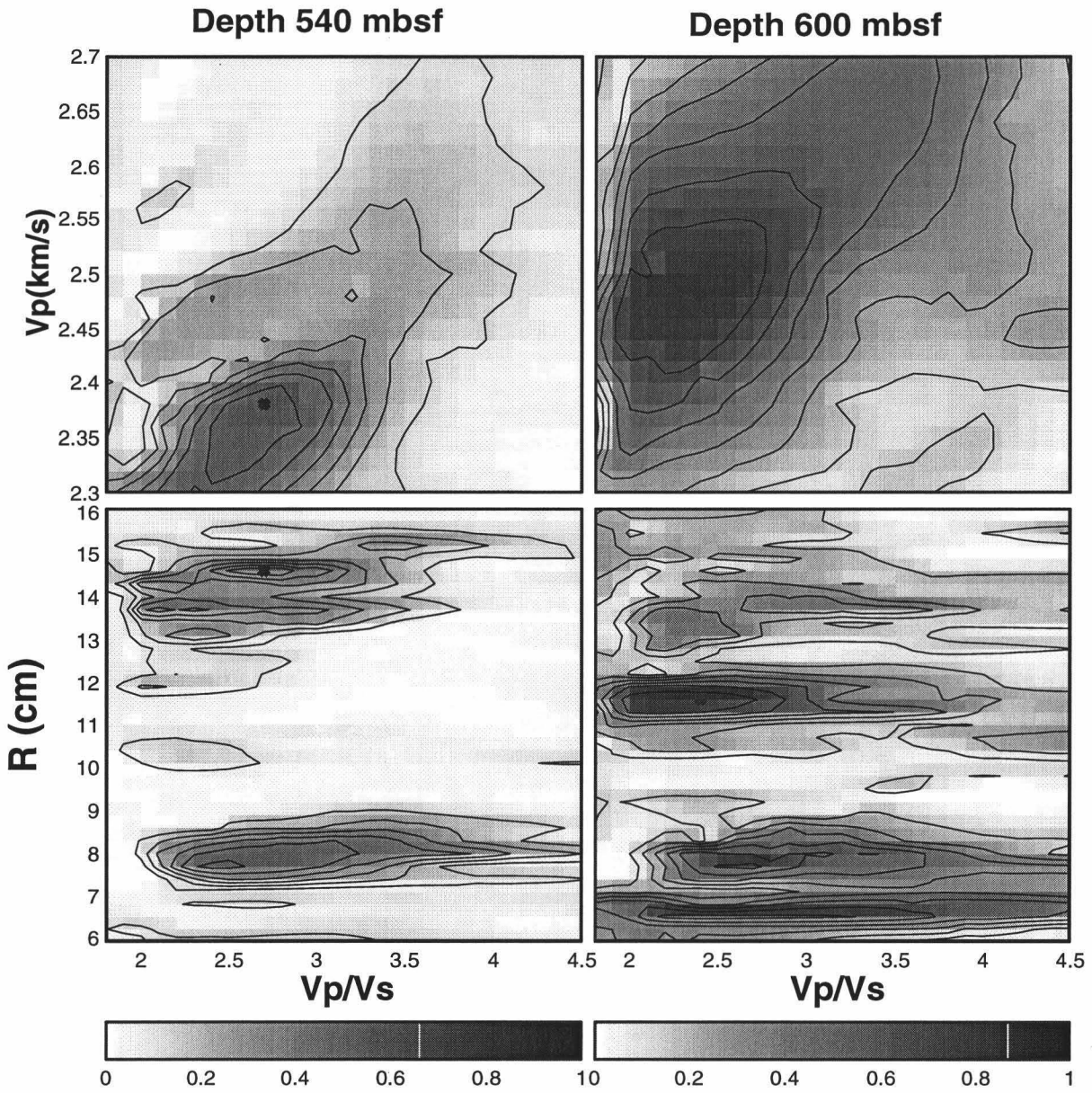

Figure 3.10: Distribution of ϕ with changes of both v_P/v_S and v_P (upper panel), and both v_P/v_S and R (lower panel) at depth 540 mbsf and 600 mbsf.

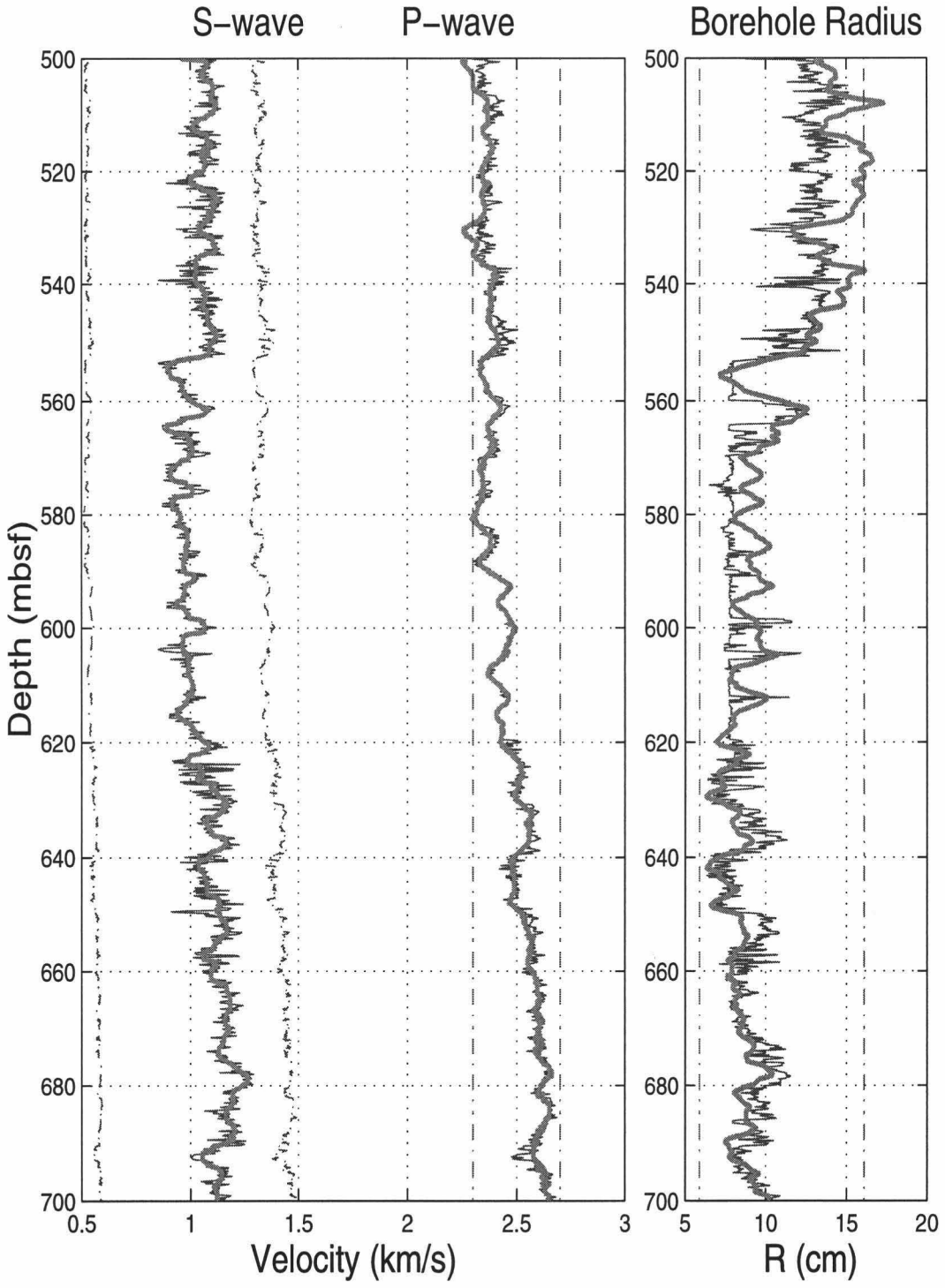

Figure 3.11: The profiles of v_P, v_S, and R inverted from the ODP sonic data by the 3-D search inversion. The dashdot lines are search boundaries and solid thin lines are the results inverted from inversion. The solid thick lines are respectively sonic R, v_P, and the v_S averaged with a median over each 10 ft depth interval.

3.7 REFERENCES

Cheng, C. H., 1989, Full waveform inversion of P-waves for V_s and Q_p, *J. Geophys. Res.*, **94**, 15,619-15626.

Stenevs, J. L. and Day, S. M.,1986, Shear velocity logging in slow formations using the Stoneley wave, *Geophysics*, **51**, 137-147.

Frazer, L. N. and Sun, X. H., 1998, New objective functions for waveform inversion: *Geophysics* , **63**, 213-222.

Frazer, L. N., Sun, X. H., and Wilkens, R. H., 1997a, Changes in attenuation with depth in an ocean carbonate section: ODP sites 806 and 807, Ontong Java Plateau: J. Geophys. Res., **102**, 2983-2997.

Mallick, S. and Frazer, L. N., 1987, Practical aspects of reflectivity modeling: *Geophysics*, **52**, 1355-1364.

Toksöz, M. N., Wilkens, R. H., and Cheng, C. H., 1985, Shear wave velocity and attenuation in ocean bottom sediments from acoustic log waveforms: *Geophys. Res. Lett.*, **12**, 37-40.

Tolstoy, A., 1993, Matched Field Processing: World Scientific.

Sun, X. H., Frazer, L. N. and Wilkens, R. H., 1998, Inversion for S-wave velocity from ODP sonic logging data: 68th Ann. Internat. Mtg., Soc. Expl. Geophys., Expanded Abstracts, 264-267.

Wilkens, R. H., Cheng, C. H. and Meradith, J. A., 1992, Evaluation and prediction of shear wave velocities in calcareous marine sediment and rocks: *J. Geophys. Res.*, **97**, 9297-9305.

Chapter 4
Changes in P-wave attenuation with depth at ODP Sites 806 and 807

4.1 SUMMARY

A method is proposed to estimate relative *in situ* seismic attenuation from full waveform acoustic logs. The relative attenuation (Q_p^{-1}) is computed from the variation with depth of the amplitude spectrum of the P-wave train from one source-receiver pair. Tests with synthetic data generated by a full waveform method show that the variation of the P-wave amplitude spectrum with frequency depends much more on Q_p^{-1} than other unknown parameters such as v_s^{-1}. This method is applied to Ocean Drilling Program data from Holes 806B and 807A on the Ontong Java Plateau in the western Pacific Ocean. Four continuous Q_p^{-1} logs were computed independently using data from four different source-receiver pairs. Agreement of the four Q_p^{-1} logs at each site, and similar results for the two sites, suggest that the method is robust and practical. The attenuation profiles exhibit a maximum Q_p^{-1} between 300 and 500 meters below the seafloor.

4.2 INTRODUCTION

For many years the Ocean Drilling Program (ODP) has recorded full waveform data acquired by the Schlumberger Long-Spaced Sonic Tool (LSS). The LSS has two sources and two receivers. Every 15 cm (6 in), four microseismograms, with source-receiver spacings of 2.44 m (8 ft), 3.05 m (10 ft), 3.05 m and 3.66 m (12 ft), are

recorded from the different source-receiver pairs. These data provide a good record of the *in situ* physical properties of the ocean bottom. In this study we develop a method to calculate relative P-wave attenuation from these data. Existing methods of attenuation determination include spectral ratio (Cheng *et al.*, 1982; Sams *et al.*, 1990; Tonn, 1991), centroid frequency shift (Quan *et al.*, 1994), filter correlation (Courtney, 1993), partition coefficients, and full waveform inversion (Paillet and Cheng, 1991). Our attempts to apply some of these methods to data collected at 2 pelagic carbonate sites on the Ontong Java Plateau in the western Pacific Ocean yielded poor results because the receiver responses of the LSS are not known and not constrained by the data. Additionally, differences between the frequency spectra of the two sources and an unknown formation S-wave velocity make it difficult to accurately determine Q_p from full waveforms. However, we have found that it is possible to quantify relative changes in Q_p^{-1} with depth using the method developed in this study. This method yields results that are in good agreement with those from earlier studies.

4.3 BASIC PRINCIPLES

Considering that the frequency responses of two receivers in the tool differ from each other $R_1(\omega) \neq R_2(\omega)$, and the amplitude spectra of two sources in the tool also differ from each other $S_1(\omega) \neq S_2(\omega)$, we denote the amplitude spectrum X_1 of the 2-1 P-wave train by the following formula:

$$X_1(z, \omega, \Delta z_1) = S_2(\omega) R_1(\omega) C(\omega) G(\omega, \Delta z_1) \exp\left(-\frac{\omega}{2 Q_p v_p} \Delta z_1\right), \qquad (1)$$

with similar formulas for the 1-1, 1-2 and 2-2 source-receiver pairs. The geometric spreading function $G(\omega, \Delta z_1)$ and the source-receiver to fluid coupling function $C(\omega)$ are thought to depend on frequency ω (Sams 1990). Rearranging equation (1) and

taking the logarithm gives

$$\frac{2\ln X_1}{\omega} = -\Delta t Q_p^{-1} + \frac{2\ln(S_2 R_1 CG)}{\omega}, \tag{2}$$

in which $\Delta t = \frac{\Delta z_1}{v_p(z)}$ is the travel time from source S_2 to receiver R_1 and $Q_p^{-1} = Q_p^{-1}(z)$ is the averaged reciprocal Q_p of the interval between S_2 and R_1.

Now we write equation (2) in the following way:

$$\Phi(z,\omega) = f(z) + A(\omega), \tag{3}$$

where $\Phi(z,\omega) = \frac{2\ln X_1}{\omega}$, $f(z) = -\Delta t Q_p^{-1}$ and $A(\omega) = \frac{2\ln(S_2 R_1 CG)}{\omega}$. It can be seen from equation (3) that we neglect the dependence of geometric spreading G on the formation parameters. First, let us use numerical simulations to study the properties of the function $\Phi(z,\omega)$.

4.3.1 Analysis Using Synthetic Waveform Data

In the synthetic sonic logging calculation procedure, the pressure response at a point located at cylindrical coordinate $(r, \Delta z)$ from the source located at $(0,0)$ in a fluid-filled borehole can be derived. Following Cheng et al.(1989) notations, we write the response as

$$P(r,\Delta z,t) = \int_{-\infty}^{+\infty} S(\omega) e^{-i\omega t} d\omega \int_{-\infty}^{+\infty} A(k,\omega) I_0(fr) e^{ik\Delta z} dk, \tag{4}$$

in which

$$A(k,\omega) = \frac{gK_1(fR) - K_0(fR)}{gI_1(fR) + I_0(fR)}, \tag{5}$$

and

$$g = \frac{f\rho}{l\rho_f}\left\{(\frac{2v_s^2}{c^2} - 1)^2 \frac{K_0(lR)}{K_1(lR)} - \frac{2v_s^2 lm}{k^2 c^2}[\frac{1}{mR} + \frac{2v_s^2}{c^2}\frac{K_0(mR)}{K_1(mR)}]\right\}. \tag{6}$$

I_0 is the modified Bessel function of the first kind of the zeroth order, K_0 and K_1 are the modified Bessel functions of the second kind of the zeroth order and the first

order. ρ and ρ_f are the density of the formation and the borehole fluid. R is the borehole radius, c is the phase velocity, l, m, and f are the radial wave numbers given by

$$p^2 = k^2 - \frac{\omega^2}{v^2};$$

where p is for l, or m, or f; and correspondingly v for v_p, or v_s, or v_f. They are the P- and S- wave velocity of the formation and the borehole fluid velocity, respectively. k is the wave number in the z direction.

The complete acoustic waveform is computed by discrete wave-number integration and an FFT. The spectrum of the source function is described by (Tsang & Rader 1979) as:

$$S(\omega) = \frac{8\alpha\omega_0(\alpha - i\omega)}{[(\alpha - i\omega)^2 + \omega_0^2]^2}. \tag{7}$$

Attenuation is introduced through a complex velocity given by:

$$v(\omega) = v(\omega_{ref})[1 + \frac{1}{\pi Q}\ln(\frac{\omega}{\omega_{ref}})][1 + \frac{i}{2Q}]^{-1}, \tag{8}$$

where Q is the quality factor for either the P-wave or S-wave, and v is either the P-wave velocity or S-wave velocity, ω_{ref} is an arbitrary reference frequency.

The first arrival in full waveform sonic logs is a P head wave. We separate it from later arrivals using a time window tapered at both ends using a cosine taper. Then we calculate Φ as a function of Q_p^{-1} at different frequencies, as shown in Figure 4.1. The other model parameters used in Figure 4.1 are similar to those of soft marine carbonate sediments. The parameters of the source function are: $\omega_0 = 2\pi \times 15$ kHz and $\alpha = 0.5\omega_0/\pi$. The relationship between Φ and Q_p^{-1} is nearly linear (Figure 4.1). As Q_p^{-1} changes with depth, Φ also changes. While Φ depends on frequency, at different frequencies the relationships between Φ and Q_p^{-1} change very little. Next, we calculate Φ with shear slowness v_s^{-1} and Q_p^{-1} at frequency 10 kHz, because the S-wave velocity of formations is unknown. For $v_s < 1$, Φ depends much more significantly

on Q_p^{-1} than on v_s^{-1} (Figure 4.2). These results suggest that we can use equation (3) to approximately estimate Q_p^{-1}. Based on equation (3), an estimation method is developed, which is described in the following section.

4.3.2 Method for Attenuation Estimation

We wish to reduce the noise in $\Phi(z,\omega)$ by "averaging" different frequencies using a combination of means and medians. We must, however, proceed carefully, because in equation (3) we don't know what $A(\omega)$ is, and it could greatly affect a median over ω. First, at each depth we form the average $\Phi(z,\omega)$:

$$\bar{\Phi}(z) = \frac{1}{N}\sum_{\omega=\omega_1}^{\omega_N} \Phi(z,\omega) \tag{9}$$

It can be seen that $\bar{\Phi}(z) \approx f(z) + \bar{A}$. Then we calculate the median depth shift of each Φ from the average.

$$\Delta\tilde{\Phi}(\omega) = \underset{z}{median} \left\{\Phi(z,\omega) - \bar{\Phi}(z)\right\}, \tag{10}$$

in which $\Delta\tilde{\Phi}(\omega) \approx A(\omega) - \bar{A}$. At this stage, it seems that the median over depth did nothing if A were depth independent. Next we shift each curve to bring it closer to the average:

$$\Phi'(z,\omega) = \Phi(z,\omega) - \Delta\tilde{\Phi}(\omega). \tag{11}$$

Finally we take the $\omega - median$ of this family of curves:

$$\hat{\Phi}(z) = \underset{\omega}{median} \left\{\Phi'(z,\omega)\right\}. \tag{12},$$

in which $\hat{\Phi}(z) \approx f(z) + \bar{A}$. It seems there is nothing done with the $\omega - median$. In other words, the result can simply be achieved by using a mean over ω instead of the above-described mean-median procedure. The main reason for using the above

procedure is that A in equation (3) is not only frequency-dependent but also weakly depth-dependent.

The result $\hat{\Phi}(z)$ is an estimate of $-\Delta t(z)Q_p^{-1}(z)$ plus an unknown constant $\hat{A}$:

$$\hat{\Phi}(z) = -\Delta t(z)Q_p^{-1}(z) + \hat{A}. \tag{13}$$

In order to obtain the value of the unknown constant $\hat{A}$, it is necessary to assume a value of Q_p at some reference depth ζ, say, $Q_p(\zeta) = 100$. Other necessary informations $\Delta t(\zeta)$ and $\hat{\Phi}(\zeta)$ are obtained from waveform data processing. We set z equal to ζ in equation (13) and then solve for $\hat{A}$; this yields

$$\hat{A} = \hat{\Phi}(\zeta) + \Delta t(\zeta)Q_p^{-1}(\zeta). \tag{14}$$

Now, knowing the fixed offset $\hat{A}$, we can recover $\Delta t Q_p^{-1}$ from

$$\Delta t(z)Q_p^{-1}(z) = \hat{A} - \hat{\Phi}(z) = \hat{\Phi}(\zeta) - \hat{\Phi}(z) + \Delta t(\zeta)Q_p^{-1}(\zeta). \tag{15}$$

Using values of $\Delta t(z)$ from the velocity log and solving for Q_p^{-1} gives

$$Q_p^{-1}(z) = \frac{\hat{\Phi}(\zeta) - \hat{\Phi}(z) + \Delta t(\zeta)Q_p^{-1}(\zeta)}{\Delta t(z)} \tag{16}$$

This estimate of $Q_p^{-1}(z)$ can be averaged with estimates of $Q_p^{-1}(z)$ from the other source-receiver pairs.

4.3.3 Test on Synthetic Data

Before using this method to process the ODP data, we demonstrate the validity of our algorithm using synthetic waveforms. In order to simulate the full waveforms from the LSS tool in slow formations, we first assume that P-wave velocity and density increase with depth in a manner similar to ODP Hole 806B (Figure 4.3). In other words, in the synthetic test, we used v_P increasing linearly with depth from 1.75 km/s

at 200 m to 2.6 km/s at 700 m, and ρ_b increasing linearly from 1.6 Mg/m^3 at 200 m to 1.9 Mg/m^3 at 700 m. We then assume a Q_p^{-1} log (Figure 4.4). S-wave velocities are obtained by using a fixed Poisson's ratio. Other model parameters are the same as Figure 4.1. Using the above parameters, we calculate synthetic waveforms from 200 m to 700 m at 5 m intervals for each source-receiver spacing. The time sampling interval of synthetic waveforms is the same as that of ODP data. Next we check the method introduced above using the synthetic data step by step.

To begin, we pick up P-wavetrain from the synthetic data using a time window which begins at the first arrival of the P-wavetrain predicted by the following formula

$$t(z) = \frac{2R}{v_f \cos(\sin^{-1}(\frac{v_f}{v_p}))} + \frac{\Delta z - 2R \tan(\sin^{-1}(\frac{v_f}{v_p}))}{v_p}, \tag{17}$$

where Δz is a source-receiver spacing.

The window size is generally a sensitive parameter. In soft marine carbonate sediments, the P-wave velocity is very low, approaching the borehole fluid velocity, and the P-wave duration is short. In our application 20 data points (200 μsec) are sufficient to characterize the P-wave. The amplitude spectra of the P-wave trains are calculated by padding zeros to 128 points and using a Fast Fourier Transformation (FFT). Considering frequency distribution of the P-wave spectra, we compute function Φ in equation (3) over a frequency range from 5 kHz to 25 kHz. We then use equations (9)-(12) to calculate $\bar{\Phi}(z), \Delta\tilde{\Phi}(\omega), \Phi'(z)$, and $\hat{\Phi}$. The reference depth waveform is chosen automatically by a rule in which the maximum value of Φ corresponds to maximum Q_p, in this case set at 100. Finally we use equation (15) to calculate $\hat{A}$ and recover the $Q_p^{-1}(z)$ log using equation (16).

The assumed Q_p^{-1} log and the calculated Q_p^{-1} logs are illustrated in Figure 4.4. This result shows that the calculated Q_p^{-1} logs from different source-receiver pairs are almost the same. We calculate correlation coefficients between the assumed Q_p^{-1} log and the calculated Q_p^{-1} logs from different source-receiver pairs. With increasing

source-receiver spacing, the correlation coefficient increases. That means the longer the spacing, the better the calculated Q_p^{-1} log is. Averaged among different source-receiver spacings, the correlation coefficients for different Poisson's ratio cases(0.3, 0.35, and 0.40) shown in Figure 4.4 are 0.98, 0.94 and 0.84, respectively. Although the correlation coefficients are larger, the assumed and calculated Q_p^{-1} values obviously differ and Poisson's ratio has some effects on the calculated Q_p^{-1} logs. There are several factors which may affect the calculated Q_p^{-1} log. First, with the S-wave velocity decreasing, most of the energy of the transmitted wave is converted into P-wave. The amplitude of the P-wave for the lower S-wave velocity case is larger than that for the higher S-wave velocity case even though other parameters are the same. That means we can not get an accurate Q_p value using the assumption that the P-wavetrain from full waveforms is independent of S-wave velocity. Second, in Figure 4.4 we set a shallow reference depth with a slow S-wave velocity, which results in shifting the Q_p^{-1} log up with increasing depth. In addition, it is unreasonable to assume that Poisson's ratio does not change with depth. Because the S-wave velocity is unknown, we can not get a Poisson's ratio to accurately simulate full waveforms of ODP Hole 806B and 807A. Finally, Q_s is also unknown, which may affect our synthetic waveforms. All in all, many factors may affect our calculation results. Nevertheless, the shape of the calculated Q_P^{-1} log is very similar to that of the assumed Q_p^{-1} log.

The ODP data include a lot noise even though we have considered geometric spreading, source-receiver differences and source-receiver couples through the borehole fluid. In order to test the stability of our method, we next add random noise to the synthetic data. The noise is generated from a pseudo-random routine with zero mean, which has been numerically filtered by a bandpass with frequencies determined by the frequency range of the synthetic waveforms. The amount of noise is expressed as the ratio of its energy to the energy of the synthetic P-wave train. The calculated Q_p^{-1} logs for the noise-free case, the 15% noise case, and the 15% noise case after

smoothing over depth with 19-point median filter are illustrated in Figure 4.5. Depth points are 0.152 m apart, so 19 depth points correspond to one 3.05 m depth interval. It can be seen that the method is robust up to 15% noise level, which is adequate for our purposes, as the noise levels in the actual ODP sonic data are less than 10%.

4.4 APPLICATION TO DATA

We next apply our technique to data from ODP Hole 806B and 807A. Hole 806B was logged in 2520 m of water from 120 meters below seafloor (mbsf) to approximately 700 mbsf. (During ODP logging operations the bottom of the drillpipe is typically left at about 100 mbsf to avoid the possibility of the pipe dragging off the hole in poorly consolidated near-seafloor sediments.) We use a fixed window length to extract the P-wavetrain from the full waveforms. The edges of the window are tapered using a cosine taper. It is important to correctly select window position. In our program, we determine P-wave first arrival and borehole fluid wave positions by waveform changes, and then set the window position. Second, we calculate P-wave spectra from 120 m to 720 m at the depth interval of 0.152 m. Considering the relatively narrow bandwidth of the LSS tool, we use the P-wave amplitude spectra in a frequency range from 5 kHz to 25 kHz. The key step is to obtain $\hat{\Phi}(z)$ by equations (9)-(13), from which we can extract the P-wave attenuation (Q_p^{-1}) log. It should be emphasized that using median shifting makes this method robust. The reference waveform depth point and Q_p^{-1} at the reference depth point are selected on the basis of geological conditions. Most of the data we used are from soft carbonate sediments, in which shear wave velocity is less than fluid velocity. From other experiments (Fu *et al.* 1996), we know the quality factor (Q_p) of shallow ocean bottom carbonate sediments is on the order of $80 \sim 100$. Thus we chose the reference depth as the $\hat{\Phi}(z)$ profile showing maximum (corresponding to a minimum of attenuation). Finally we

set $Q_p = 100$ and recover the Q_p^{-1} log. Averaged by 2.44 m, 3.05 m, 3.05 m, and 3.66 m medians, the four Q_p^{-1} logs from different source-receiver pairs (2.44 m, 3.05 m, 3.05 m, and 3.66 m) at the same time window lengths are virtually identical (Figure 4.6). Finally, we calculate one Q_p^{-1} log with depth by taking a median of the four Q_p^{-1} logs at each depth.

In order to better understand the sensitivity of the results from real data to some of our initial parameters we repeated the inversion process several times. Calculated Q_p^{-1} logs using different window lengths (150 μsec, 200 μsec, 250 μsec, and 300 μsec) show that small differences in window length do not seriously affect results (Figure 4.7). However, care must still be taken in choosing a window length. In shallow ocean bottom sediments a pure P-wavetrain is difficult to obtain since the P-wave velocity is close to the borehole fluid velocity. If the window length is too long, the shallow Q_p^{-1} estimation is incorrect, although it may not affect the deep Q_p^{-1} estimation (Figure 4.7). The effects of varying the value of Q_p^{-1} at the reference depth are shown in Figure 4.8. Setting Q_p^{-1} equal to zero at the reference depth (dashed line) gives a lower bound profile of attenuation and thus an upper bound profile of Q_p. The solid and dotted lines are for reference attenuations of 0.01 and 0.02, respectively.

An upper bound for the estimated error in Q_p^{-1}, assuming $Q_p = 100$ at the reference depth, is shown in Figure 4.9. The left curve in Figure 4.9 is the difference between Q_p^{-1} values obtained from synthetic waveforms with Poisson's ratios of 0.35 and 0.45. The right curve is the attenuation profile used to compute the synthetics.

Waveforms from hole 807A were inverted for Q_P^{-1} following the same procedure used for hole 806B data. Figure 4.10 shows that the derived Q_P^{-1} logs are similar with different window sizes. The P-velocity profile is plotted in the fourth column in the figure. It can be seen that the attenuation profiles from both holes separated by 450 km exhibit remarkable similarity. Both begin with relative low attenuation gradually

increasing with depth to a maximum at around 350 mbsf. Then the attenuation decreases with depth.

4.5 CONCLUSIONS

A method has been presented in this chapter to estimate *in situ* P-wave attenuation from full waveform acoustic logs. It has the following advantages:

1. In this method, the geometrical spreading and coupling terms are considered to depend on frequency. We, however, need not know specific functional forms they have. Numerical tests and real data processing show that the method can effectively reduce effects of the geometrical spreading and source-receiver's coupling functions in relation to frequency.

2. The P-wave amplitude spectrum depends largely on Q_p^{-1}. But the window size for a P-wavetrain does not significantly affect the Q_P estimation. The best window length is about 200 μsec for the ODP data we examined.

3. Numerical tests on effects of noise show that in spite of the presence of 15% noise, the results given by the method are acceptable.

4. A relative Q_p^{-1} log can be obtained from a family of data from one source-receiver pair. Q_p^{-1} is an average of the interval between the source and the receiver.

5. Agreement of the four Q_p^{-1} logs which were computed independently using data from four different source-receiver pairs suggests that the method is robust and practical.

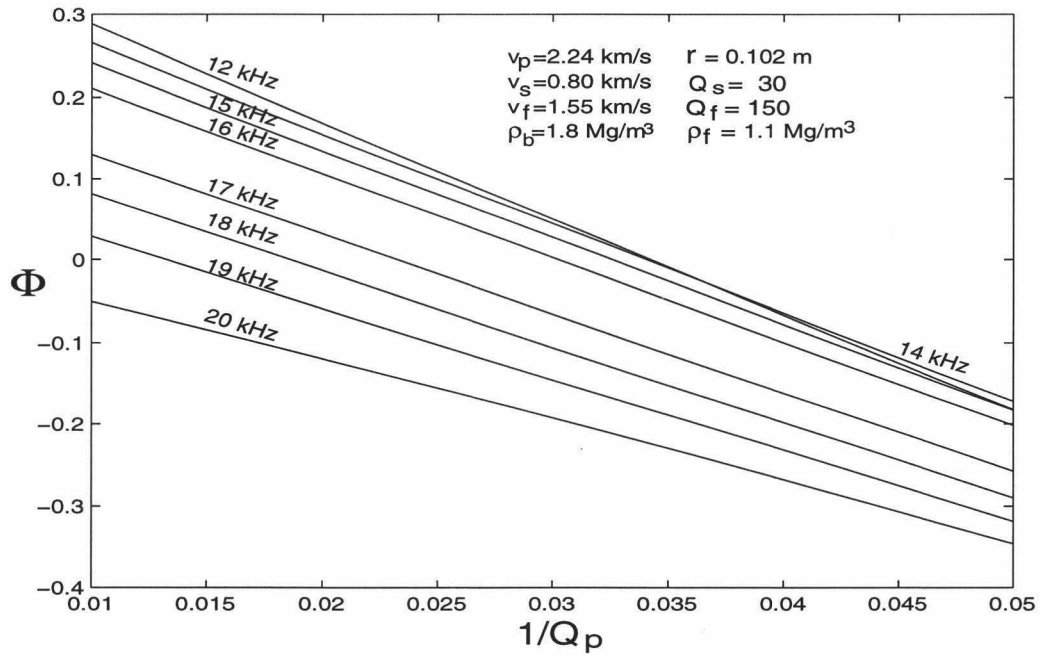

Figure 4.1: Validation of equation (3) using synthetic data. Here Φ calculated from full-wave synthetics is plotted as a function of Q_p^{-1} at different frequencies. The source-receiver separation is 3.05 m (10 ft).

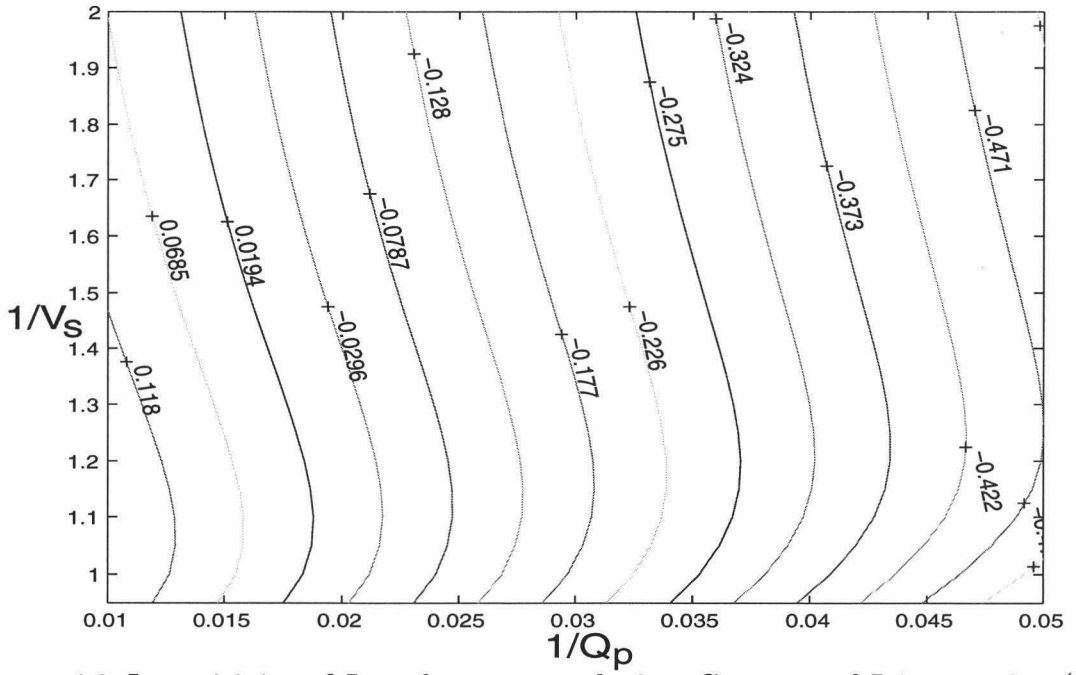

Figure 4.2: Insensitivity of Φ to shear wave velocity: Contours of Φ in equation (3) as a function of Q_P^{-1} and v_s^{-1} at 10 kHz for synthetic data. Formation parameters were fixed as shown on Figure 4.1.

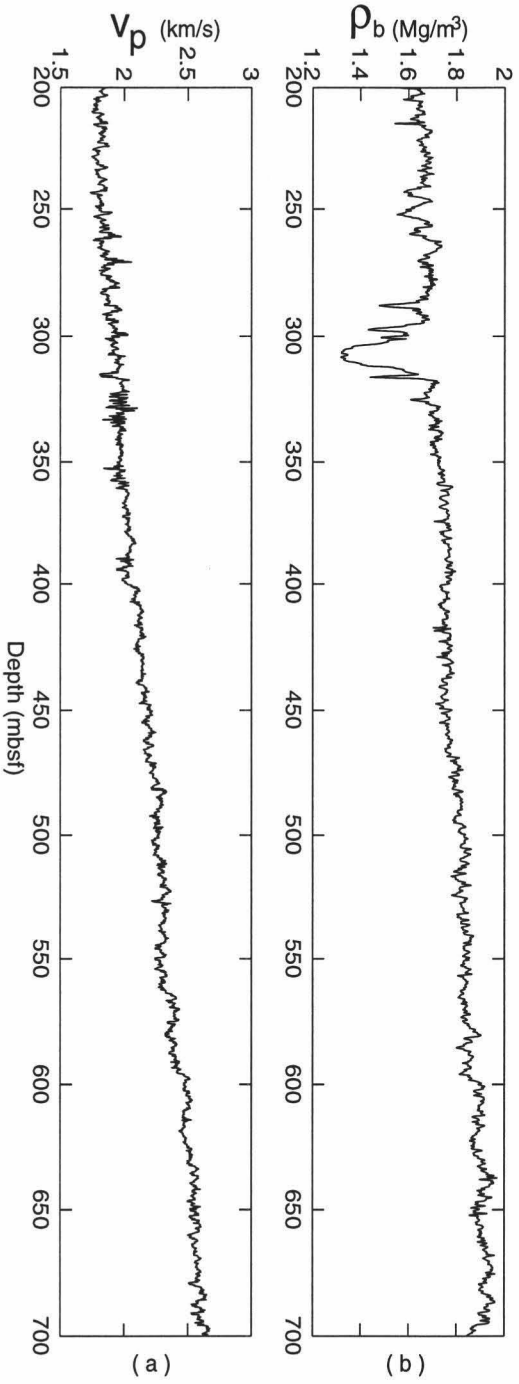

Figure 4.3: Velocity (a) and density (b) logs taken from ODP site 806B.

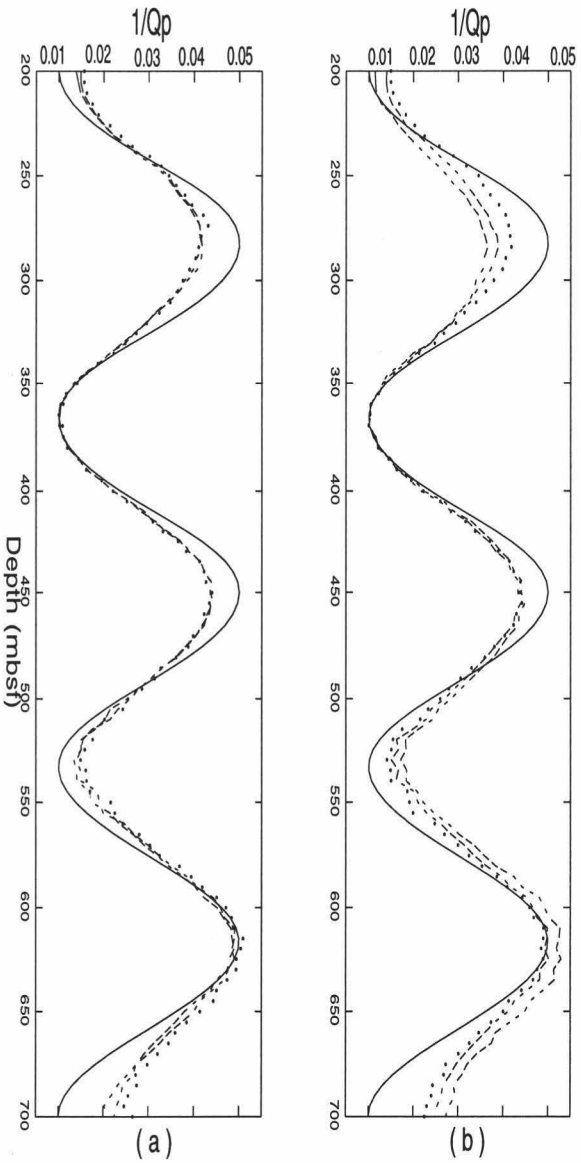

Figure 4.4: Comparison of the inverted attenuation Q_P^{-1} from synthetic data with the assumed attenuation (solid line) (a) the Q_P^{-1} logs calculated from the synthetic data with offset 2.44 (dotted lines), 3.05 (dashed line), and 3.66 m (dash-dotted line) and a fixed Poisson's ratio 0.3.; (b) the Q_P^{-1} logs calculated for offset 3.05 m with Poisson's ratio 0.3 (dotted line), 0.35 (dashed line) and 0.4 (dash-dotted line).

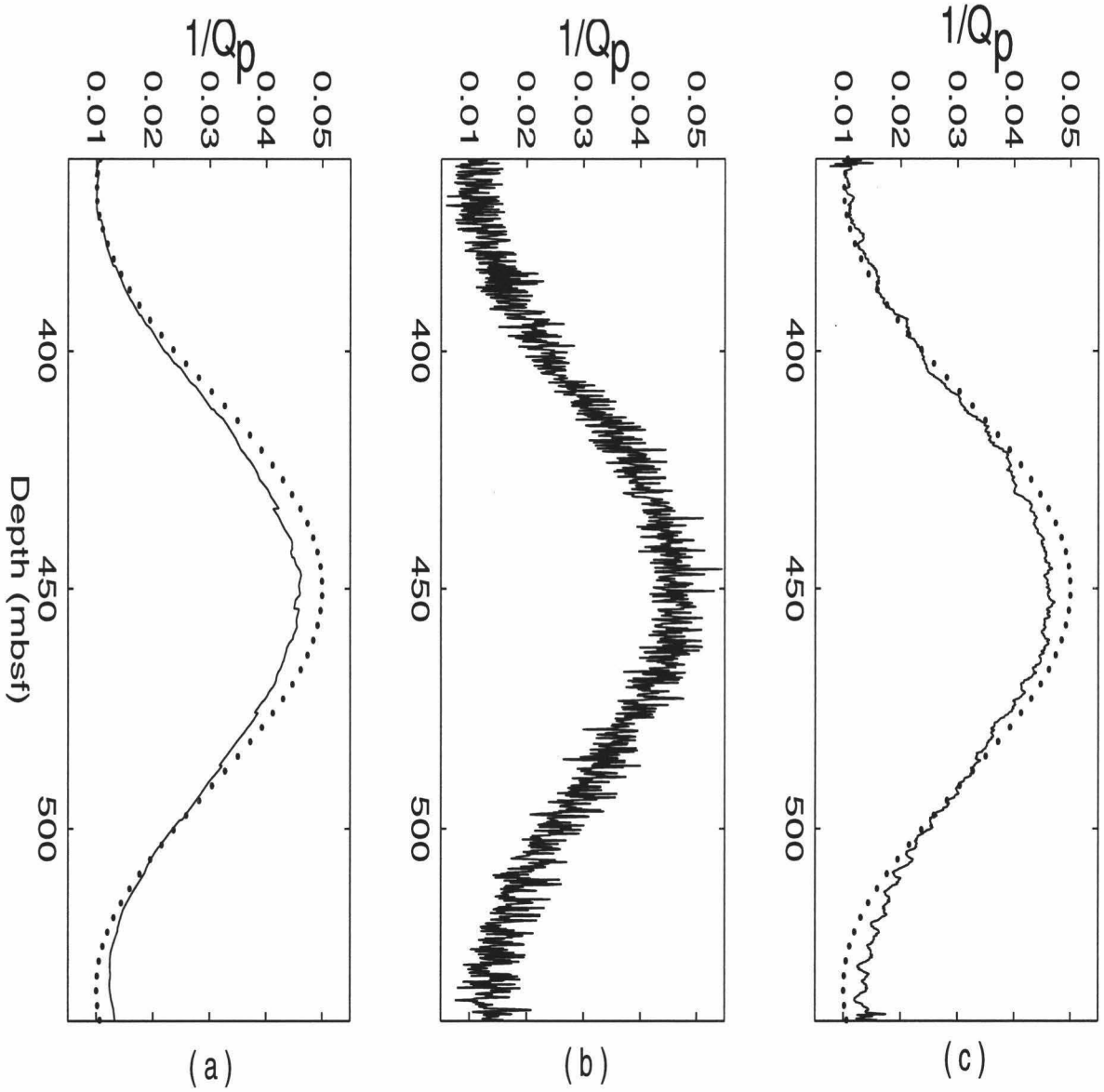

Figure 4.5: Effects of noise on the attenuation estimation. The dotted line is true attenuation Q_P^{-1}; The synthetic waveforms were calculated at each 6 inches depth interval, same as the field data. The source-receiver spacing 3.05 m (10 ft) and a Poisson's ratio 0.3 were used in the synthetics. (a) Noise-free case, (b) 15% noise, and (c) 15% noise after smoothing over depth with a median filter equal to the source-receiver spacing.

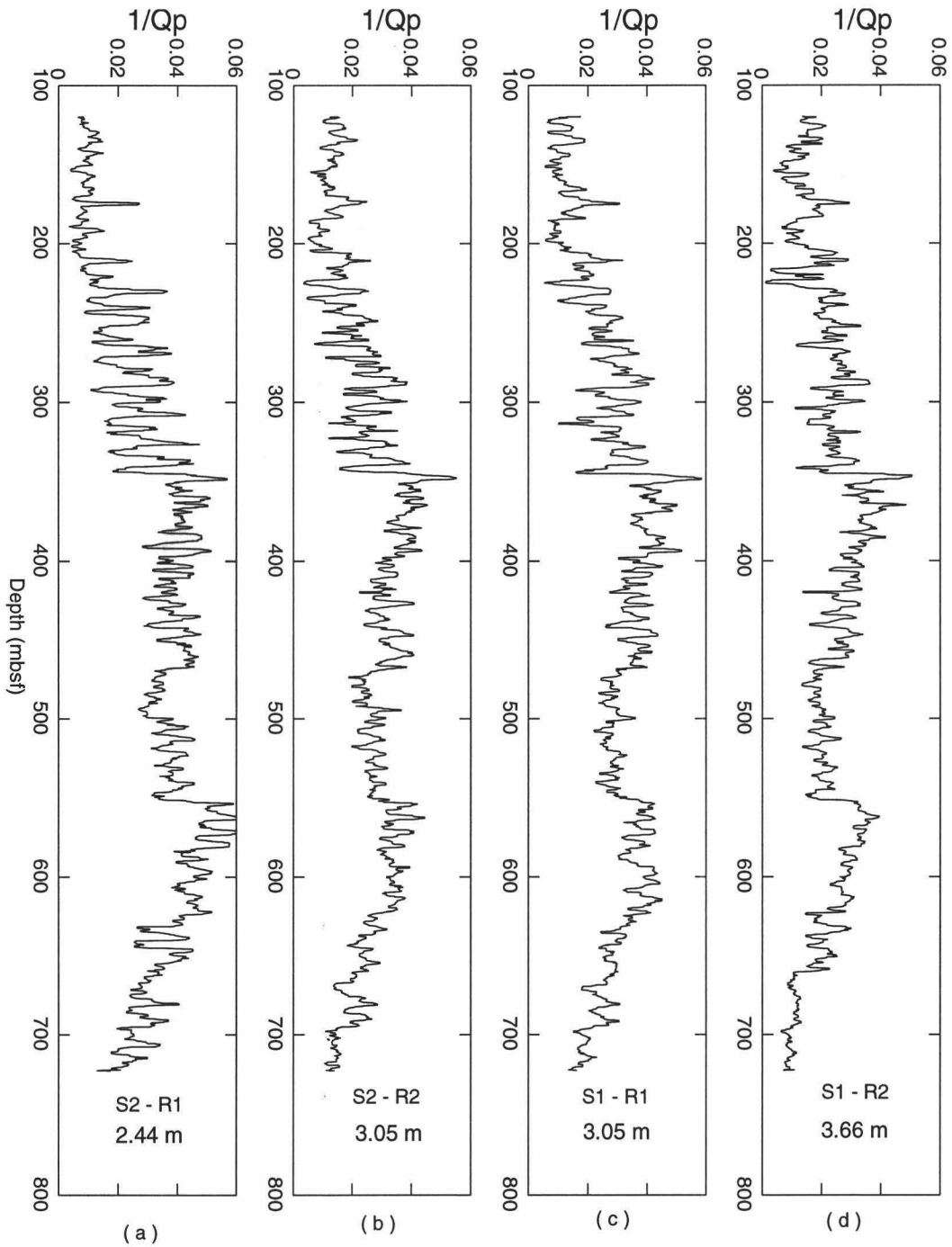

Figure 4.6: Four Q_P^{-1} logs inverted from four data set independently from ODP hole 806B. The P-wave train was taken by a window length of 200 μs. The source-receiver pair is (a) S2-R1 (2.44 m) (b) S2-R2 (3.05 m), (c) S1-R1 (3.05 m), and (d) S1-R2 (3.66 m).

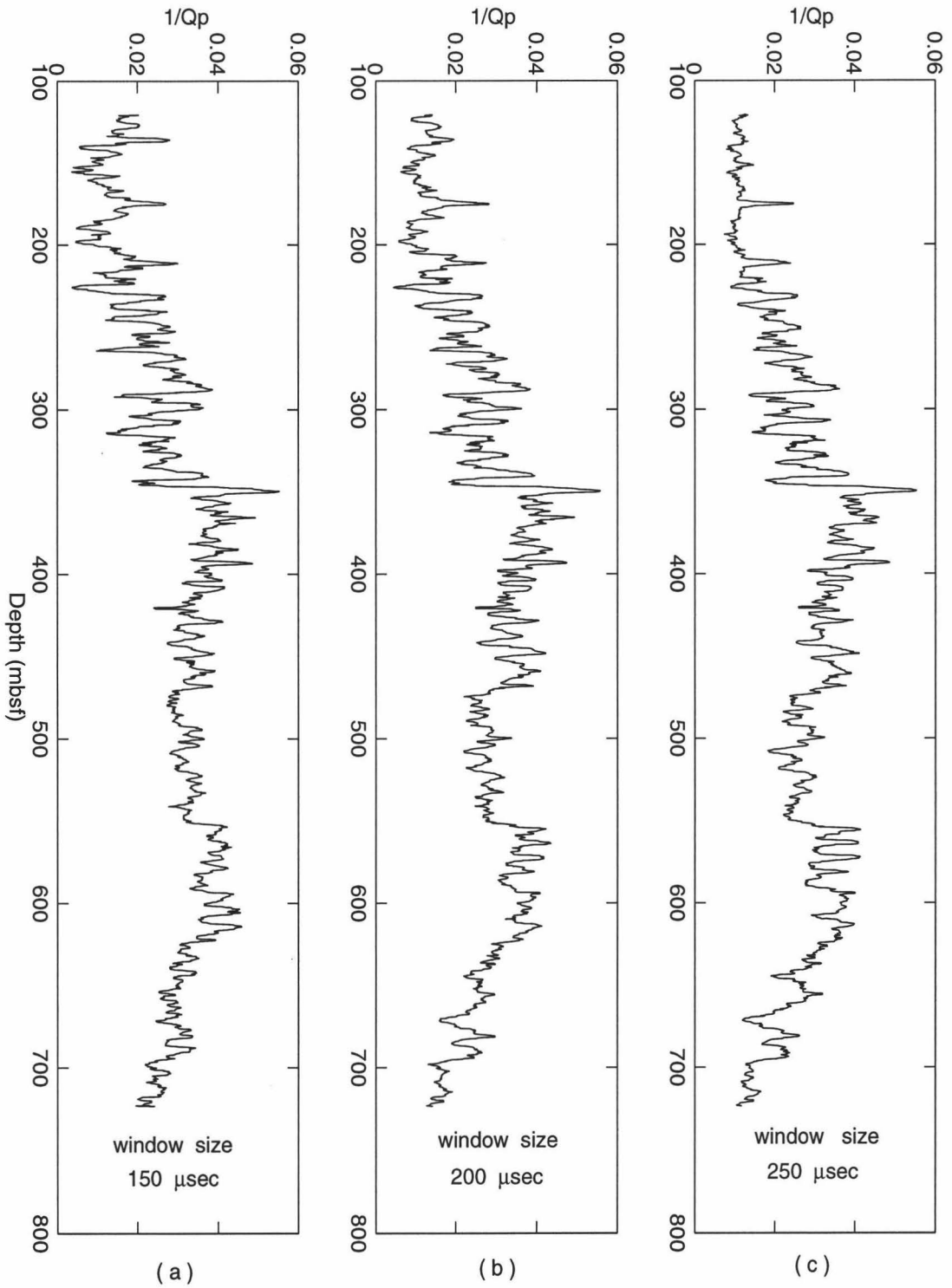

Figure 4.7: Effects of time window size on the attenuation estimates. (a) window size 150 μs, (b) 200 μs, and (c) 250 μs.

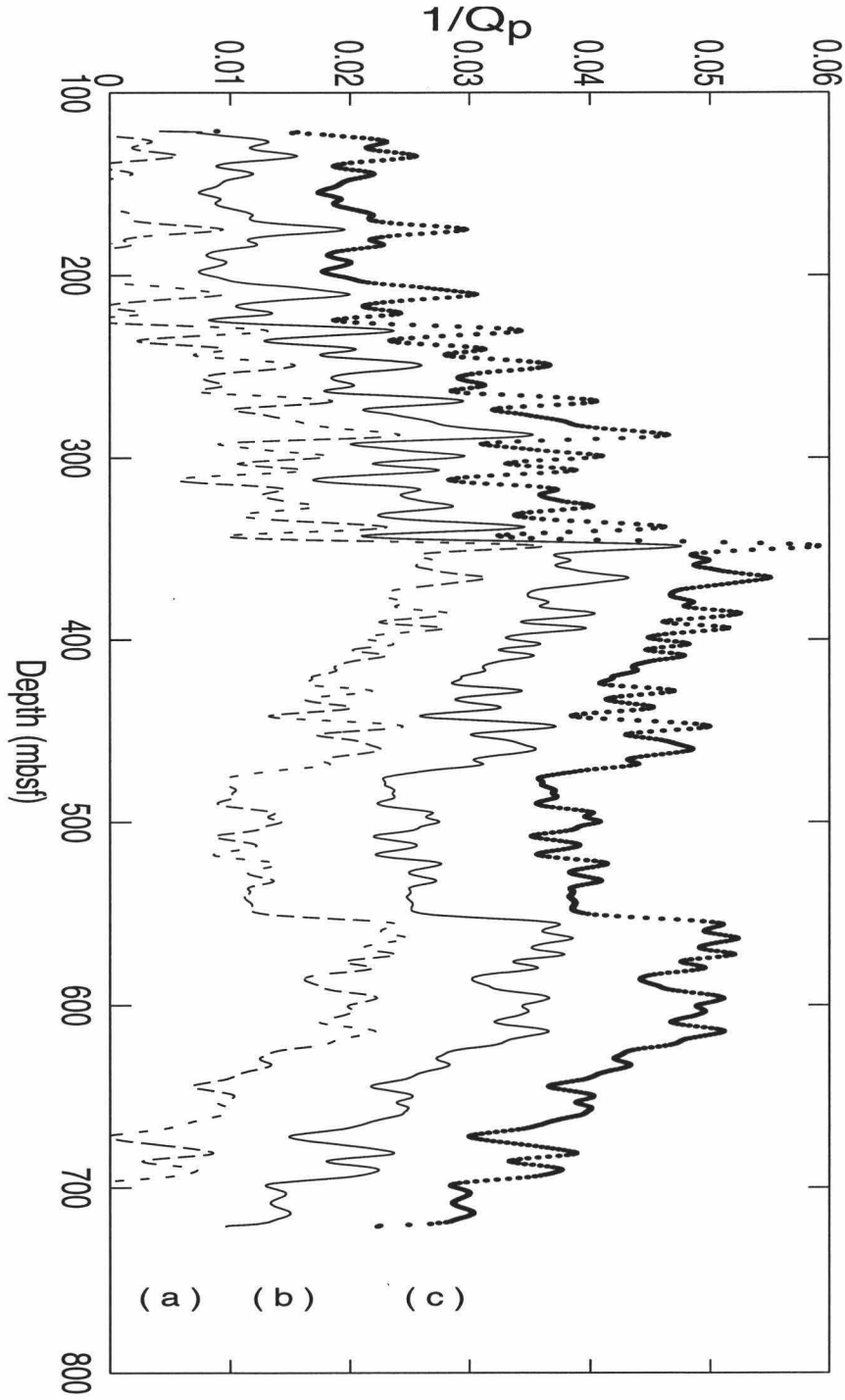

Figure 4.8: Effect of the reference attenuation value on the inverted results. Using different reference values gives different results. The dashed line for a reference Q_P^{-1} of zero; solid line is for a reference Q_P^{-1} of 0.01; and dotted line for a reference Q_P^{-1} of 0.02. The results have been filtered with a median over 9.15 m.

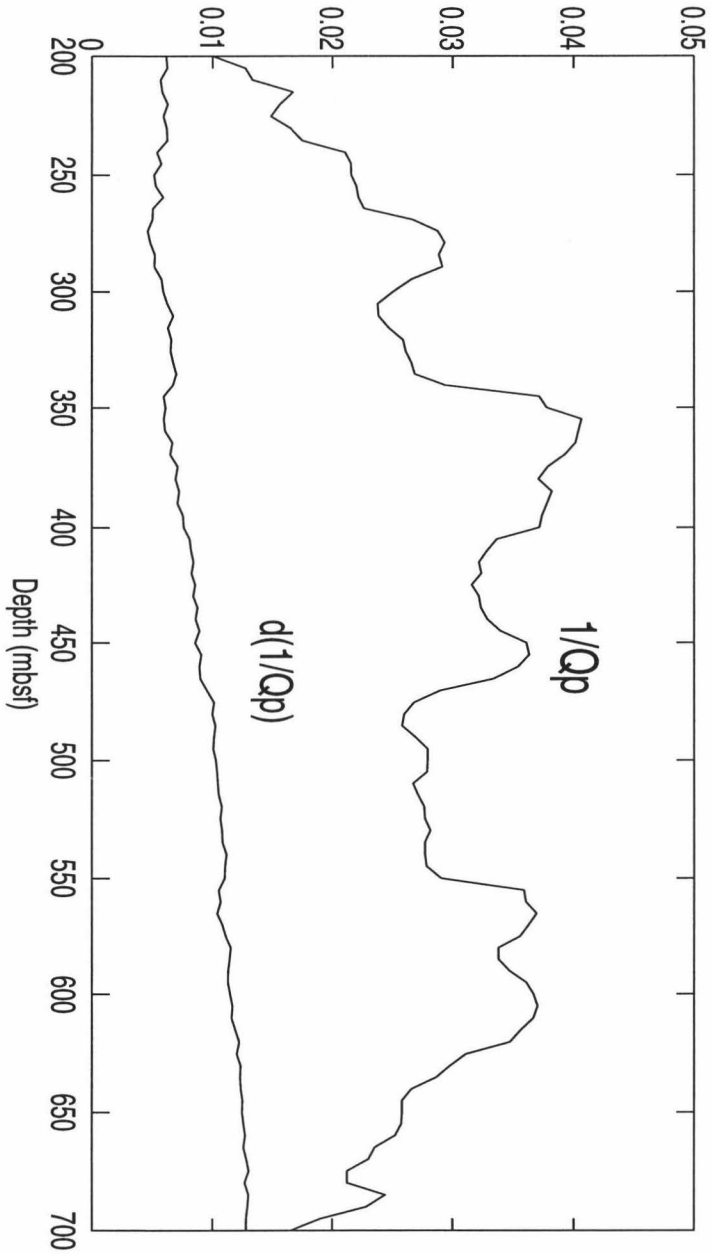

Figure 4.9: Effect of unknown S-wave velocity on the inverted Q_P^{-1} results. The left line shows the jump in Q_P^{-1} due to the variation of Poisson's ratio form 0.35 to 0.45. The calculation was made using Q_P^{-1} log shown on the right.

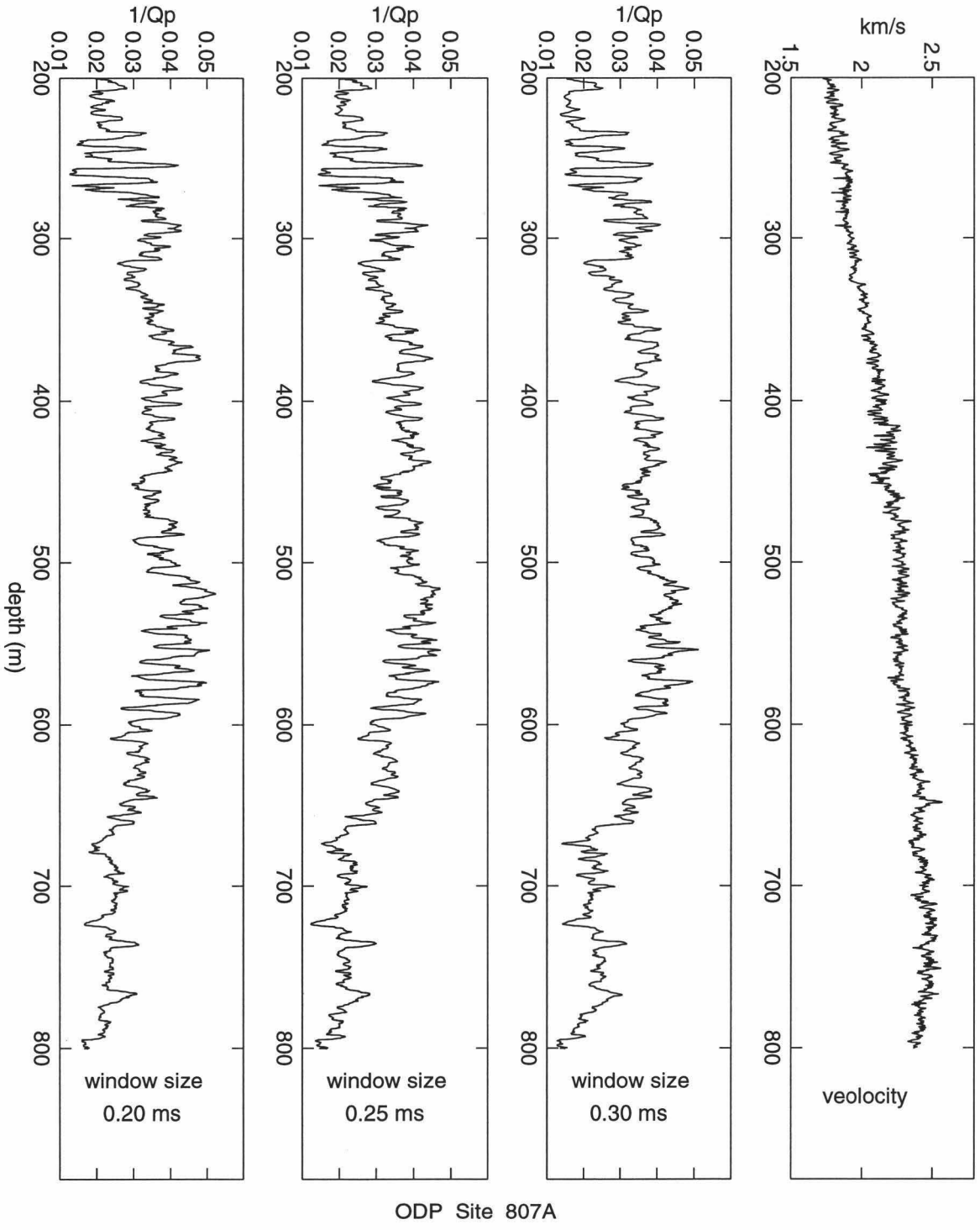

Figure 4.10: The attenuation profiles calculated from another field data set from ODP hole 807a, 450 km far from hole 806B. The attenuation logs (Q_P^{-1}) were calculated from the source-receiver offset 10 ft pair data set with a window length (a) 200 μs, (b) 250 μs, and (c) 300μs. (d) the velocity profile at ODP 807a.

4.6 REFERENCES

Cheng, C.H., 1989. Full waveform inversion of P waves for V_s and Q_p, *Geophys. J. R. astron. Soc.*, **94**, 15619-15625.

Cheng, C.H., Toksoz, M.N., and Wills, M.E., 1982. Determination of *in situ* attenuation from full waveform acoustic logs, *J. Geophys. Res.* , **87**, 5477-5484.

Courtney, R.C., 1993. Calculation of acoustic parameters by a filter-correlation method,*J. Acoust. Soc. Am.*, **97**, 1145-1154.

Frazer, L. N., Sun, X., and Wilkens, R. H., 1997, Changes in attenuation with depth in an ocean carbonate section: ODP sites 806 and 807, Ontong Java Plateau: J. Geophys. Res., **102**, 2983-2997.

Fu, S. S., R. H. Wilkens, and L. N. Frazer, Acoustic lance: New *in situ* seafloor velocity profiles, *J. Acoust. Soc. Am.*, **99**, 234-242, 1996.

Paillet, F. and Cheng, C.H., 1991. *Acoustic Waves in Boreholes*, CRC Press, N.Y., pp. 253.

Quan, Y, Harris, J.M., and Chen, X.F.,1994. Acoustic attenuation logging using centroid frequency shift and amplitude ratio methods: A numerical study, *64th Annual Internat. Mtg., Soc. Expl. Geophys., Expanded Abstracts*, Soc. Expl. Geophys ., 8-11.

Sams, M. and Goldberg, D., 1990. The validity of Q estimations from borehole data using spectral ratios, *Geophysics*, **55**, 97-101.

Tonn, R., 1991. The determination of the seismic quality factor Q from VSP data: a comparison of different computational methods,*Geophysical Prospecting*, **39**, 1-27.

Tsang, L. and Rader, D., 1979. Numerical evaluation of transient acoustic waveforms due to a point source in a fluid-filled borehole, *Geophysics*, **44**, 1706-1720.

Urmos, J., and Wilkens, R.H., 1993. *In situ* velocities in pelagic carbonates: new insights from Ocean Drilling Program Leg 130, Ontong Java Plateau, *J. Geophys. Res.*, **98**, 7903-7920.

Urmos, J., Wilkens, R.H., Bassinot, F., Lyle, M., Marsters, J., Mayer, L., and Mosher, M., 1993. Laboratory and well-log velocity and density measurements from the Ontong Java Plateau: New *in situ* corrections to laboratory data for pelagic carbonates, Proc. ODP, Sci. Results, **130**, 607-622.

Wilkens, R.H., Cheng, C.H., and Meredith, J.A., 1992. Evaluation and prediction of shear wave velocities in calcareous marine sediment and rocks, *J. Geophys. Res.*, **97**, 9297-9305.

Chapter 5
In-situ P- and S-wave attenuation logs from monopole sonic data

5.1 SUMMARY

In this Chapter, a modification of the method of Chapter 4 for relative P-wave attenuation estimation is proposed. In the modified method the variation of wave amplitudes related to changes in formation properties with depth is accounted for by the use of synthetic log data. The method first calculates an attenuation profile from a single source-receiver pair by assuming a reference attenuation value at some depth. Then the errors of the attenuation profile caused by the inaccurate reference value can be corrected from multiple receiver gathers provided the receiver responses are identical. Synthetic tests show that the P- and S-wave attenuation values estimated from synthetic waveforms are in good agreement with their respective model values.

In-situ P- and S-wave attenuation profiles provide valuable information about reservoir rock properties and formation damage induced during and by the drilling process. Field data processing results show that the modified method gives robust estimates of intrinsic attenuation. The attenuation profiles calculated independently from each waveform of an eight receiver array are consistent with one another. In fast formations where S-wave velocity exceeds the borehole fluid velocity, both P-wave attenuation (Q_P^{-1}) and S-wave attenuation (Q_S^{-1}) profiles can be obtained. P- and S-wave attenuation profiles and their comparisons are presented for three reservoirs. Their correlations with formation lithology, permeability, and fractures are also presented.

5.2 INTRODUCTION

The amplitude of acoustic waves propagating in a borehole penetrating an earth formation decreases with travel distance due to geometrical spreading, scattering, and intrinsic attenuation. The intrinsic attenuation is closely related to the petrophysical properties of subsurface formations, and it can be used for lithology and reservoir interpretation (Klimentos and McCann, 1990; Klimentos, 1995). The full waveform measurement in the borehole provides an effective means to directly obtain in-situ estimates of formation intrinsic attenuation. Existing methods of attenuation determination from acoustic logging data include spectral ratio (Cheng et al., 1982; Sams and Goldberg, 1990; Tonn, 1991; Neep, 1995), centroid frequency shift (Quan et al., 1994; Neep et al., 1996), filter correlation (Courtney, 1993), partition coefficients, and waveform inversion (Paillet and Cheng, 1991; Tang, 1995). Most of these methods calculate attenuation over the span of the receiver array. The receiver responses are assumed to be identical. However, effects such as receiver mismatch, borehole irregularity, off-centered tool, and geometrical spreading, etc., can significantly degrade the results of attenuation estimation.

In estimating in-situ intrinsic attenuation, these effects have to be taken into account. In reality, however, they are difficult to correct for. We propose a method to suppress these unwanted effects and improve the results of attenuation estimation.

A method for estimating relative attenuation was developed in Chapter 4 for Ocean Drilling Program (ODP) sonic logging data. The drawback with this method is the assumption that the effects of density and velocity variations on geometrical spreading can be neglected in the estimation of wave attenuation. Synthetic tests show that this assumption introduces errors into the estimation of attenuation in slow formations (rock with shear velocity less than borehole fluid velocity). For fast formations, good results of P-wave attenuation would not be obtained without cor-

recting the geometrical spreading. Moreover, absolute attenuation was not given in the previous method. In this Chapter, we will first review the method for estimating relative P-wave attenuation. Then we will propose a modification by reducing the effect of geometrical spreading. Furthermore, we will simplify the modified method and present a practical implementation of the method. We will also provide a correction to obtain absolute attenuation. Finally, we will apply the method to the estimation of P- and S-wave attenuations in fast formations. We will show some useful lithological indications and reservoir features from the attenuation profiles.

5.3 ALGORITHM OF ATTENUATION DETERMINATION

A monopole array acoustic tool generally consists of one monopole source (transmitter) and an array of receivers. Each receiver records a waveform generated by the transmitter at each depth. The amplitude spectrum of the P-wavetrain recorded by the i-th receiver can be written as

$$X_i(z,\omega) = S(\omega)C_S(\omega, z+\frac{1}{2}d_i)R_i(\omega)C_{R_i}(\omega, z-\frac{1}{2}d_i)G_i(\omega, z, d_i)\exp[-\frac{\omega}{2}Q_P^{-1}(z)\Delta t_i(z)], \tag{1}$$

where ω is angular frequency; S and R_i are the spectra of the source and the instrument responses of the i-th receiver on the tool; d_i is the offset between the source and the i-th receiver; z is the depth referred to the center point between the source and the i-th receiver; Δt_i is the traveltime of P-wave in the formation, which is approximately equal to d_i/v_p, where v_p is formation P-wave velocity. Q_P^{-1} is an average of attenuation over the source-receiver offset d_i. The couplings(C_S) of the source and (C_{R_i}) of the i-th receiver to the borehole are frequency-dependent. They include the attenuation of the P-wave during transmission through the fluid annulus between the tool and borehole wall. The geometrical spreading (G_i) is a function of frequency ω,

depth z and offset d_i (Paillet and Cheng, 1991; Sams and Goldberg, 1990; Quan et al., 1994).

Rearranging equation (1) and taking its natural logarithm give

$$\frac{2\ln X_i}{\omega} = -Q_P^{-1}\Delta t_i + \frac{2\ln(SC_S R_i C_{R_i} G_i)}{\omega}. \tag{2}$$

On the right side of the above equation, the first term depends only on z (assuming Q_P^{-1} is independent of ω). For commercial array sonic tools (e.g., MAC/XMAC, DSI, etc.) the frequency of monopole waves is usually below 30 kHz and the source-receiver offset ($> 3.2m$) is long compared to borehole size ($\sim 0.25m$). The P-wave amplitude variation caused by the formation intrinsic attenuation dominates over other factors.

The original method for relative attenuation estimation was developed for ODP data taken in soft marine sediments with the Schlumberger Long-Spaced Sonic (LSS) tool. A brief summary of the original method is given next.

5.3.1 Original Method

To extract P-wave attenuation (Q_P^{-1}) from the ODP data, the dependence of G in equation (2) on depth z was neglected, thus equation (2) can be written as

$$\Phi(z,\omega) = \phi(z) + A(\omega), \tag{3}$$

where $\Phi(z,\omega) = \frac{2\ln X_i}{\omega}$, $\phi(z) = -Q_P^{-1}\Delta t_i$, and $A(\omega) = \frac{2\ln SC_s R_i C_{R_i} G}{\omega}$. Obviously, $\phi(z)$ is what we want to estimate. To extract $\phi(z)$ from $\Phi(z,\omega)$, we use a combination of a mean and two medians rather than a single mean of Φ over frequency ω. This is because the second term A in the right side of equation (3) depends not only on ω but also weakly on z.

In practice, $\Phi(z,\omega)$ is a matrix with m rows and n columns, where $z = z_1,\ldots,z_m; \omega = \omega_1,\ldots,\omega_n$. The median value of the elements in each column of Φ is written as:

$$\tilde{\Phi}(\omega) = \underset{z}{median}\, \Phi(z,\omega),$$

with a similar formula for the mean value.

First, we average $\Phi(z,\omega)$ over frequency ω,

$$\bar{\Phi}(z) = \underset{\omega}{mean}\, \Phi(z,\omega). \tag{4}$$

Then we estimate the frequency-dependent portion of $A(\omega)$ by calculating the median depth shift of each Φ from the average,

$$\Delta\tilde{\Phi}(\omega) = \underset{z}{median} \left\{\Phi(z,\omega) - \bar{\Phi}(z)\right\}. \tag{5}$$

Next we take the ω-median of the ω-shifted Φ,

$$\hat{\Phi}(z) = \underset{\omega}{median} \left\{\Phi(z,\omega) - \Delta\tilde{\Phi}(\omega)\right\}. \tag{6}$$

The result $\hat{\Phi}(z)$ is an estimate of $-Q_P^{-1}\Delta t_i(z)$ plus an unknown constant $\hat{A}$,

$$\hat{\Phi}(z) = -Q_P^{-1}(z)\Delta t_i(z) + \hat{A}. \tag{7}$$

Finally we solve Q_P^{-1} from the above equation by assuming a value of Q_P at some reference depth ζ, say, $Q_P(\zeta) = 100$,

$$Q_P^{-1}(z) = \frac{\hat{A} - \hat{\Phi}(z)}{\Delta t_i(z)} = \frac{\hat{\Phi}(\zeta) - \hat{\Phi}(z) + Q_P^{-1}(\zeta)\Delta t_i(\zeta)}{\Delta t_i(z)}. \tag{8}$$

The essence of the original method is using mean and median average methods over depth and frequency to extract an attenuation profile from the common receiver data set. The drawback with the original method is that the estimated P-wave attenuation is biased from the true value, because the second term on the right side of

equation (3) depends on depth. As shown in Chapter 4, in slow formations, compared with the first term on the right side of equation (3), the depth-dependence of the term A is weak and negligible. For fast formations, however, the depth-dependence of the term A can not be neglected. To address the problem, the following modified method is proposed.

5.3.2 New Method

From the term A in equation (3), it can be assumed that the source and receiver wavelets and couplings are independent of depth. The geometrical spreading G is a function of depth, frequency, and offset. If we reduce the dependence of G on depth, the above mentioned bias will be reduced.

Using synthetic data, we can estimate the geometrical spreading G. We calculate synthetic waveforms without introducing attenuation; in this case, the term $\phi(z)$ in equation (3) vanishes. For the synthetic data, equation (3) can be written as

$$\Phi^{syn}(z,\omega) = A^{syn}(z,\omega). \tag{9}$$

The above equation simulates the P-wave amplitude variation with depth due to borehole and formation changes (i.e., the geometrical spreading effect). In other words, the variation of P-wave amplitudes caused by geometrical spreading can be estimated using equation (9). It is this variation that causes the bias of the attenuation estimates in the original method. Using equation (9), this variation can be separated from the intrinsic attenuation.

Taking the difference between equation (3) and equation (9) gives

$$\Delta\Phi_i(z,\omega) = \phi_i(z) + \Delta A_i(z,\omega), \tag{10}$$

where

$$\Delta\Phi_i = \frac{2\ln X_i}{\omega} - \frac{2\ln X_i^{syn}}{\omega},$$

$$\phi_i = -Q_P^{-1}\Delta t_i,$$

$$\Delta A_i = \frac{2\ln(SC_sR_iC_{R_i}G_i)}{\omega} - \frac{2\ln[(SC_sR_iC_{R_i})^{syn}G_i^{syn}]}{\omega}.$$

The purpose of the above modification is to make $\Delta A_i(z,\omega)$ less variable with depth so that the depth-dependence of equation (10) is dominated by the first term $\phi_i(z)$ at the right side of the equation. It should be noted that there is no requirement that the source-receiver responses in both synthetic data and real data be perfectly matched, because they are assumed to be depth-independent. It is only necessary that both responses occupy approximately the same frequency band.

Applying the same mean and median average procedures to equation (10), we can extract $\phi_i(z)$ from $\Delta\Phi_i(z,\omega)$. Then the attenuation can be solved from $\phi_i(z)$. In the following, we use synthetic data to test the modified attenuation estimation method.

5.4 ATTENUATION FROM SYNTHETIC DATA

The modified method is first tested on synthetic data. We assume a simple axisymmetric fluid-filled borehole of radius R_b surrounded by an isotropic solid formation. The synthetic data were computed by using the frequency-wavenumber method of Cheng (1989), with various enhancements such as causal attenuation, complex frequencies, and Filon integration.

The attenuation is introduced by making the seismic velocities complex. The use of complex velocities is equivalent to the assumption of visco-elastic properties for the solid and fluid. The imaginary parts of the velocities are related to attenuation(Q^{-1}). To maintain causality with the constant Q assumption, the log-

arithmic dispersion law is used (Aki and Richards, 1980). The total transformation for the complex velocities is

$$v(\omega) = v(\omega_0)[1 + \frac{1}{\pi Q}\ln(\frac{\omega}{\omega_0})](1 + \frac{i}{2Q})^{-1}, \tag{11}$$

where Q is the quality factor for either P- or S-wave, v is either P- or S-wave velocity, and ω_0 is an arbitrary reference frequency. Neglecting second and higher terms in 1/Q in equation (11) gives the same expression as Aki and Richard (1980) did.

An effective way to check the accuracy of the modified method is to test it with synthetic waveforms computed from well logging data. These data are shown in Figure 5.1 for a depth range from 4740 to 5260 m. They are P- and S-wave slowness, density, and caliper logs. The caliper log will be used to test borehole size effects. P- and S-wave attenuation values were estimated from full-waveform data using the original method. The fluid velocity (v_{fl}) is taken as 1.5 km/s. The quality factor of the fluid is assumed to be 30. The fluid density is 1.0 Mg/m^3. Using the log data and the attenuation values, we calculate synthetic waveforms for three receiver offsets: 3.2, 3.66, and 4.27 m.

The synthetic data with a source-receiver offset of 3.2 m are plotted in Figure 5.2. For comparison, a field data set for receiver 1 with the same source-receiver offset is plotted in Figure 5.3. The formation parameters used in the synthetics are the same as those in field data except for borehole size and attenuation. A Ricker wavelet is used as a source wavelet in the synthetics. The window lengths for both P- and S-wave attenuation estimation are shown in both figures. Similar features of P- and S- head wavetrains can be found in both figures. We did not consider the presence of the tool in synthetics, this effect will be shown to have little impact on our method.

Next we apply the mean and median average method to the synthetic data with equations (3) and (10) to obtain the P-wave attenuation profiles. The results

are shown along with the actual attenuation Q_P^{-1} input into the model (Figure 5.4). From the first column, we see that the attenuation values estimated using equation (3) are biased from input values, which is mainly caused by the variation of the term A with depth. Using equation (10), the agreement between the estimated and input Q_P^{-1} values is significantly improved. This is because the variation of P-wave amplitudes caused by formation intrinsic attenuation is now effectively separated from that caused by other effects. Consequently, a more accurate and robust attenuation profile is obtained.

5.4.1 Windowing effects

It is worthwhile mentioning that a correct selection of window position is important. In general, P-wave attenuation estimation is sensitive to the time window size. We discuss the effect of window size on the estimation of attenuation. Here we use the ray path theory to predict the first arrivals of P- and S-waves for synthetic data using the following formula:

$$T_a = \frac{2R_b}{\cos(\theta)v_{fl}} + \frac{d_i - 2R_b\tan(\theta)}{v}, \tag{12}$$
$$\theta = \arcsin(\frac{v_{fl}}{v}),$$

where v is velocity for either P- or S-wave.

Generally speaking, the window length has some effect on the estimation of attenuation from sonic logging data, especially when the P-wave velocity is very low, as shown in Chapter 4. To test the sensitivity of our method to window length, we use various time window lengths: 120, 240, and 360 μs, respectively, for both P- and S-wave attenuation estimation. Both edges of the window are smoothed with a cosine taper. The results are shown in Figures 5.5 and 5.6. It can be seen that

changes of the window size have a small but measurable effect on the estimates of P-wave attenuation. However, the effect of window size on the estimates of S-wave attenuation is minimal. The testing shows that for fast formations, a window length of 240 μs is adequate for both P- and S-wave attenuation estimations.

5.4.2 Borehole fluid velocity and attenuation effects

In practice, an accurate borehole fluid velocity may not be available. Various muds of different acoustic properties are used for drilling. The mud velocity is usually lower than that of water. To test the borehole fluid velocity effect on our modified method, we use a borehole fluid velocity of 1.13 km/s to generate synthetics but assumed a fluid velocity of 1.5 km/s in our inversion procedure. Other parameters used in the synthetic data are the same as before. We calculate P- and S- wave attenuation logs from the synthetic data. The results are almost the same as those with a borehole fluid velocity of 1.5 km/s. This is because the borehole fluid velocity is a constant value, it does not significantly influence the depth variation of the P- and S-wave geometrical spreading.

The borehole fluid attenuation is a little more difficult to obtain. Various muds used for drilling might have different attenuation values. To test the borehole fluid attenuation effect on our attenuation estimates, we calculate two synthetic data sets with a fixed Q_f of 30 and 100, respectively. The other parameters used in the two data sets are the same as before. Using our inversion procedure with a fixed Q_f of 30, we calculate two P-wave attenuation profiles and two S-wave attenuation profiles from these two data sets. The difference between the two attenuation profiles for either P- or S-wave is insignificant. This is because a constant Q_f does not have any significant effect on the variation of P- and S-wave amplitudes with depth.

5.4.3 Borehole size effects

It is well known that the variation of borehole size has an effect on the amplitude of P- or S-waves. Although our method can handle the effect of borehole size on our attenuation estimates by using a caliper log to generate synthetics, it requires making synthetics depth by depth. On the other hand, the synthetic model must be appropriate for the real case. It is very time consuming to exactly simulate the real borehole case in the presence of a tool. For convenience, we assume that the borehole size does not change with depth in the depth range of interest. In other words, we use a fixed borehole diameter of 0.2 m in our inversion procedure. The error introduced by this assumption is tested by using the caliper log shown in Figure 5.1 to calculate synthetic data. As seen from Figure 5.7, the P- and S-wave attenuation profiles calculated using equation (10) from the synthetic data with an offset of 3.2 m and input attenuation profiles are still in good agreement, even though the borehole diameter changes with depth. One might suspect the insensitivity to the diameter effect because the appearance of full waveforms changes with the borehole diameter. It is worth mentioning that our method uses the common receiver data set. The calculation for attenuation is based on the change of the averaged energy of P- and S-waves with depth. On the other hand, the change of the borehole diameters (0.22 $\sim$ 0.3 m) with depth is very small compared with the source-receiver spacing (3.2 m). The test shows that the depth-dependence of geometrical spreading is more sensitive to formation property changes than to borehole diameter changes. Another important reason is that formation intrinsic attenuation makes a major contribution to the change of P- and S-wave amplitudes with depth. With the test result, we can also understand why we can ignore the tool effect in our method, because a tool mainly makes an effective borehole size smaller. Consequently, the borehole size and tool effects can be neglected in the field data processing using our method, provided the

actual borehole size does not differ greatly from the above value. It is the insensitivity to the borehole size that allows the method to give robust estimation of attenuation.

5.4.4 A practical implementation of the new method

As described before, the modified method needs to calculate synthetic wave data, which is usually time-consuming. To solve this problem, we construct a look-up table from synthetic waveforms in advance. This table is composed of a cubic data set which is the tabulated values of $\bar{\Phi}^{syn}$ for various formation parameter values. The value of $\bar{\Phi}^{syn}$ at depth z is given by finding the $\bar{\Phi}^{syn}$ value in the table corresponding to the formation parameter values at z. We use the identity that the difference of two averages is equal to the average of differences. Therefore, in processing the data of $\Delta\Phi_i$, we can first apply an average to $\Delta\Phi_i(z,\omega)$ over frequency ω to eliminate the frequency-dependence. Equation (10) can then be expressed as

$$\bar{\Phi}_i(z) - \bar{\Phi}_i^{syn}(z) = \phi_i(z) + \overset{mean}{\omega} A_i(z,\omega) - \overset{mean}{\omega} A_i^{syn}(z,\omega). \qquad (13)$$

It can be seen from equation(13) that we only need the synthetic profile $\bar{\Phi}^{syn}(z)$ to correct for the geometrical spreading. The synthetic $\bar{\Phi}^{syn}(z)$ changes with depth only. At each depth, the value of $\bar{\Phi}^{syn}$ depends on formation parameters. It is a function of formation P- and S-wave velocities, formation to borehole fluid density ratio, borehole fluid velocity, borehole size, and source-receiver offset.

As shown from previous tests, geometrical spreading is most sensitive to the first three parameters (i.e., formation P- and S-wave velocities and formation to borehole fluid density ratio) and least sensitive to the last three parameters (i.e., borehole fluid velocity, borehole radius, and source-receiver offset). Therefore, the last three parameters are kept constant in our synthetic data. The main reason for keeping the last three parameters constant is that our method does not require that

synthetic waveform data be exactly matched with real waveform data. The useful information we need from the synthetic waveform data is the relative change of $\bar{\Phi}^{syn}$ with depth. In addition, the source-receiver offset in the acoustic tool is from 3.2 m to 4.27 m. We use a fixed offset of 3.2 m in $\bar{\Phi}^{syn}(z)$ for all cases to make an approximate modeling for offsets from 3.2 m to 4.27 m. Thus, equation (10) can be further simplified as:

$$\Delta\Phi_i(z,\omega) = \frac{2\ln X_i}{\omega} - \bar{\Phi}_1^{syn}(z), \tag{14}$$

where

$$\bar{\Phi}_1^{syn}(z) = \underset{\omega}{mean}\ \Phi_1^{syn}(z,\omega).$$

To demonstrate the validity of equation (14), we compute P-wave attenuation from synthetics with three common offsets of 3.2 m, 3.66 m and 4.27 m, respectively, as shown in Figure 5.8. Clearly, equation (14) works very well for all three cases. This means that we only need to calculate synthetics for one offset, say 3.2 m. The important implication of this example is that we can make a table of $\bar{\Phi}^{syn}$ in advance. This table consists of a three dimensional data set calculated by 34441 synthetic models with a reciprocal P-wave velocity from 150 to 550 $\mu s/m$ at an increment of 4 $\mu s/m$, a P- to S-wave velocity ratio from 1.5 to 3 at an increment of 0.05, and a formation to borehole fluid density ratio from 1.8 to 2.8 at an increment of 0.1. Each of the data in the table represents a value of $\bar{\Phi}^{syn}$. This value is calculated from a synthetic waveform corresponding to an appropriate reciprocal P-wave velocity and a P- to S-wave velocity ratio, and a formation to fluid density ratio. The final look-up table is obtained by using a cubic spline interpolation for each dimension of $\bar{\Phi}^{syn}$. It is this simplification that makes the modified method efficient for processing field data.

5.4.5 Correcting relative attenuation to absolute attenuation

In the above method, the attenuation values are solved through a reference attenuation value at some depth. In other words, they are not an absolute attenuation but the relative attenuation between depth z and the reference depth ζ. Suppose $\delta Q^{-1}(\zeta)$ is the difference between the guessed and true attenuation values at ζ, as

$$Q^{-1}_{guess}(\zeta) = Q^{-1}_{true}(\zeta) + \delta Q^{-1}(\zeta). \tag{15}$$

To determine absolute attenuation, we can estimate this error and then correct for it. According to equation (8), we can derive the estimated attenuation as follows,

$$Q^{-1}_{estm}(z) = Q^{-1}_{true}(z) + \delta Q^{-1}(\zeta)\frac{\Delta t_i(\zeta)}{\Delta t_i(z)}, \tag{16}$$

where Q^{-1} is for either P- or S-wave attenuation. Obviously, the estimated attenuation $Q^{-1}_{estm}(z)$ is independent of the source-receiver offset but it is biased from true attenuation $Q^{-1}_{true}(z)$ due to the reference attenuation error. It can be corrected by using a two receiver data set assuming that the two receiver responses are identical.

Applying the above mean and median procedures to equation (10), we have

$$\Delta\hat{\Phi}_i(z) = -Q^{-1}_{true}(z)\Delta t_i(z) + \Delta\hat{A}_i. \tag{17}$$

Here we assume that the constant term $\Delta\hat{A}_i$ of the i-th receiver is the same as that of the j-th receiver. One might consider taking a difference between $\Delta\hat{\Phi}_j$ and $\Delta\hat{\Phi}_i$, then computing Q^{-1}_{true} using,

$$Q^{-1}_{true}(z) = \frac{\Delta\hat{\Phi}_j(z) - \Delta\hat{\Phi}_i(z)}{\Delta t_i(z) - \Delta t_j(z)}. \tag{18}$$

However, it turns out that equation (18) does not work well for real data because of noise. Instead of directly calculating Q^{-1}_{true}, we estimate $\delta Q^{-1}(\zeta)$. Adding $Q^{-1}_{estm}(z)\Delta t_i(z)$ to equation (17) gives,

$$\Delta\hat{\Phi}_i(z) + Q^{-1}_{estm}(z)\Delta t_i(z) = \Delta\hat{A}_i + \delta Q^{-1}(\zeta)\Delta t_i(\zeta). \tag{19}$$

The right side of equation (19) should be constant with depth z. Taking a mean of the left side of equation (19) over depth z, we can rewrite equation (19) as,

$$\Delta_i = \Delta\hat{A}_i + \delta Q^{-1}(\zeta)\Delta t_i(\zeta), \tag{20}$$

where

$$\Delta_i = \overset{mean}{z}\left\{\Delta\hat{\Phi}_i(z) + Q^{-1}_{estm}(z)\Delta t_i(z)\right\}.$$

Using data from two offsets and assuming $\Delta\hat{A}_i = \Delta\hat{A}_j$, we can solve $\delta Q^{-1}(\zeta)$ from equation (20) because $\Delta t_i(\zeta)$ is known. Then using equation (16), we can recover true attenuation values $Q^{-1}_{true}(z)$. This scheme works much better than equation (18) because the averaging operation reduces the noise effect.

Under certain circumstances, care must be taken when making this correction. First of all, true wave amplitudes must be correctly recorded at the two offsets. Second, the two receiver responses must be matched. Finally, the estimated attenuation profiles derived from two offset data must be in good agreement.

Without correction, the error in the estimated attenuation due to inaccurate reference attenuation is less than 0.01. The effective attenuation values estimated from sonic logging data are mostly within a range of 0.005 (Q=200) to 0.1 (Q=10). Beyond this range, the attenuation values derived from sonic logging data are unreliable. Therefore, the least attenuation value Q^{-1} for some formations should be in a range of $0.005 \sim 0.02$. The probable error with the reference attenuation ($Q^{-1}_{guess} = 0.01$) is less than 0.01. In addition, from equation (16), it can be seen that errors with $Q^{-1}_{estm}(z)$ depend on both $\delta Q^{-1}(\zeta)$ and $\frac{\Delta t_i(\zeta)}{\Delta t_i(z)}$. At the least attenuation depth, Δt_i is usually smaller than those at other depths. So the errors of $Q^{-1}_{estm}(z)$ should be less than 0.01.

5.5 ATTENUATION FROM FIELD DATA

Seismic wave attenuation has been an important topic in seismic exploration and rock property evaluation. P- and S-wave attenuations have been found to be related to formation lithologies, pore fluid type, and the degree of fluid saturation (Toksoz et al., 1979; Klimentos and McCann, 1990; Klimentos, 1995). Thus, effective and reliable estimation of in-situ attenuation from full waveform logging data will be a potential tool for formation evaluation. In this section, we derive the P- and S-wave attenuation logs from full waveform logs measured in three closely spaced wells. They are referred to as wells A, S and T.

First of all, we checked the consistency in the estimates of attenuation for different receivers as this gives a measure of the repeatability and reliability for the method. The eight P-wave attenuation (Q_P^{-1}) logs shown in Figure 5.9 were independently calculated for the acoustic data sets from Well S. They are in good agreement except for some small differences. It can be observed that the attenuation log for the first receiver shows more variations and a higher quality than that for the last receiver. This is because attenuation causes the last receiver waveform to have a lower amplitude and therefore a lower signal-to-noise ratio compared to the first receiver, because of their different offsets (4.27 m vs. 3.2 m). Another important reason is that the attenuation (Q^{-1}) value we calculate is an average over the source-receiver offset. In other words, the attenuation profile from different offsets gives different depth resolution. The shorter the offset, the higher the depth resolution of the attenuation profile is. Therefore, the attenuation log from the first receiver wave data is usually used as the estimation results.

For the formation under study, we found that P-wave attenuation is closely related to the clay content and the permeability of rocks. The Gamma ray log and attenuation log (presented as $1000Q_P^{-1}$) from Well S are shown in Figure 5.10. The

two logs show a significant correlation. In a shale zone (depth range from 5028 to 5042 m, from 5210 to 5225 m), the P-wave attenuation log (Q_P^{-1}) shows a high anomaly. A laboratory study shows that the P-wave attenuation increases with a clay content in rocks (Kilmentos and McCann, 1990). In general, higher clay content correlates with lower permeability. Thus for permeable rocks, e.g., sandstones with low clay content, one should see a relatively low anomaly on the P-wave attenuation log, compared with shales.

Combining S-wave attenuation with P-wave attenuation logs can provide useful information for formation characterization. Compared to the P-wave attenuation, the S-wave attenuation log shows less variations with depth, as can be seen from Figures 5.11, 5.12 and 5.13. Core permeability values are also plotted in these figures to indicate high permeability zones of interest. Figure 5.11 shows two permeable zones between 5730-5740 m and 5685-5710 m, corresponding to high core permeability values. An interesting phenomenon is that in these two oil-producing zones the P-wave attenuation decreases and the S-wave attenuation increases relative to their respective values outside the zones. Similar phenomena can also be found from other two wells, for example, between 5005-5020 m in Figure 5.12 and between 5200-5210 m in Figure 5.13. The behavior of P- and S-wave attenuation logs at oil saturating formation intervals can be explained by the results of Klimentos (1995). He observed that S-wave attenuation equals or exceeds P-wave attenuation in oil/water-saturated sandstone rocks. Using this observation, we can infer that the zone between 5070-5130 m in Figure 5.13 is possibly an oil-bearing zone, because the two attenuation logs come together, although the zone's low-permeability values may not justify its production potential. These examples show that in-situ attenuation, combined with laboratory results, can be a useful tool for formation evaluation.

Another important application of attenuation logs for formation evaluation is to identify fractured zones in a formation. Fractures usually produce anomalies on

both P- and S-wave attenuation logs. An example is shown in Figure 5.14. The presence of multiple borehole fractures is identified using the Stoneley wave reflection analysis (Tang, 1996) results. Track 5 shows the image display of the down-going reflected Stoneley waves and the caliper curve. There are many reflection events caused by fractures. The fracture intensity is measured by the Stoneley wave reflectivity in track 4. The Gamma ray curve is also shown in the same track. Several major fractures are found between 2920-2932 m. In this interval, the P- and S-wave attenuation values are significantly higher than their respective values above and below. The high attenuation values also correlate with the waveform amplitude changes in tracks 1 and 2. This example demonstrates that attenuation logs can be a useful tool to identify borehole fractures.

5.6 DISCUSSIONS AND CONCLUSIONS

It is important to point out that our method differs from other attenuation methods (Cheng et al., 1982; Patton, 1988; Sams and Goldberg, 1990; Quan et al., 1994; Neep, 1995; Tang, 1995; Neep et. al., 1996). The differences are discussed below.

First of all, our method uses a common receiver data set and calculates attenuation over the source-receiver spacing. In other words, we extract attenuation from the information of changes of wave amplitudes with depth, while those methods extract attenuation based on the changes of wave amplitudes over two or more receivers at different distances from the source. The receiver responses in those methods must be virtually identical for the result to be valid. Our method, however, can obtain an attenuation profile regardless whether the receivers are matched or not. Secondly, we use a narrow time window length ($\sim$ 0.24 milliseconds after the first arrival) for P- and S-wave attenuation estimation. Other workers (e.g., Neep, 1995) applied a

much longer time window length ($\sim$ 1.15 milliseconds after the first arrival). It is the narrow window length that isolates the wave event (P- or S-wave) of interest from other non-attenuation related effects, such as reflection multiples generated by bed boundaries, scattering from borehole rugosity, etc. Furthermore, we avoid using spectral division, e.g., spectral ratio method, which may become unstable when there are holes (i.e., low amplitudes in the spectrum to be divided). Thus our method is more stable. Finally, and most importantly, our method separates the wave attributes that are related to formation attenuation from other effects that are related to borehole and formation elastic property changes. This separation is made by using synthetic log data, which allows the method to yield more reliable estimates of attenuation. The main shortcoming of our method is that the attenuation profile contains some errors caused by the inaccurate reference attenuation value, but these errors are usually small. In real data processing, effects such as large borehole size, borehole irregularity, off-centered tool, thin layer beds, etc. can degrade our results of attenuation estimation. Thus the result of attenuation estimates should always be used with other log data, such as borehole caliper, etc.

In conclusion, we have developed an effective and robust method for estimating P- and S-wave attenuation profiles from full waveform sonic logging data. It effectively overcomes the bias in the attenuation estimates in the original method. Using this method, the results derived from synthetic data are in good agreement with the input attenuation values. This method applies equally well to S-wave attenuation estimation in fast formations. We showed that the borehole size, borehole fluid velocity and attenuation, and wave window length have a minimal effect on our estimation method. This allows us to build an efficient look-up table to correct for the bias caused by geometrical spreading.

The results derived from three well sonic logging data sets show that the P-wave attenuation log is correlated with the clay content and permeability in sand-

stones. The greater the clay content the smaller the permeability and the greater the P-wave attenuation. In contrast, the S-wave attenuation increases with formation permeability. Formation fluid and saturation also affect attenuation. We showed that the decrease of P-wave attenuation and increase of S-wave attenuation correlate well with oil zones. This indicates that the combination of P- and S-wave attenuation logs may be potentially a useful tool in formation evaluation. We also showed that P- and S-wave attenuation values increase across borehole fractures. Thus the attenuation logs serve as a useful tool for fracture detection and characterization.

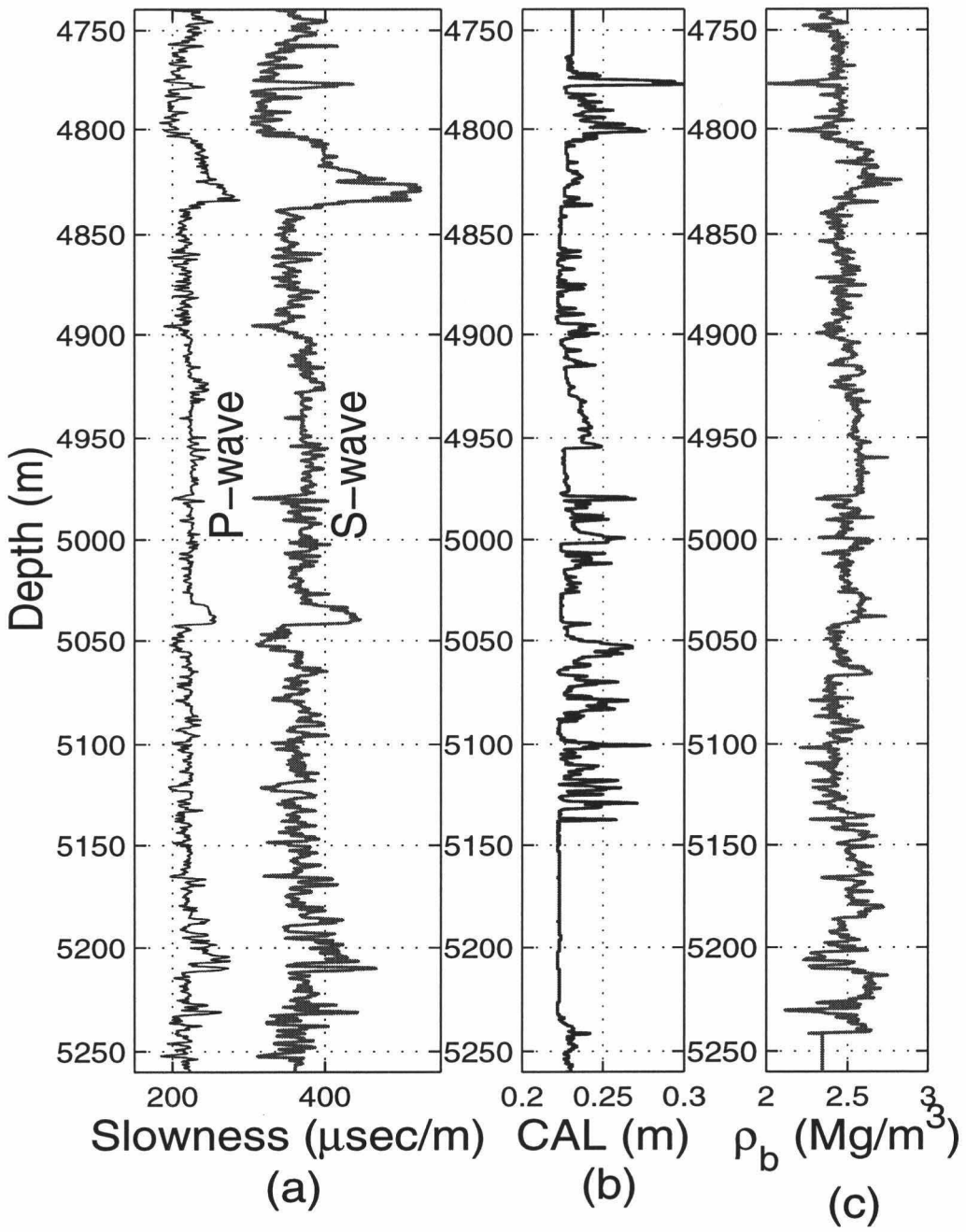

Figure 5.1: In-situ measured P- and S-wave slowness (a), caliper (b), and density (c) logs. These logs are used to compute synthetic full waveform data.

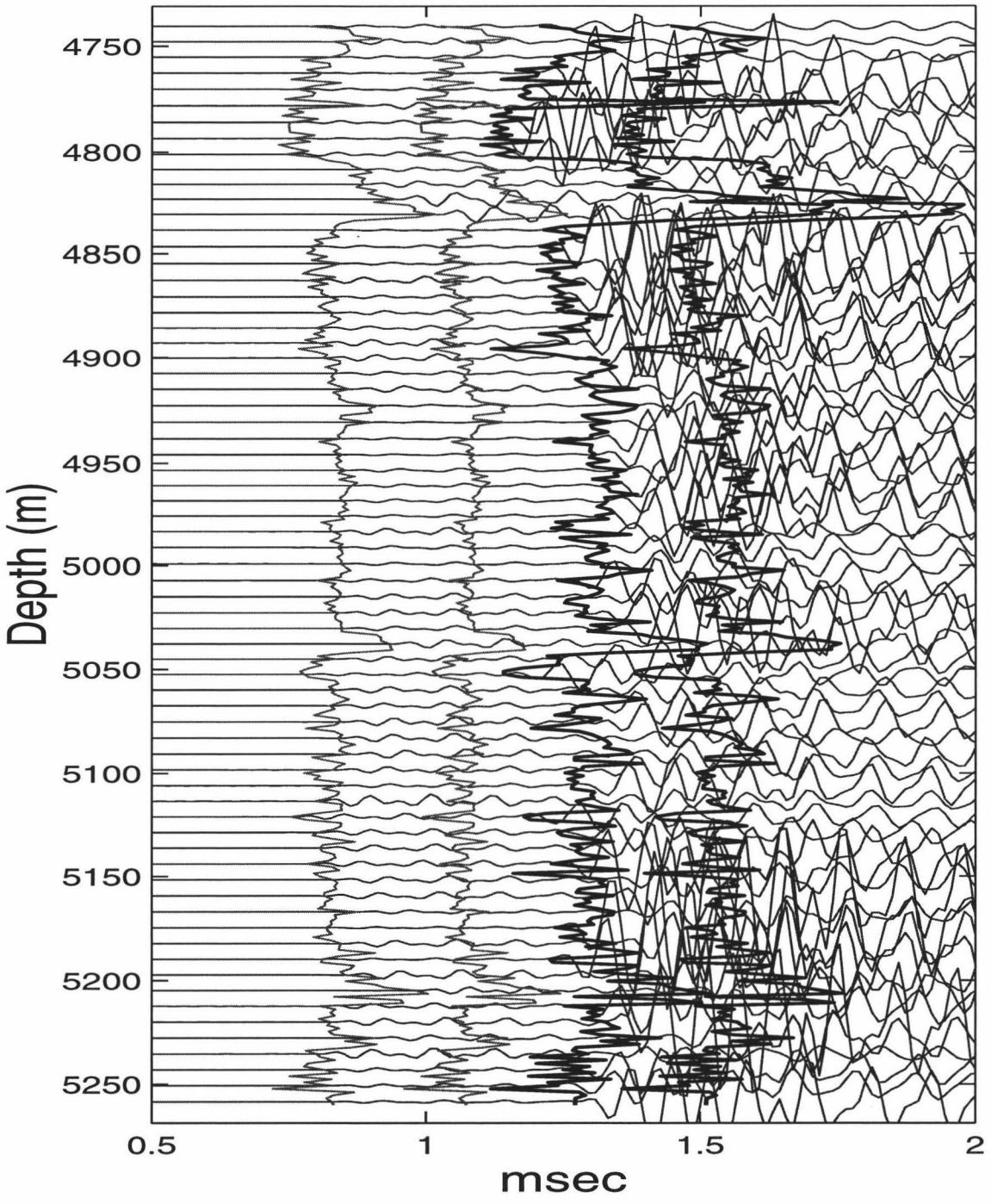

Figure 5.2: Synthetic waveforms for a receiver offset of 3.2 m. A time window of 240 μs is applied to both P- and S- head wavetrains. The waveforms were calculated at 0.1524 m depth increment, and plotted with a decimation of 50.

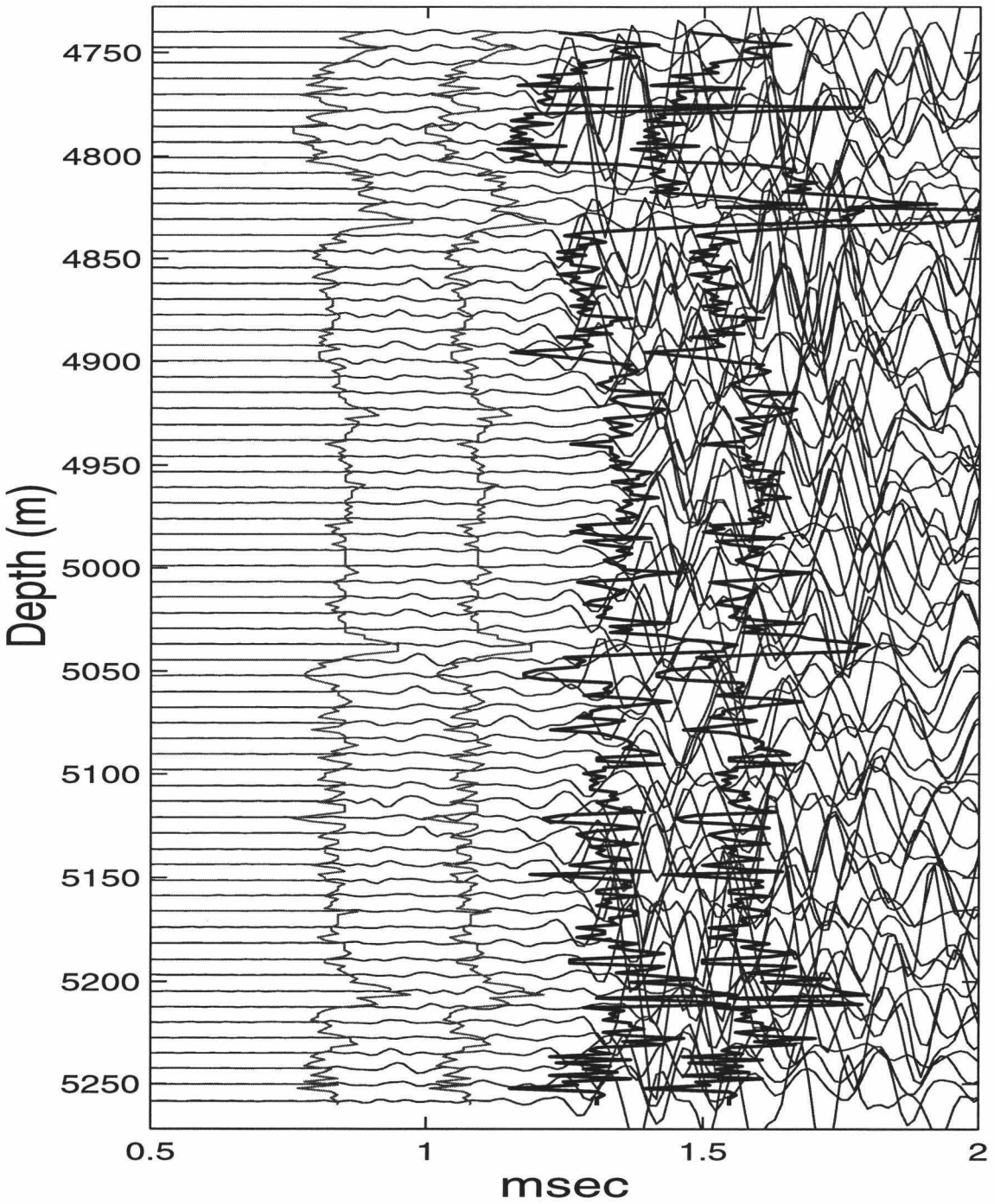

Figure 5.3: Waveforms (for receiver 1, offset 3.2 m) from in-situ measurements with a window of 240 μs for both P- and S- wavetrains. The depth decimation factor is 50 for this plot.

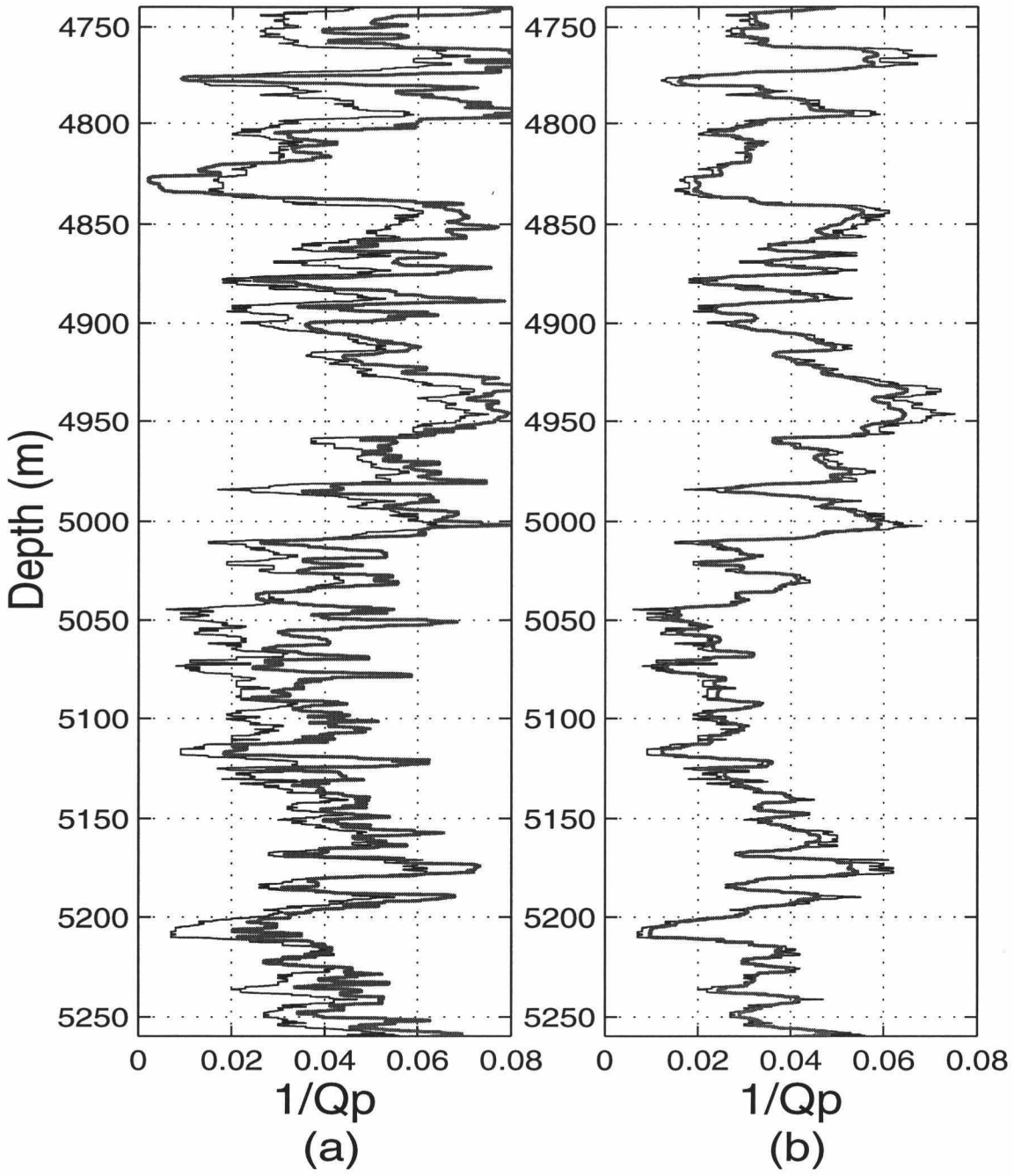

Figure 5.4: Attenuation extracted from synthetic data. Thick line - calculated attenuation Q_P^{-1}; thin line - attenuation Q_P^{-1} input into the model. (a) attenuation derived from equation (3); (b) attenuation derived from equation (10).

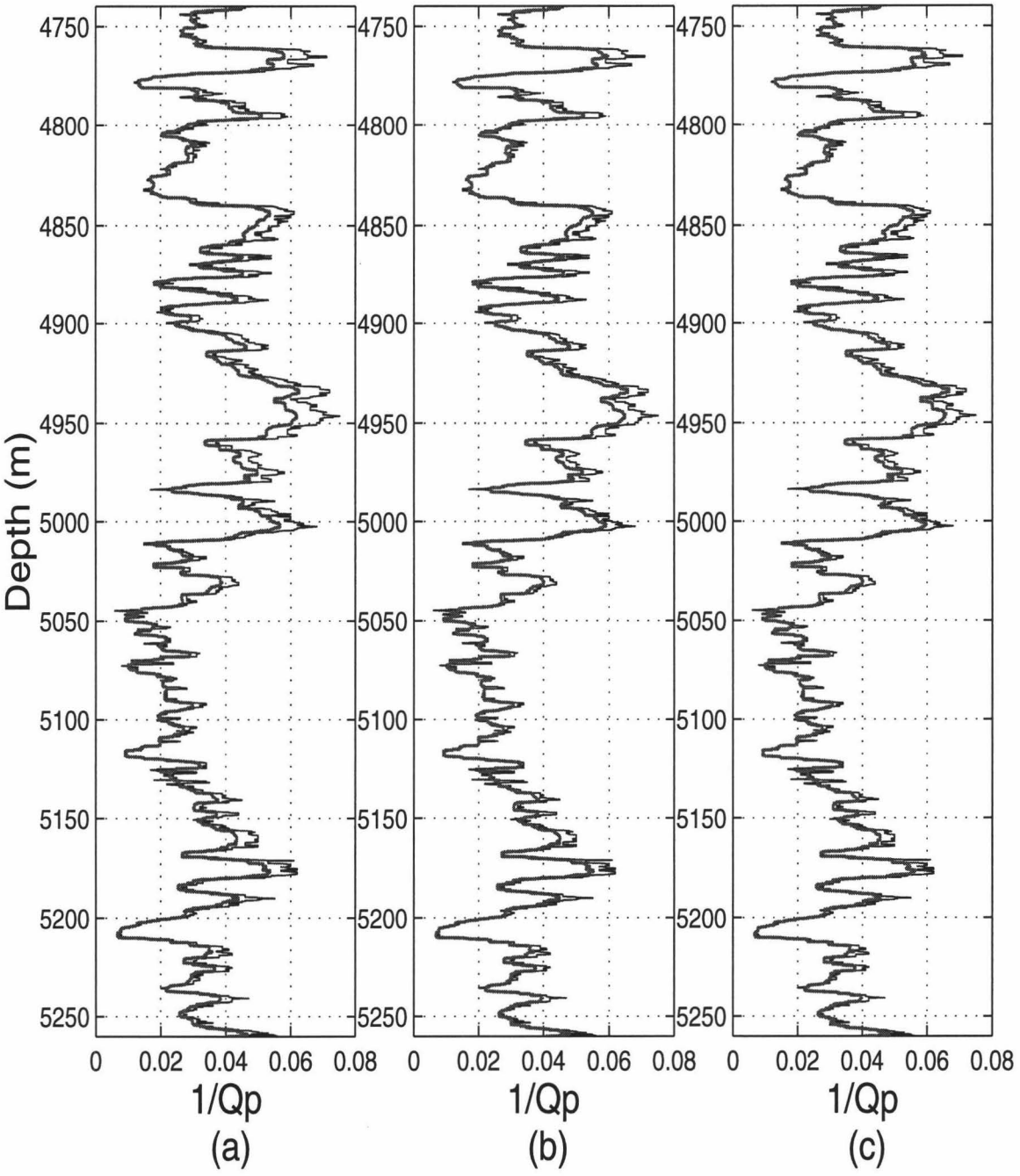

Figure 5.5: Sensitivity test of time window length for P-wave attenuation estimation. (a) window length 120 μs; (b) window length 240 μs; and (c) window length 360 μs. Thick lines - calculated attenuation; thin lines- input attenuation.

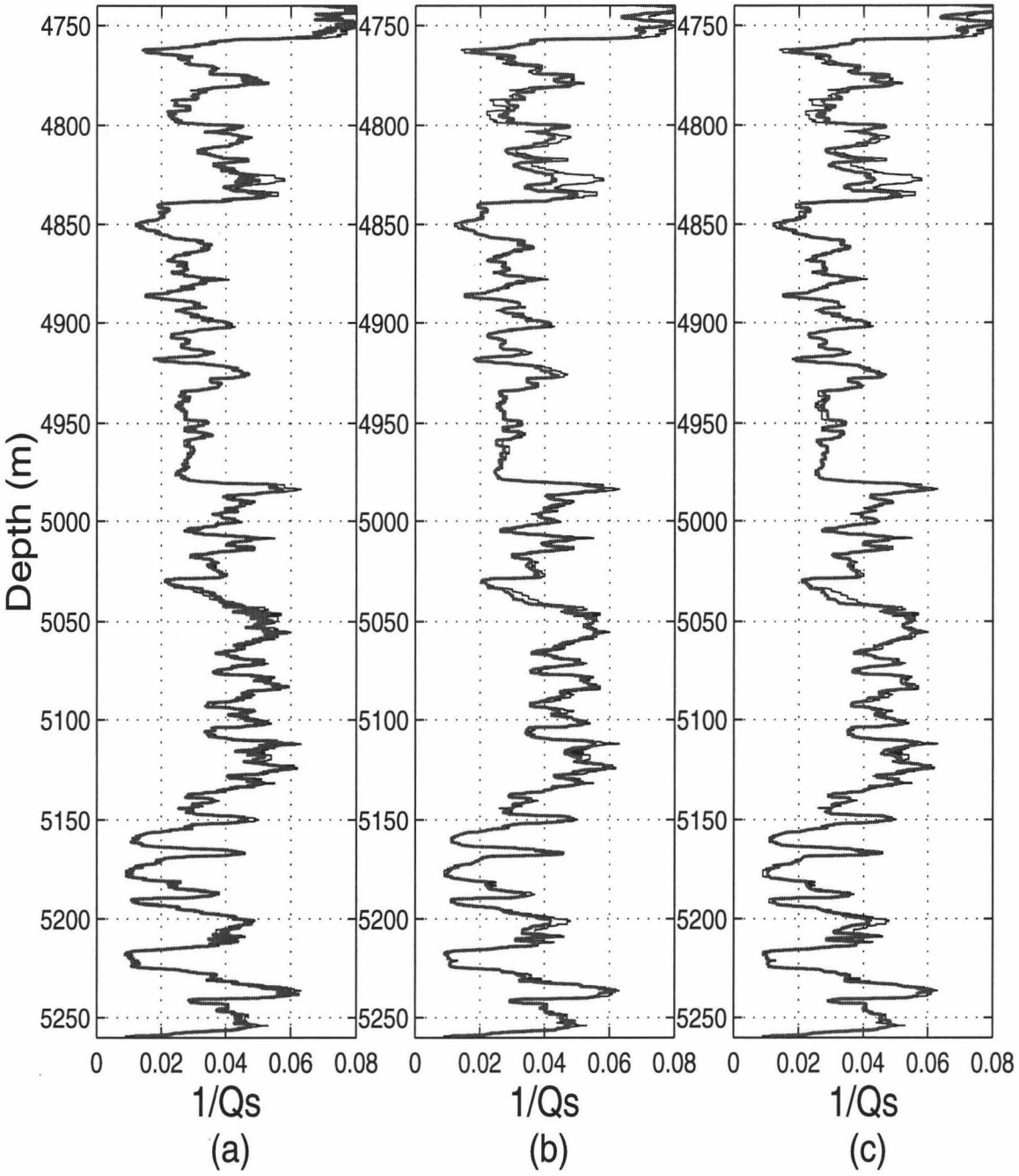

Figure 5.6: Sensitivity test of time window length for S-wave attenuation estimation. (a) window length 120 μs; (b) window length 240 μs; and (c) window length 360 μs. Thick lines - calculated attenuation; thin lines- input attenuation.

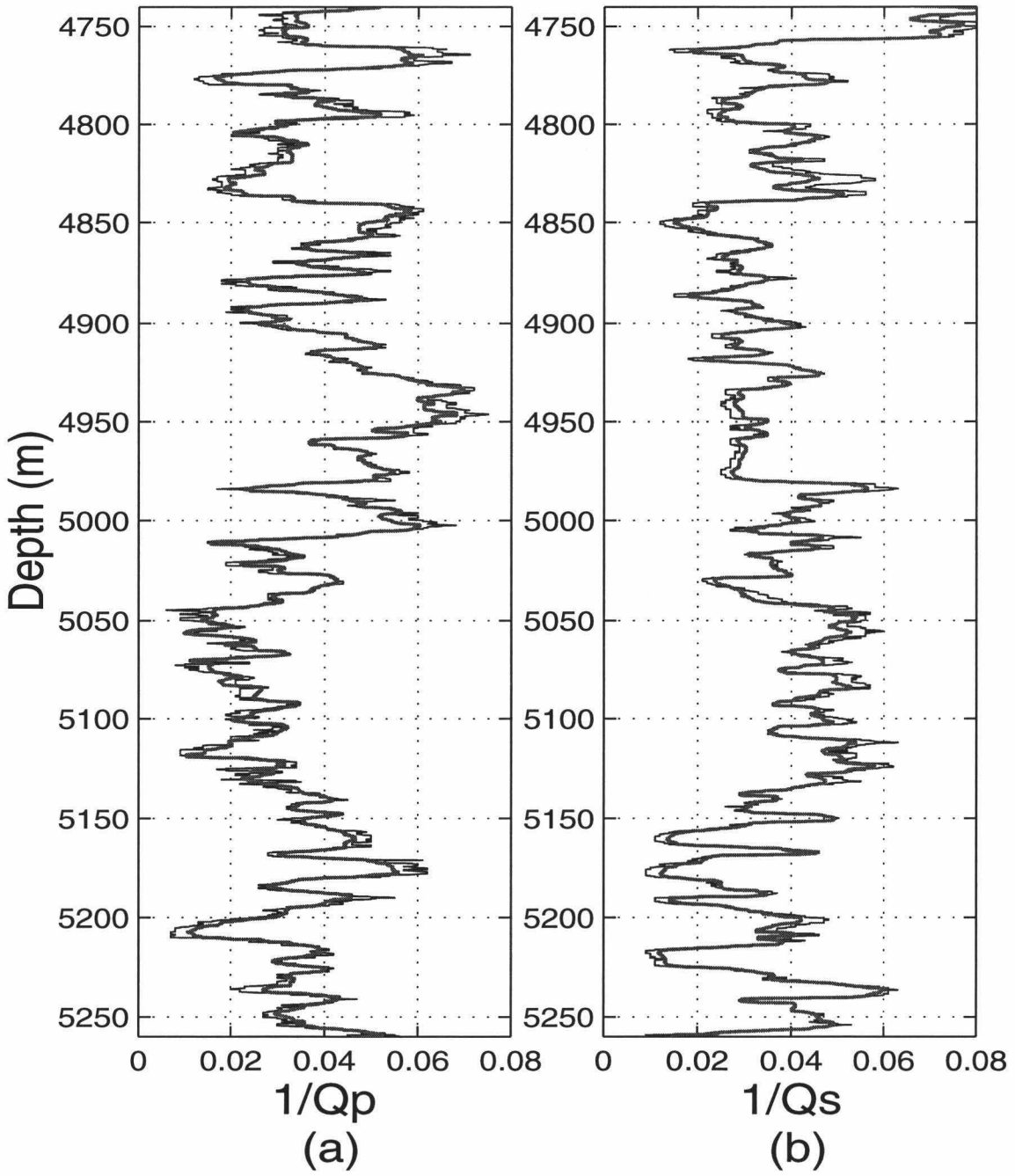

Figure 5.7: Effects of borehole size on P- and S-wave attenuation estimation. The synthetic data were made with the caliper log shown in Figure 1. (a) P-wave attenuation; (b) S-wave attenuation. Thick line - calculated Q^{-1}; thin line - input Q^{-1}. A time window length of 240 μs was applied.

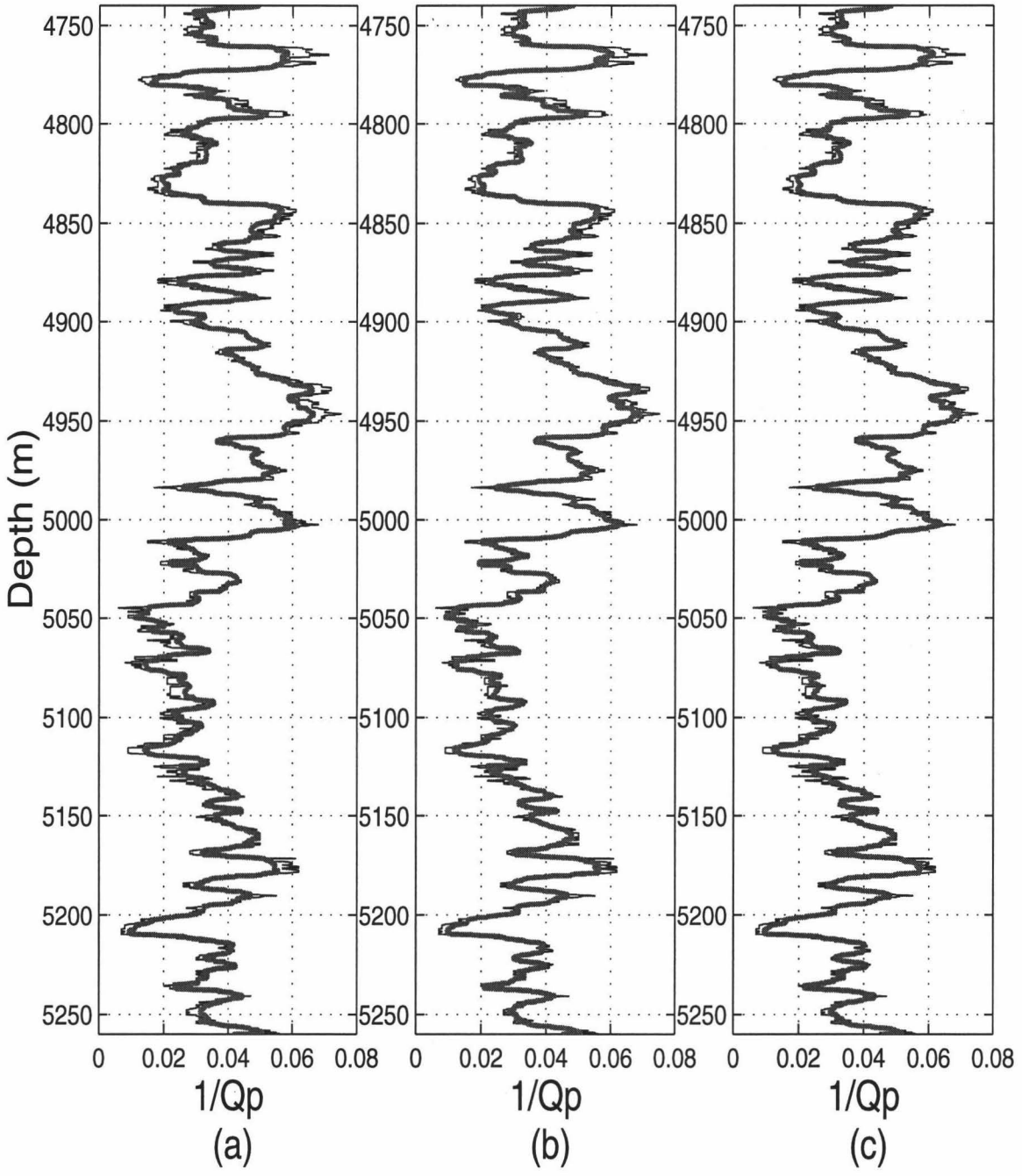

Figure 5.8: Testing effect of fixed offset (3.2 m) in the geometrical spreading correction function $\bar{\Phi}^{syn}$. Synthetic data of three offsets [3.2 m (a), 3.66 m (b), and 4.27 m (c)] are input for attenuation estimation. The results for these offsets are compared with the input values. Thick lines are calculated Q_P^{-1}; thin lines are input Q_P^{-1}.

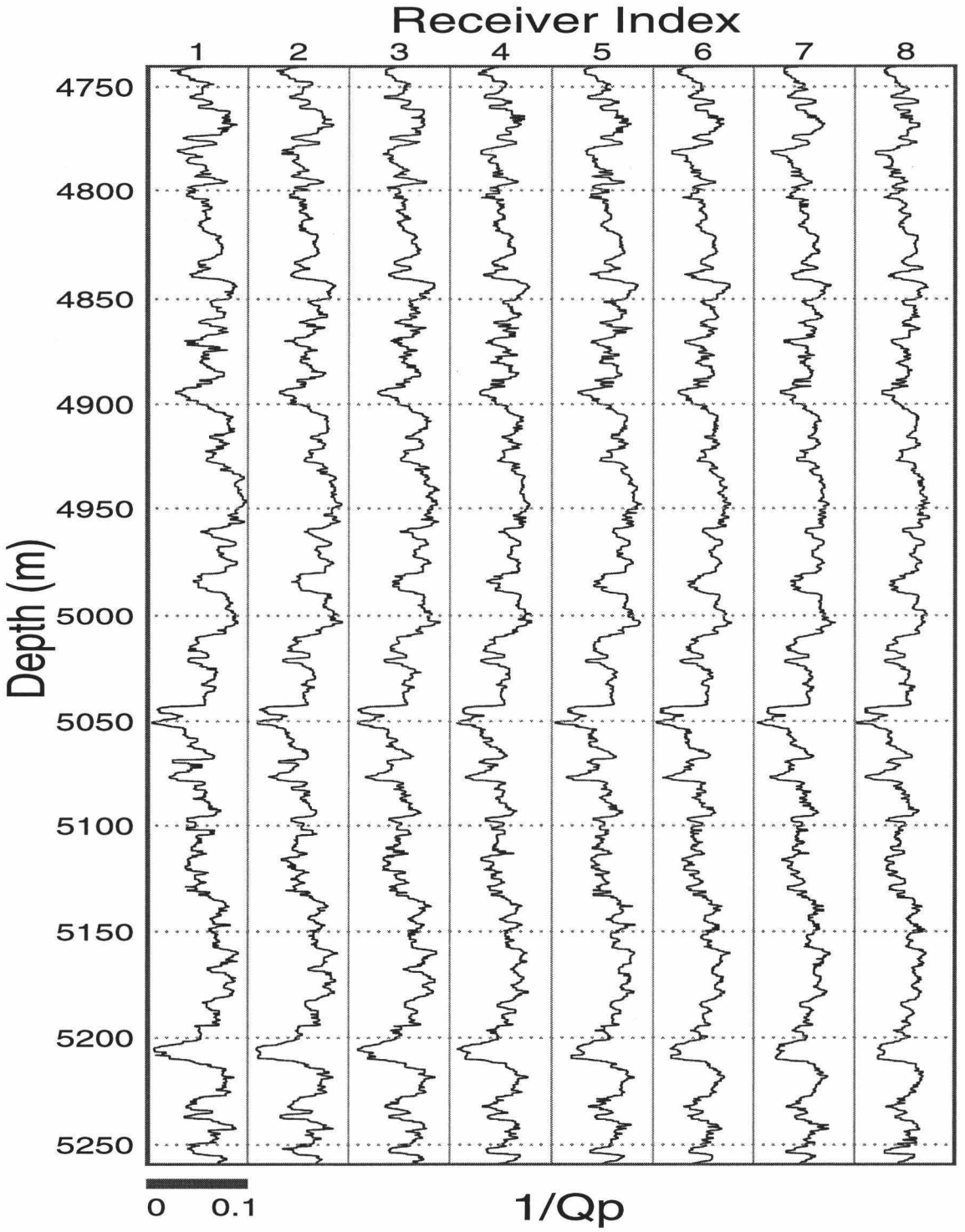

Figure 5.9: Comparison of Q_P^{-1} logs for the eight receivers in array. Each of them is independently calculated. The time window length of 240 μs was used.

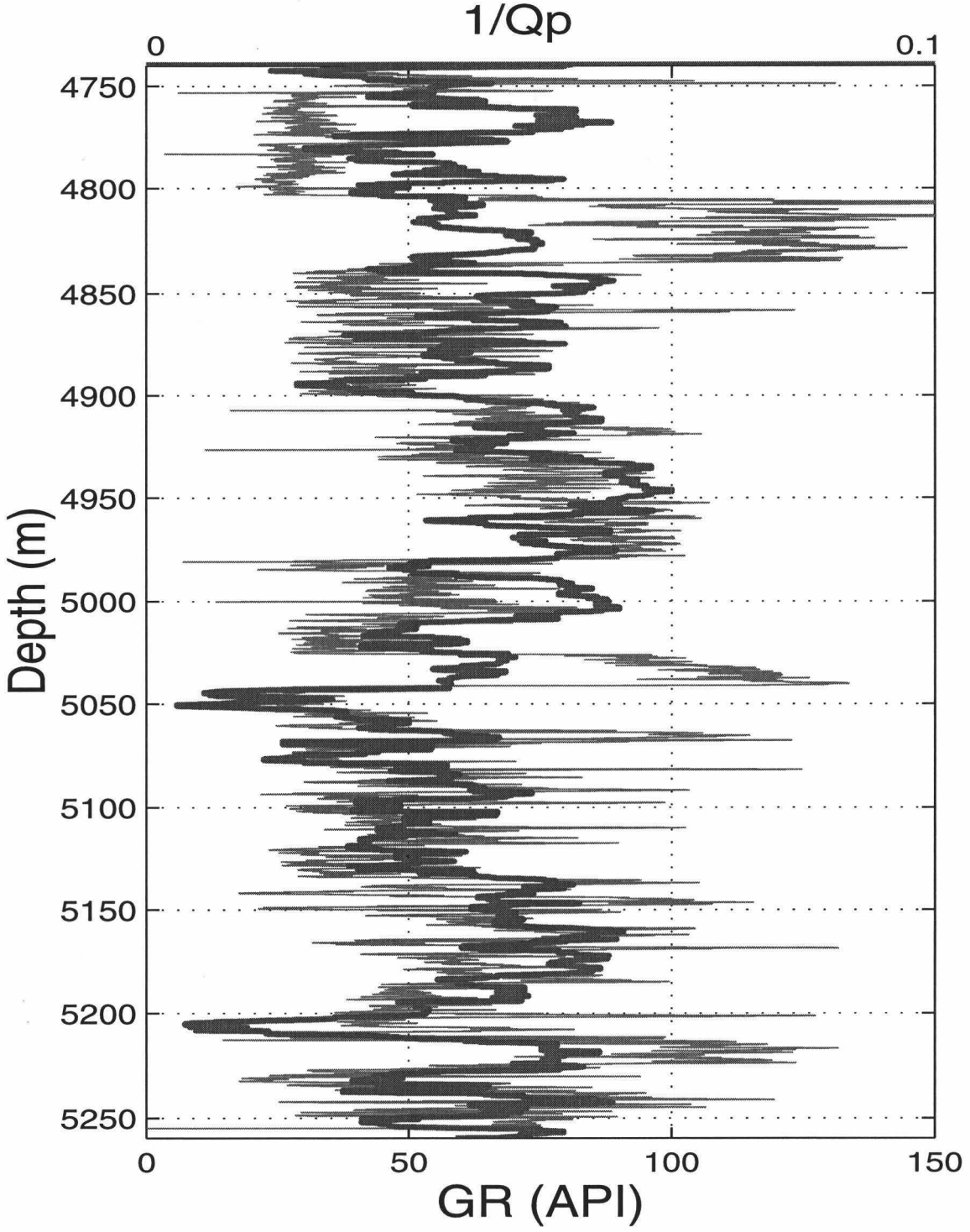

Figure 5.10: Comparison of P-wave attenuation and natural Gamma Ray logs shows certain degree of correlation between the wave attenuation and lithology.

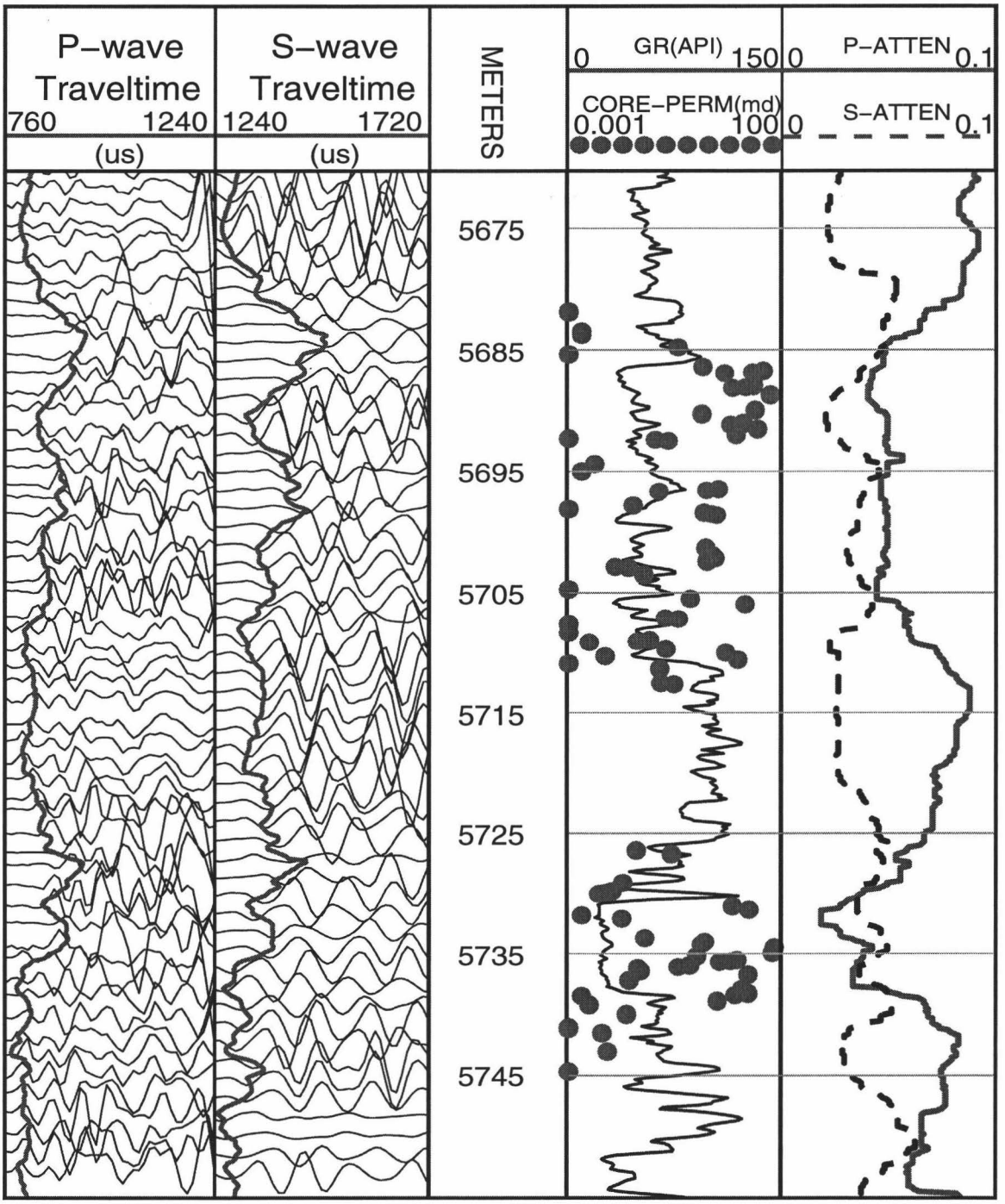

Figure 5.11: Comparison between attenuation logs and core permeabilities from Well A. On left two tracks the P- and S- head waves and their arrivals are displayed. On right two tracks the calculated P- and S-wave attenuation logs, Gamma log, and core permeability are displayed.

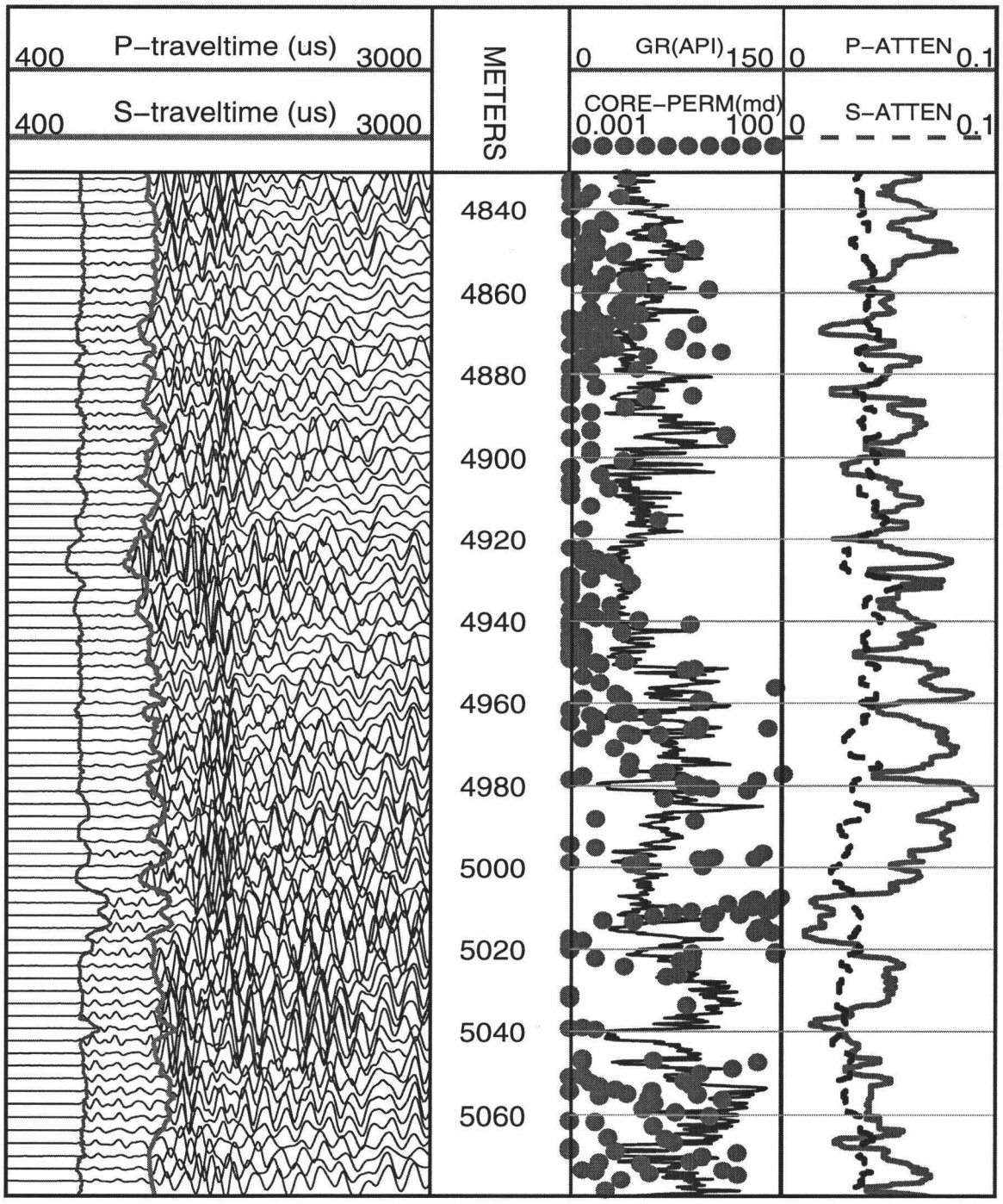

Figure 5.12: Comparison between attenuation logs and core permeability measurements for Well T. The left track displays the full waveforms and P- and S-wave arrivals. The right two tracks show the calculated P- and S-wave attenuation logs, Gamma log, and core permeabilities.

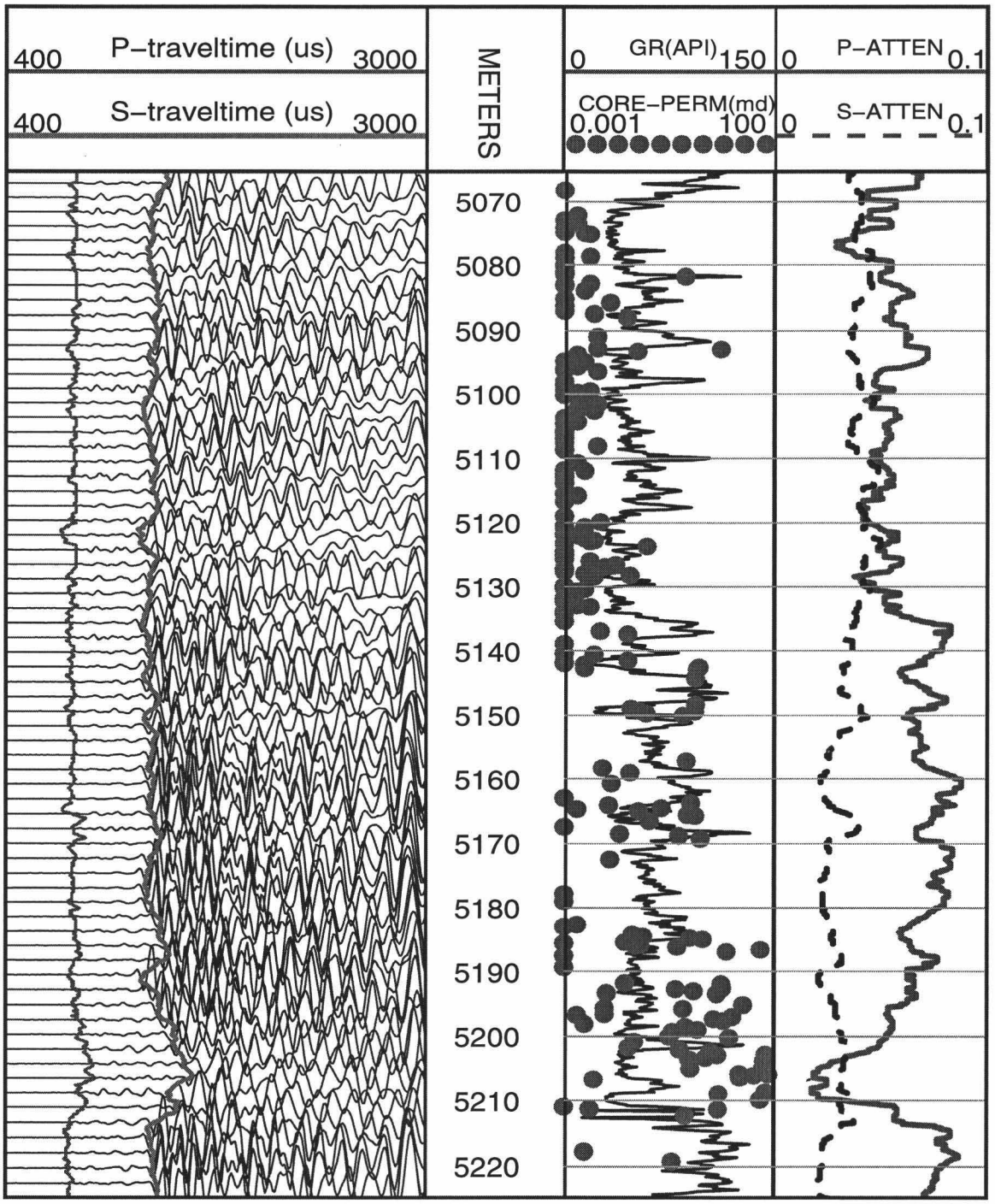

Figure 5.13: Comparison between attenuation logs and core permeability measurements for Well S. The left track displays the full waveforms and P- and S-wave arrivals. The right two tracks show the calculated P- and S-wave attenuation logs, Gamma log, and core permeabilities.

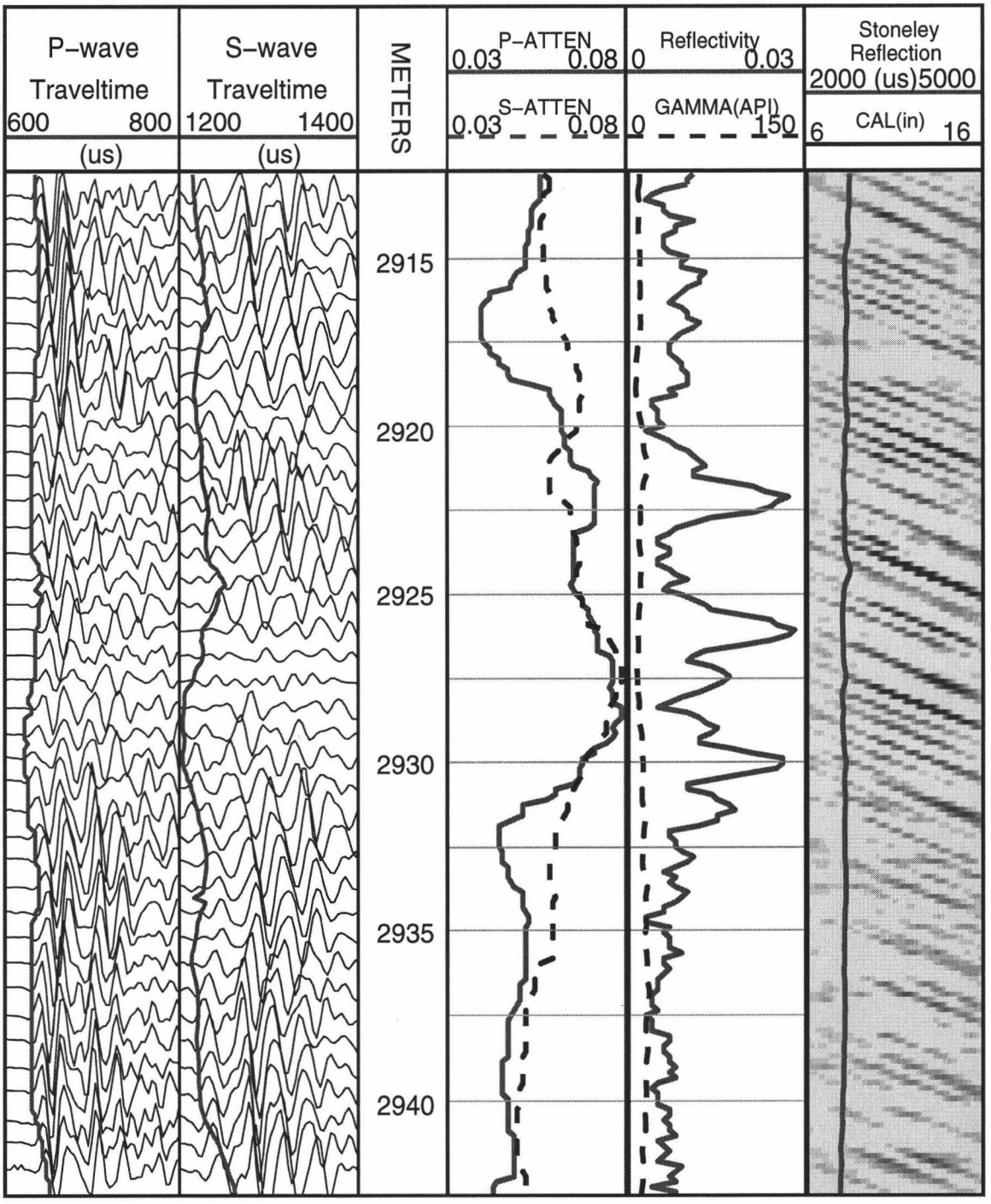

Figure 5.14: Correlation between high P- and S- wave attenuation values and the fracture location. The fractures are identified by the down-going Stoneley reflectivity values (track 5), the P- and S-wave amplitude variations can also be seen in tracks 1 and 2.

REFERENCES

Aki, K. and Richards, P. G., 1980, *Quantitative seismology theory and methods*, W. H. Freeman and Company.

Akbar, N., Dvorkin, J., and Nur A., 1993, Relating P-wave attenuation to permeability: *Geophysics*, **58**, 20-29.

Brienzo, R.K., 1992, Velocity and attenuation profiles in the Monterey deep-sea fan: *J. Acoust. Soc. Amer.*, **92**, 2109-2125.

Cheng, C.H., 1989, Full waveform inversion of P-waves for V_s and Q_P: J. Geophys. Int., **94**, 15,619-15,625.

Cheng, C. H., Toksöz, M. N., and Wills, M. E., 1982, Determination of in situ attenuation from full waveform acoustic logs: *J. Geophys. Res.*, **87**, 5477-5484.

Courtney, R.C., 1993, Calculation of acoustic parameters by a filter-correlation method: *J. Acoust. Soc. Am.*, **97**, 1145-1154.

Frazer, L. N., Sun, X. H., and Wilkens, R. H., 1997, Changes in attenuation with depth in an ocean carbonate section: ODP sites 806 and 807, Ontong Java Plateau:*J. Geophys. Res.*, **102**, 2983-2997.

Goldberg, D., Moos, D., and Anderson, R.N., 1985, Attenuation changes due to diagenesis in marine sediments, Trans. *SPWLA Ann. Logging Symp.*, **26**, pap. KK.

Hamilton, E.L., 1972. Compressional wave attenuation in marine sediments: *Geophysics*, **37**, 620-646.

Hurley, M.T., and Manghnani, M.H., 1991, Modeling compressional wave velocity and attenuation in carbonate sediments, *J. Acoust. Soc. Amer.*, **89**, 2689-2695.

Jacobson, R.S., Shor, G.G., and Dorman, L.M., 1981, Linear inversion of body wave data - part II: attenuation versus depth using spectral ratios, *Geophysics*, **46**, 152-162.

Kilmentos T., 1995, Attenuation of *P*- and *S*- waves as a method of distinguishing gas and condensate from oil and water: Geophysics, **60**, 447-458.

Klimentos T. and McCann C., 1990, Relationships among compressional wave attenuation, porosity, clay content, and permeability in sandstones: Geophysics, **55**, 998-1014.

Martin, N. W., Azavache A. and Donati M. S., 1998, Indirect oil detection by using *P*-wave attenuation analysis in eastern Venezuela Basin: Expanded Abstracts of the 68th International Meeting of the Soc. of Expl. Geophys. 914-917.

Neep, J. P., 1995, Robust estimation of *P*-wave attenuation from full waveform array sonic data: *J. Seis. Expl.*, **4**, 329-344.

Neep, J. P., Sams, M. S., Worthington, M. H., and O'Hara-Dhand, K. A., 1996, Measurement of seismic attenuation from high-resolution crosshole data: *Geophysics*, **61**, 1175-1188.

Paillet, F. and Cheng, C.H., 1991, *Acoustic Waves in Boreholes*: CRC Press, N.Y., pp. 253.

Patton, S. W., 1988, Robust and least-squares estimation of acoustic attenuation from well-log data: *Geophysics*, **53**,1225-1232.

Quan, Y, Harris, J.M., and Chen, X.F.,1994, Acoustic attenuation logging using centroid frequency shift and amplitude ratio methods: A numerical study: Expanded Abstracts of the 64th International Meeting of the Soc. of Expl. Geophys. 8-11.

Sams, M. and Goldberg, D., 1990, The validity of Q estimations from borehole data using spectral ratios: *Geophysics*, **55**, 97-101.

Shatilo, A. P., Sondergeld, C., and Rai, C. S., 1998, Ultrasonic attenuation in Glenn Pool rocks, northeastern Oklahoma: *Geophysics*, **63**, 465-478.

Sondergeld, C. H. and Rai, C. S., 1993, A new exploration tool: quantitative core characterization, *Pure Appl. Geophys.*, **141**, 249-268

Tang, X.M., 1992, A waveform inversion technique for measuring elastic wave attenuation using cylindrical bars: *Geophysics*, **57**, 854-859.

Tang, X., 1996, Fracture hydraulic conductivity estimation from borehole Stoneley wave transmission and reflection data: Trans. *SPWLA Ann. Logging Symp.*, **37**, pap. HH.

Tang X., 1995, Waveform inversion of seismic P-wave attenuation from borehole compressional wave logs: Expanded Abstracts of the 65th International Meeting of the Soc. of Expl. Geophys. 476-479.

Toksöz, M.N., Johnston, G.H., and Timur, A., 1979, Attenuation of seismic waves in dry and saturated rocks, 1. Laboratory measurements: *Geophysics*, **44**, 681-690.

Tonn, R., 1991, The determination of the seismic quality factor Q from VSP data: a comparison of different computational methods: *Geophysical Prospecting*, **39**, 1-27.

Tsang, L. and Rader, D., 1979, Numerical evaluation of transient acoustic waveforms due to a point source in a fluid-filled borehole: *Geophysics*, **44**, 1706-1720.

Chapter 6
Shear wave attenuation profile from sonic dipole well-log data

6.1 ABSTRACT

A shear wave attenuation profile is extracted from dipole waveform well-log data. The method is demonstrated by applying it to synthetic data, and then to monopole and dipole field data for a hard formation. The attenuation profiles for the two types of field data agree remarkably well.

6.2 INTRODUCTION

Attenuation, as an independent parameter in the acoustic rock properties, is potentially rich in information, such as lithology, physical state, and degree of saturation of rocks. S-wave attenuation has been more difficult to obtain from acoustic logging data than P-wave attenuation has. For a slow formation (formation shear sound speed less than fluid sound speed) the shear head wave is not present, and even in a fast formation the shear head wave is contaminated by the compressional coda. In consequence of these problems, few publications consider the extraction of shear attenuation from well-log data. Cheng et al. (1982) used a variational method to extract S-wave attenuation from pseudo-Rayleigh waves recorded with a monopole tool. For P-wave attenuation, Cheng et al. (1984) introduced a spectral peak method that is more robust than spectral ratios for narrow band data, and Klimentos (1995) applied their spectral peak method to extract shear attenuation from monopole data in a hard formation.

Dipole well logging is a means to obtain S-wave attenuation because dipole sources excite the flexural mode. The mode is dispersive, but in its low frequency limit it travels with formation shear velocity and attenuation (Kurkjian, 1986; Kurkjian and Chang, 1986; Schmitt et al., 1988). For practical purposes, the frequency can be considered sufficiently low if the shear wavelength in the formation is less than the source-receiver offset, but much longer than the diameter of the hole (Kurkjian, 1986).

The commercial dipole logging tools MAC and XMAC use the band of 2–4 kHz, in which, as will be shown below, the dispersion has negligible effect on the attenuation estimate.

Usually, it is difficult to determine in-situ attenuation from well log data because many factors, such as source and receiver transfer functions, including coupling to the borehole wall, affect the way amplitude diminishes with distance. To deal with this difficulty, Frazer et al. (1997) used a single source-receiver data set to calculate a relative attenuation profile simply by taking the logarithm of the signal and averaging over frequency at each depth. Their method was applied to sonic monopole well-log data for relative compressional attenuation in a slow formation of marine sediments.

More recently, Sun et al. (in press) improved the method of relative attenuation by using synthetic seismograms to correct the data for the variation of formation velocity and density. The improved method was applied to monopole data for compressional and shear attenuation. Here the new method is applied to dipole data, and monopole data from the same well are used as a check on the method.

6.3 METHOD

The amplitude at frequency ω of the flexural wave from a source at $z + \frac{1}{2}\Delta z$

to a receiver at $z - \frac{1}{2}\Delta z$ is represented as

$$X(\omega, z, \Delta z) = B(\omega)E(\omega, z, \Delta z)\exp[-\alpha\Delta z], \tag{1}$$

in which $B(\omega)$ is the product of the source and receiver amplitude spectra, while the term E contains all other wave-theoretical effects on amplitude including fluid to formation coupling factors, which may be frequency dependent. The attenuation coefficient is $\alpha = \frac{\omega}{2Q_S v_s}$, where v_s is formation shear velocity and Q_S is the usual dimensionless shear wave quality factor for the interval Δz.

Taking a logarithm of equation (1), and dividing it by $\frac{\omega}{2}$, gives

$$\frac{2\ln X}{\omega} = -Q_S^{-1}v_s^{-1}\Delta z + \frac{2\ln(BE)}{\omega} \tag{2}$$

The next step is to make synthetic dipole waveforms for each depth using the known P- and S-wave velocity, density, and caliper logs obtained from well-log measurements; these synthetics are made with zero attenuation of formation. Then, we combine the data and synthetics by subtraction

$$\Phi(z, \omega) = \frac{2\ln(X)}{\omega} - \frac{2\ln(X_{syn})}{\omega}. \tag{3}$$

This subtraction largely removes amplitude effects related to variations of formation density and velocities as well as borehole size. Φ can be written as

$$\Phi(z, \omega) = \phi(z) + A(z, \omega), \tag{4}$$

where $\phi(z) = -Q_S^{-1}v_s^{-1}\Delta z$, and $A(z, \omega) = \frac{2\ln(BE)}{\omega} - \frac{2\ln(B_{syn}E_{syn})}{\omega}$. Note that the term A is theoretically independent of z if fluid to formation coupling factors are independent of z.

To extract the attenuation profile, we use the mean-median procedure given in Frazer et al. (1997). We first average over frequency to get a mean profile for Φ in the form,

$$\bar{\Phi}(z) = \overset{mean}{\omega}\ \Phi(z, \omega). \tag{5}$$

We then take a median over depth z to get the average shift of each Φ profile from the mean:

$$\Delta\tilde{\Phi}(\omega) = \underset{z}{median} \left\{ \Phi(z,\omega) - \bar{\Phi}(z) \right\}. \tag{6}$$

Finally we take a median in frequency of the shifted Φ profiles:

$$\hat{\Phi}(z) = \underset{\omega}{median} \left\{ \Phi(z,\omega) - \Delta\tilde{\Phi}(\omega) \right\}. \tag{7}$$

The result, $\hat{\Phi}(z)$, is an estimate of $-Q_S^{-1}(z)v_s^{-1}\Delta z$ plus an unknown constant $\hat{A}$. Finally, using an assumed value of attenuation at some depth ζ, we extract $Q_S^{-1}(z)$ from $\hat{\Phi}(z)$ in the form

$$Q_S^{-1}(z) = \frac{\hat{\Phi}(z) - \hat{\Phi}(\zeta) + Q_S^{-1}(\zeta)v_s^{-1}(\zeta)\Delta z}{v_s^{-1}(z)\Delta z}. \tag{8}$$

The profile $Q_S^{-1}(z)$ is referred to as a relative attenuation profile (Frazer et al., 1997), because the assumed value $Q_S(\zeta)$ may be inaccurate. The error of the relative attenuation profile caused by the inaccurate reference value of attenuation can be corrected by using a multiple receiver data set. For the i-th source-receiver pair, $\hat{\Phi}$ can be written as

$$\hat{\Phi}_i(z) = -Q_S^{-1}(z)v_s^{-1}(z)\Delta z_i + \hat{A}_i. \tag{9}$$

If all receivers in the tool have the same transfer function, the term $\hat{A}_i$ is less variable with different receivers. Averaging $\hat{\Phi}_i(z)$ over z, we can estimate the mean value of $Q_S^{-1}v_s^{-1}$ by using a linear fitting procedure. Using this mean value, we can convert the relative attenuation profile to absolute attenuation. One might use a linear fit on equation (9) depth by depth to obtain $Q_S^{-1}(z)v_S^{-1}(z)$. The results of the $Q_S^{-1}(z)v_S^{-1}(z)$ are not stable.

6.4 SYNTHETIC TESTS

Our physical model is an axisymmetric fluid-filled borehole, extending to infinity in the z direction, embedded in an isotropic solid formation. The dipole source

is physically similar to two monopole sources of opposite sign located adjacent to each other in the same horizontal plane. Our Green's function is computed by the frequency-wavenumber integration method of Kurkjian and Chang (1986), with various enhancements such as causal attenuation, complex frequencies (Mallick and Frazer, 1987), and Filon integration (Frazer, 1988). Attenuation is introduced through a complex velocity given by (e.g. Aki and Richards, 1982)

$$v_x(\omega) = v_x(\omega_0)[1 + \frac{1}{\pi Q_x} \ln(\frac{\omega}{\omega_0})](1 + \frac{i}{2Q_x})^{-1}, \tag{10}$$

where v is velocity, Q is quality factor, (index $x = p, s$, or f for formation P-wave, S-wave, or borehole fluid, respectively), and ω_0 is a reference frequency at the center of the band of interest.

Synthetics were compared with published examples from Schmitt (1988). In Figure 1, synthetic dipole waveforms for a Ricker source wavelet with a central frequency of 6 kHz are shown. As in Schmitt's example of a fast formation (1988, Fig. 3), the parameters used in the synthetics are $v_p = 4878$ m/s, $v_s = 2601$ m/s, $v_f = 1500$ m/s, $Q_P = 60$, $Q_S = 60$, $Q_f = 30$, formation density $\rho_b = 2.16$ Mg/m^3, borehole fluid density $\rho_f = 1$ Mg/m^3, and borehole radius $R = 0.10$ m. The first arrival is seen to travel with the formation shear velocity. Figure 2 compares synthetic data with an actual waveform from the data set considered below. A central frequency of 3 kHz for the synthetic source-receiver wavelet was used to closely match the real data.

To test the inversion procedure, synthetic data were generated using the measured P- and S-wave velocity logs (Fig. 3a). The synthetic waveform data were generated with a depth increment of 5 ft, ten times as large as that in the field data. As the density and caliper logs were not available for this site, we used a fixed formation density of 2.4 Mg/m^3 and a fixed borehole radius (0.10 m). The borehole fluid quality factor was fixed at 30. The P- and S- attenuations were chosen to be similar in part of the section and opposite in another part of the section to test for the effect

of P-wave attenuation on the S-wave attenuation estimate(Fig. 3b).

To compute the necessary spectral estimates of the data, we used whole waveforms and added zeros to obtain 512 time points. Figure 4 shows the results of inversion at source-receiver offsets corresponding to receivers #1 and #8 in the field data. It can be seen from the figure that the inverted attenuations are in good agreement with the input values except for a slight over-estimate of attenuation at depths with high attenuation. The varying P-wave attenuation does not affect our S-wave attenuation estimates.

The results inverted from synthetics in the frequency bands 2-3 kHz, 2-4 kHz, ..., 2-7 kHz, as shown in Figure 5, are in good agreement with the model values of attenuation. For larger borehole radii up to 0.15 m, the inversion still works very well in the frequency band 2-4 kHz though not as well for the other wider bands. Not coincidentally, the XMAC tool uses a frequency band of 2 to 4 kHz because that band is also optimal for the measurement of S-velocity.

6.5 TEST WITH FIELD DATA

In fast formations, both monopole and dipole waveform log data are sensitive to S-wave attenuation. We have both kinds of data for the same hole. The dipole field data from receiver # 1 are shown in Figure 6, and it can be seen that there is considerable variation of amplitude with depth. This variation is due to variations in formation velocity, density, and attenuation. The synthetic dipole waveforms computed for zero attenuation are also shown in Figure 7, for the 9.5 ft offset. The S-wave attenuation profiles inverted independently for the eight receivers are displayed in Figure 8, where it can be seen that the agreement between receivers is excellent.

To compare with our results from the field dipole data, we applied a similar procedure to the monopole data from the same hole (not shown). The 20 sample

points (i.e., 0.24 ms) after the S-wave first arrival were used for our attenuation estimation. Unlike the dipole tool, the receivers in the monopole tool were well calibrated in the frequency band of 5 to 20 kHz. We first extracted a relative S-wave attenuation profile from receiver # 1. Then we corrected it to absolute attenuation by using the mean value of $Q_S^{-1}v_s^{-1}$ over all eight receivers, shown in Figure 9.

A comparison of the attenuation profiles from both monopole and dipole waveform log data is shown in Figure 10. Although agreement is not perfect, the monopole and dipole results track each other fairly well throughout the section. Not surprisingly, the agreement is poorest in the shallowest part of the section (9950 to 10150 ft) where S-wave velocity is so low that the formation is near to being soft. Even here the two types of data agree on major features, such as the zone of high attenuation between 9950 ft and 10140 ft. Below depth 10700 ft (right panel) the formation is harder and agreement is better even in the details.

It is not surprising that results for the two data types do not quite agree because the data were generated by different sources(monopole and dipole) in different frequency bands (5–20 kHz and 2–4 kHz). The use of a fixed borehole diameter and a fixed value of formation density in our inversions is also a source of error. We expect that the dipole S-wave attenuation profile is more accurate than that for the monopole data. As noted above, the S-head waves on the monopole waveforms are contaminated by P-head wave coda, and so their first arrivals are often difficult to determine.

6.6 CONCLUSIONS

The results above indicate that good S-wave attenuation profiles can be extracted from dipole waveform log data. In particular, synthetic tests showed that in the band 2–4 kHz dispersion of the flexural modes has an insignificant impact on our attenuation estimation for borehole radii between 0.1 and 0.15 m. As expected,

comparison of dipole results with monopole results showed good agreement except where the formation is close to being slow.

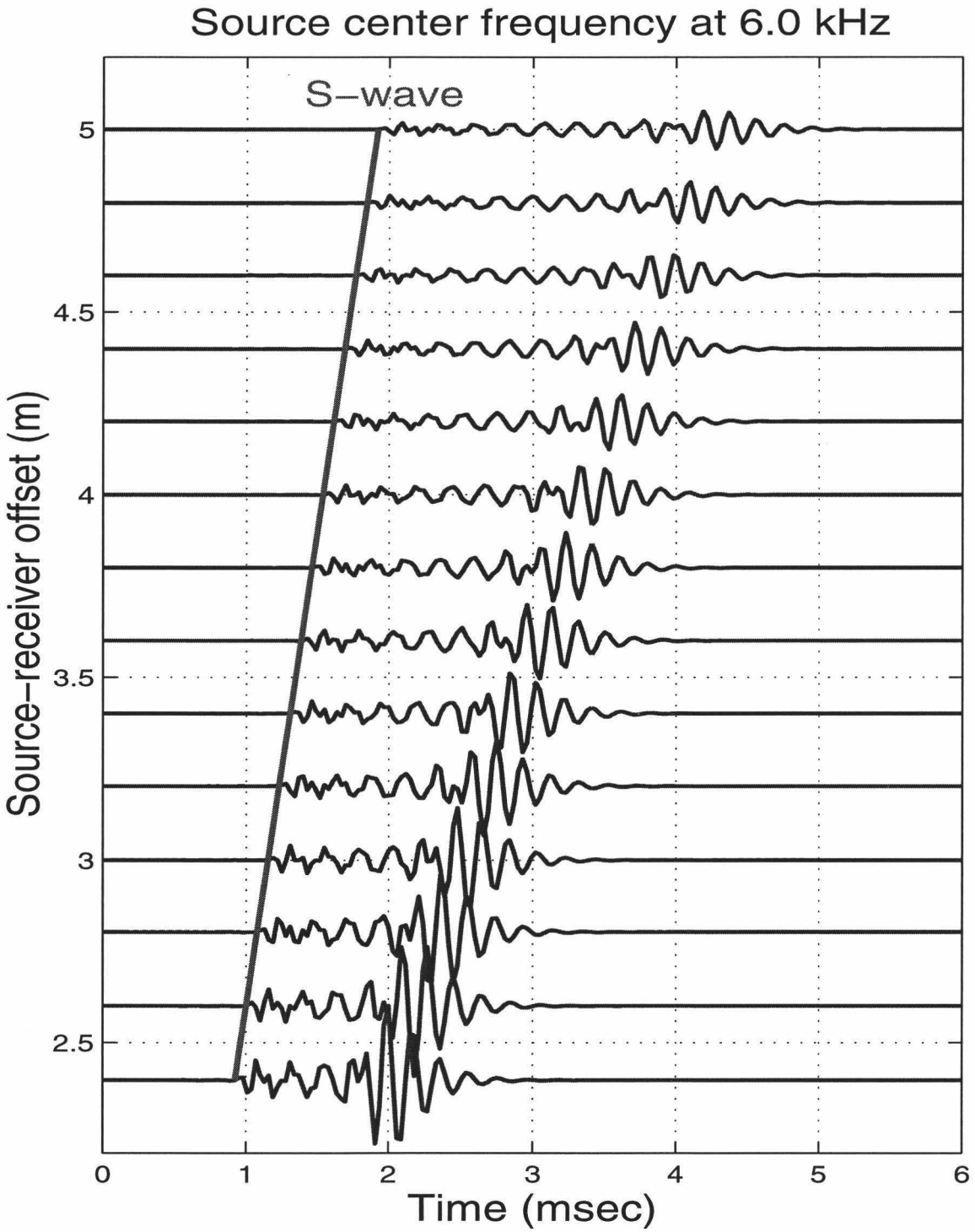

Figure 6.1: Synthetic dipole waveforms in the band 0–16 kHz using a Ricker source with a central frequency of 6 kHz.

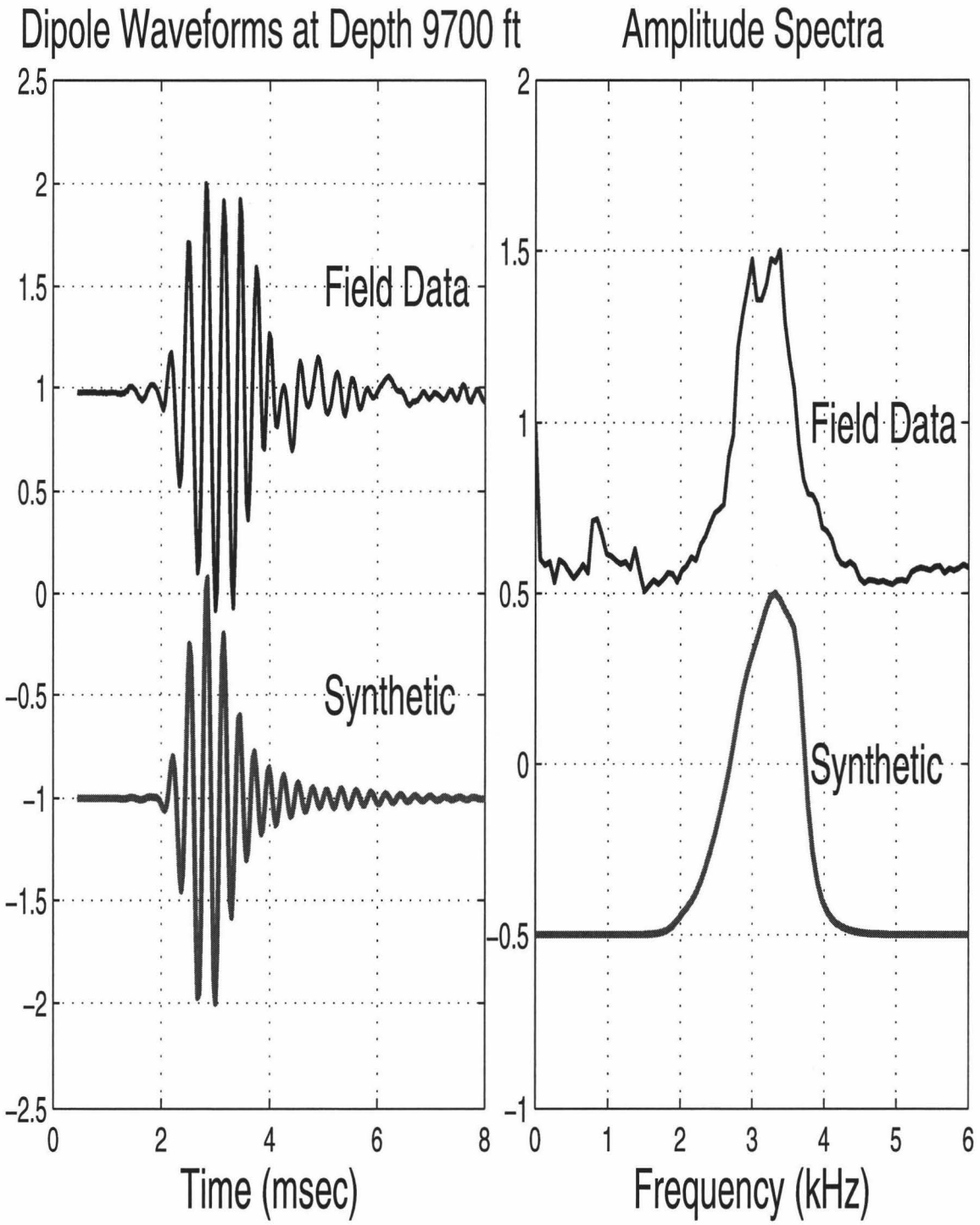

Figure 6.2: A comparison of synthetic dipole waveform and its spectrum with field data at depth 9700 ft.

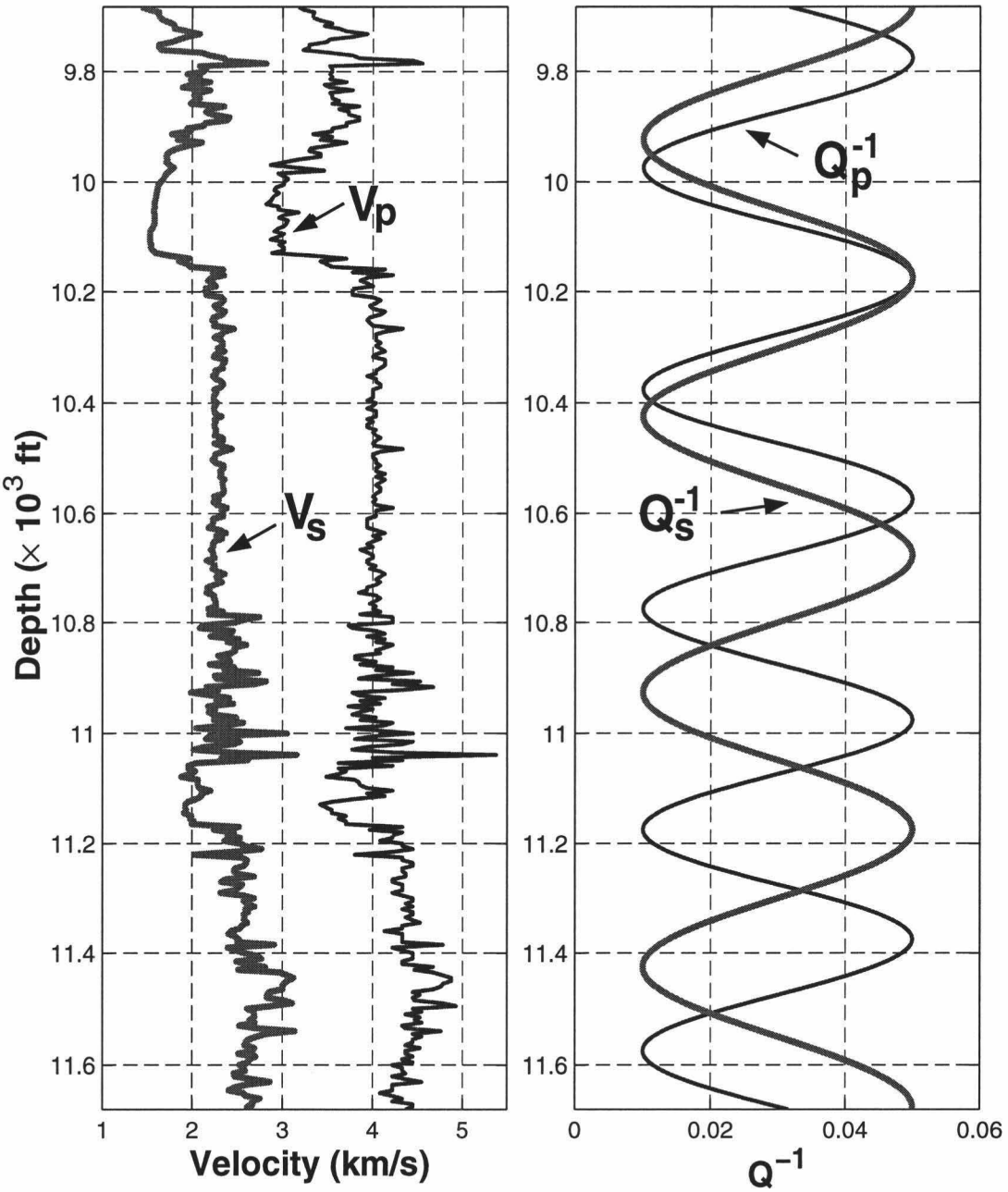

Figure 6.3: Parameters of P- and S-wave velocities (left panel) and attenuations (right panel) used in synthetic tests. The velocities are from well logging data. The attenuation curves were chosen to reveal possible trade-offs between P- and S-attenuation.

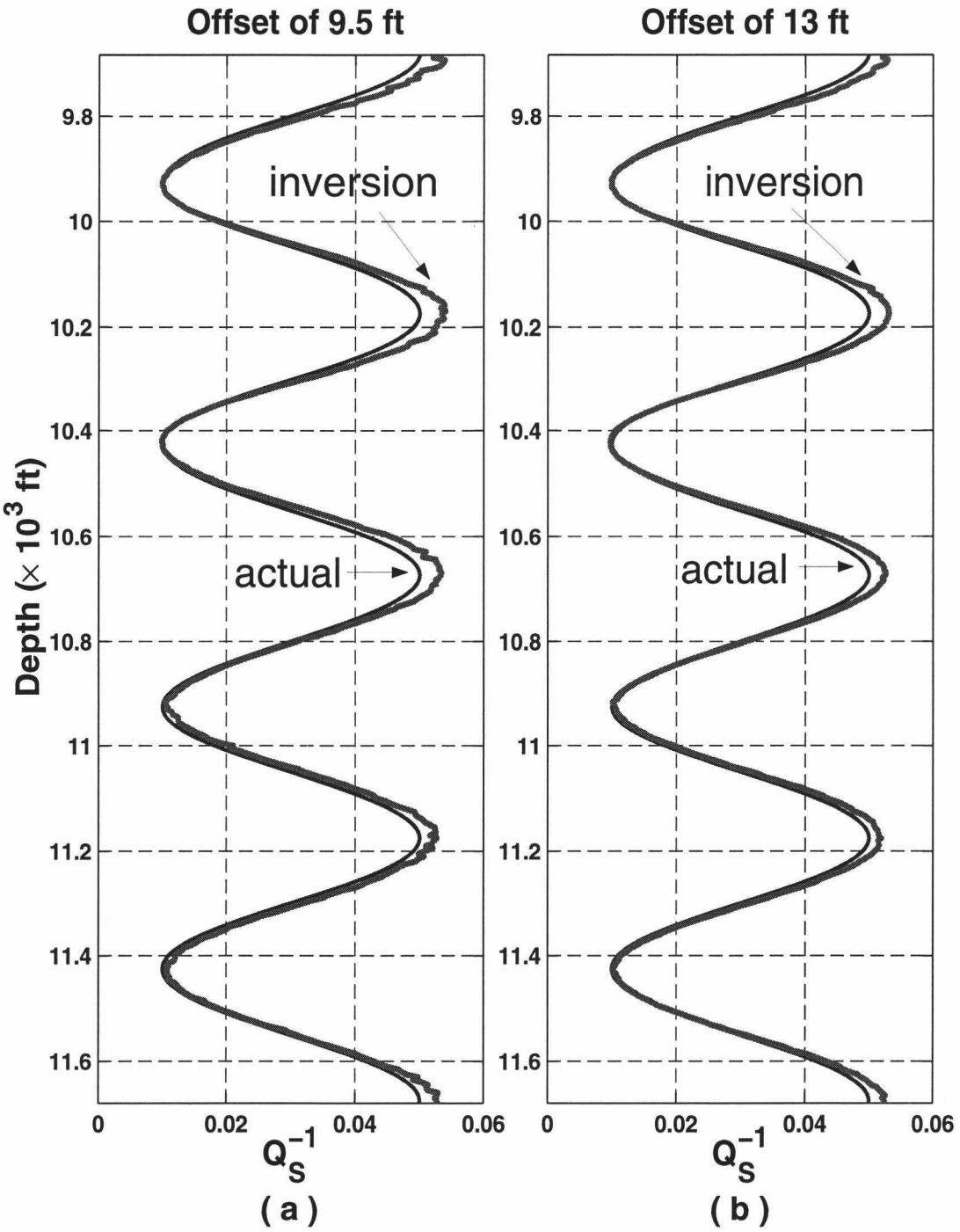

Figure 6.4: S-wave attenuation profiles (thick lines) derived from the synthetic dipole waveform data with a source-receiver offset of 9.5 ft (a) and 13 ft (b), corresponding to field data sets from receivers # 1 and # 8 in an eight receiver array. The solid lines are the attenuation values input into the model. The synthetic waveforms are generated at 401 depth points, a depth decimation of 10 compared with field data. The frequency band of 2-4 kHz is used for attenuation estimation.

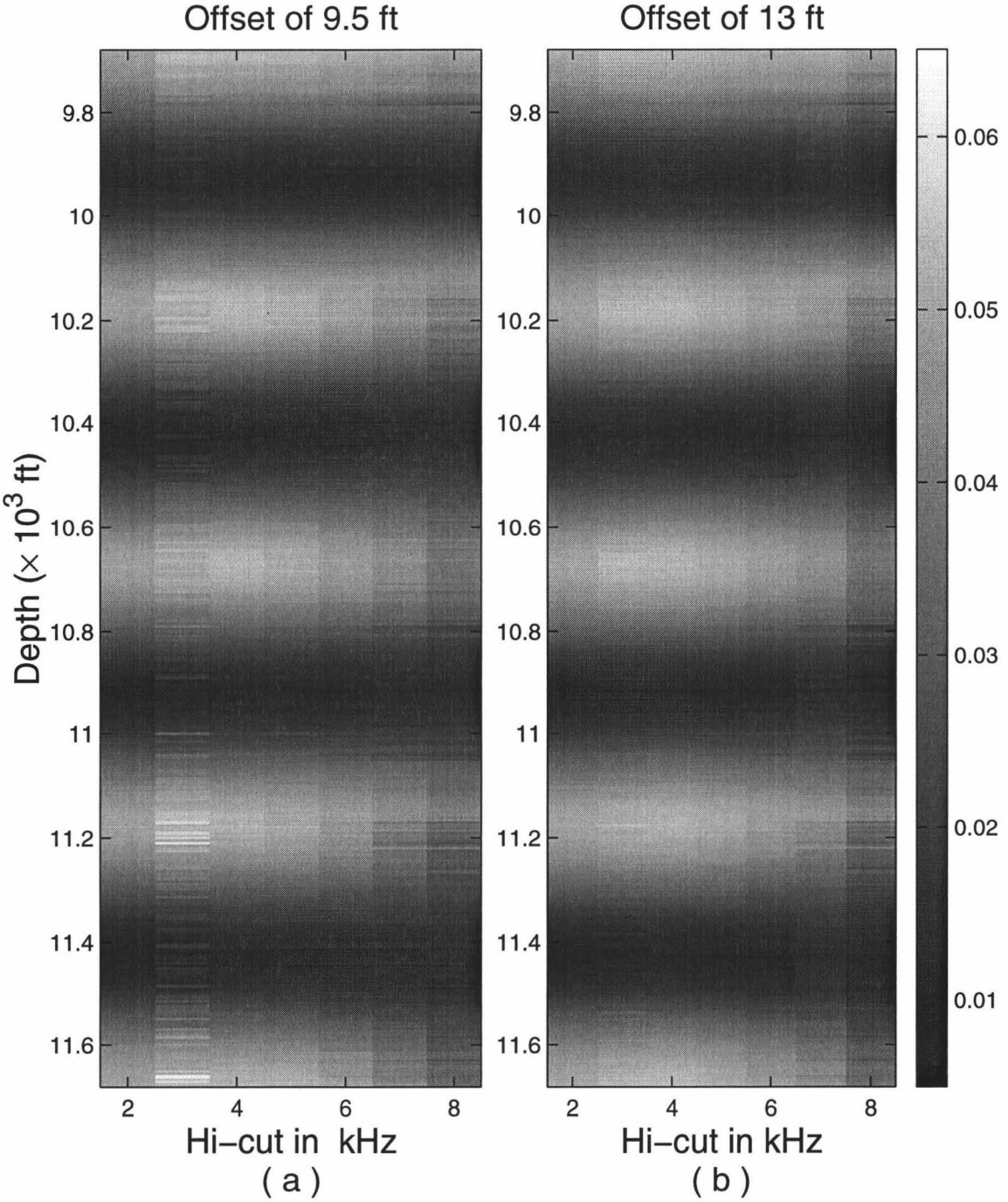

Figure 6.5: Attenuation profiles inverted from synthetic data in the bands 2-3 kHz, 2-4 kHz,..., 2-8 kHz. The result for each band is plotted above the upper limit of the band. The first column at 2 kHz is the attenuation input into the model.

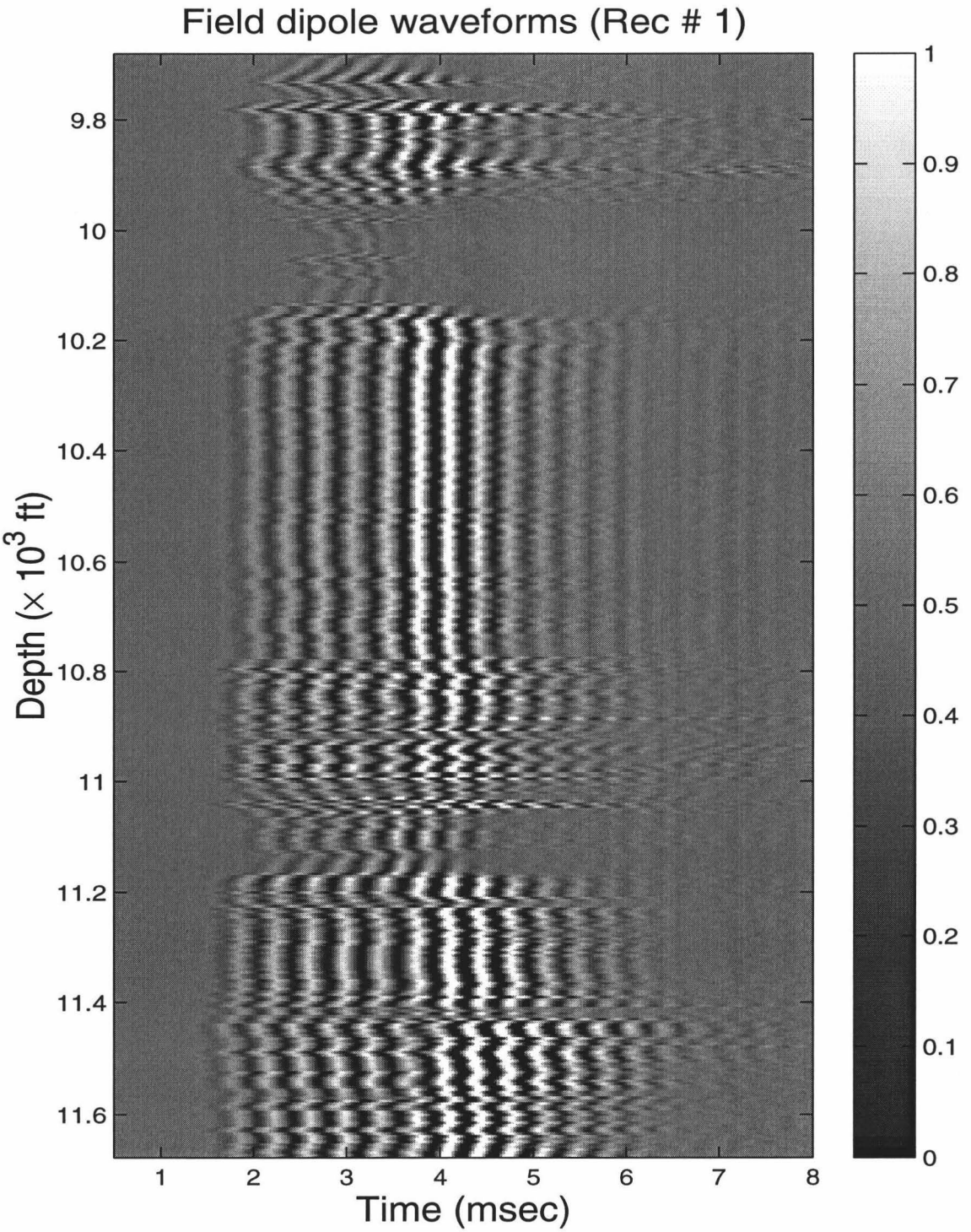

Figure 6.6: The field dipole waveform data set from receiver # 1, with every tenth trace plotted.

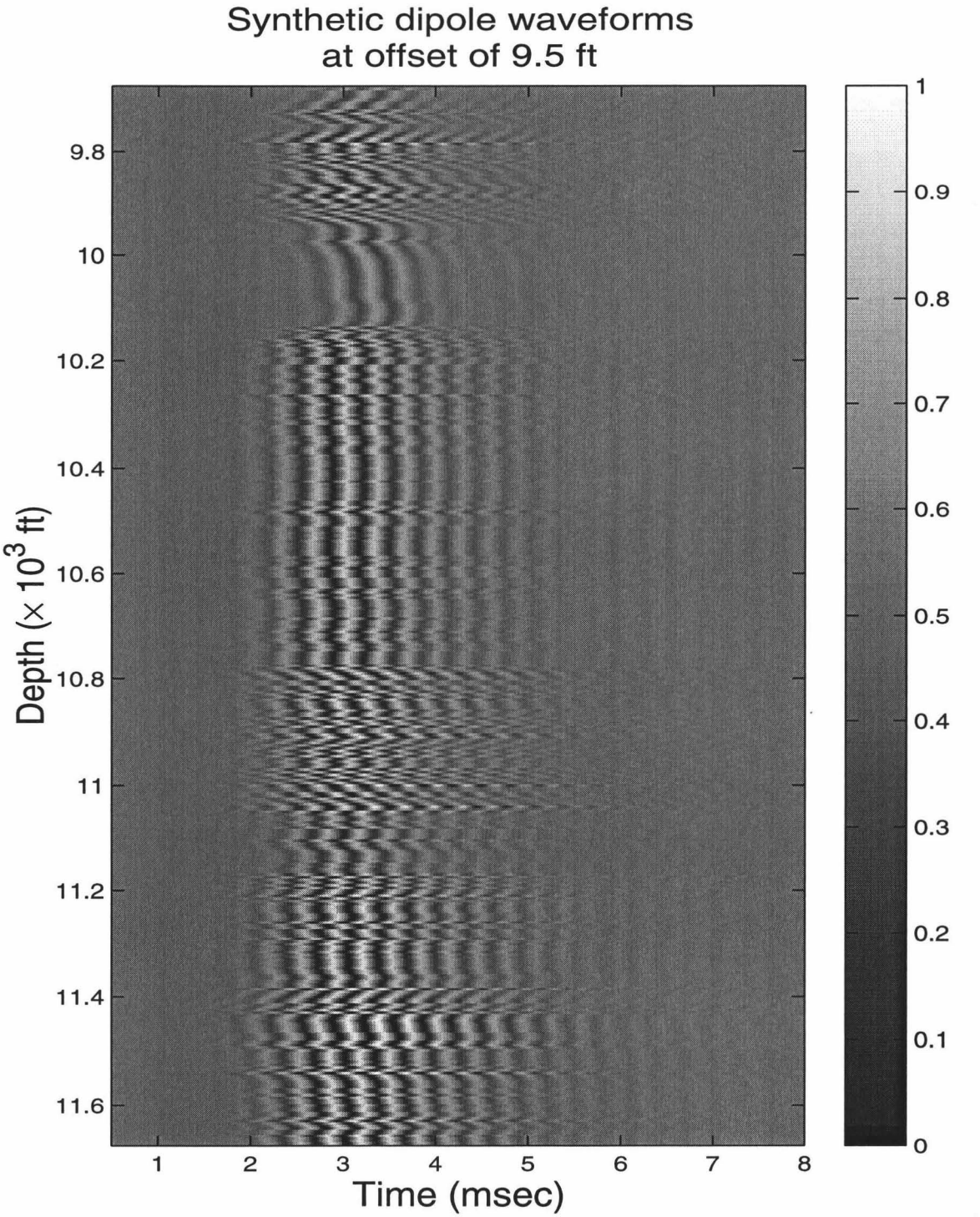

Figure 6.7: Zero-attenuation synthetic dipole waveforms at a source-receiver offset of 9.5 ft. Source was in the band 2–4 kHz.

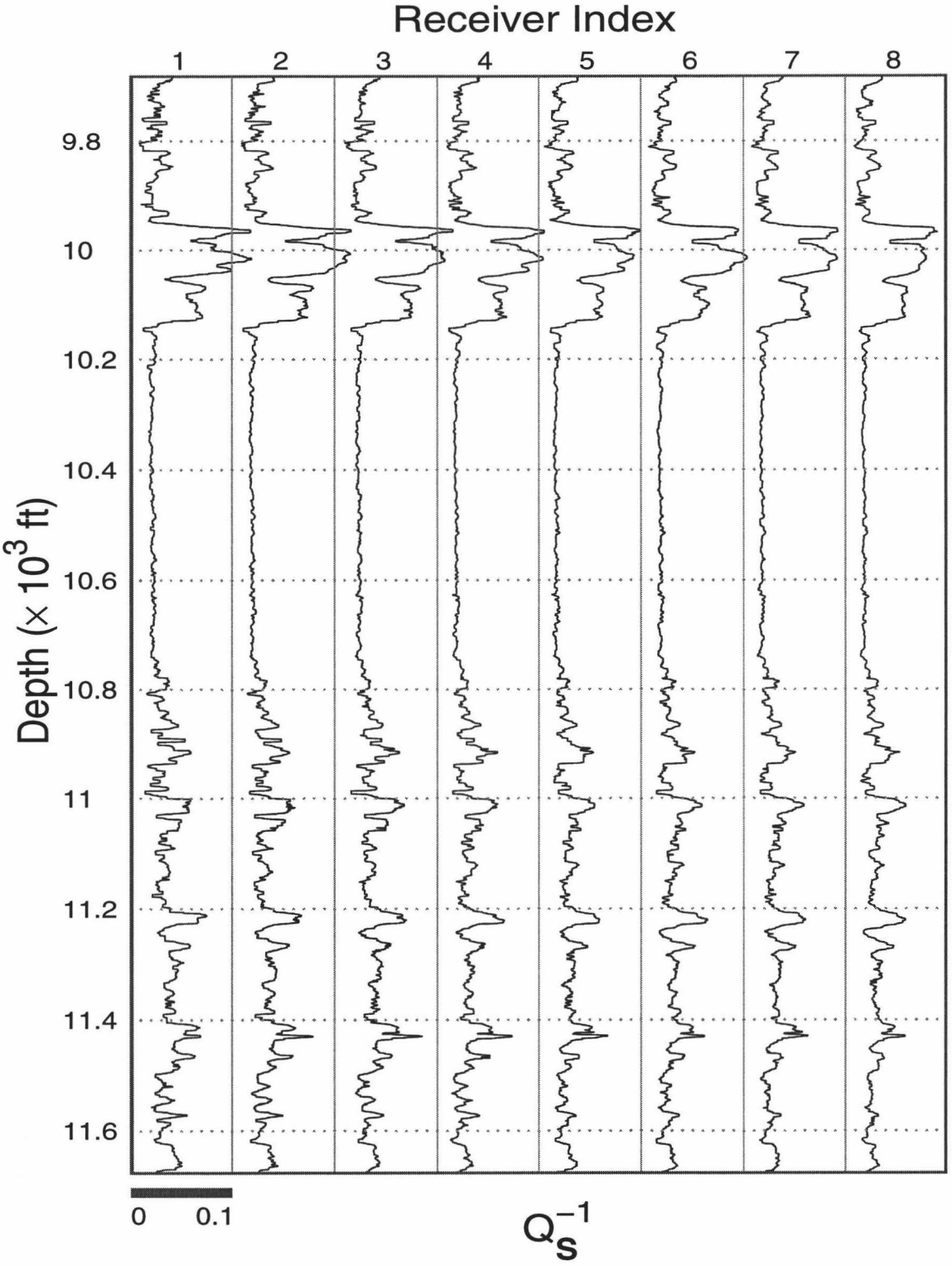

Figure 6.8: Eight S-wave attenuation profiles derived independently from each of the eight receiver field data sets.

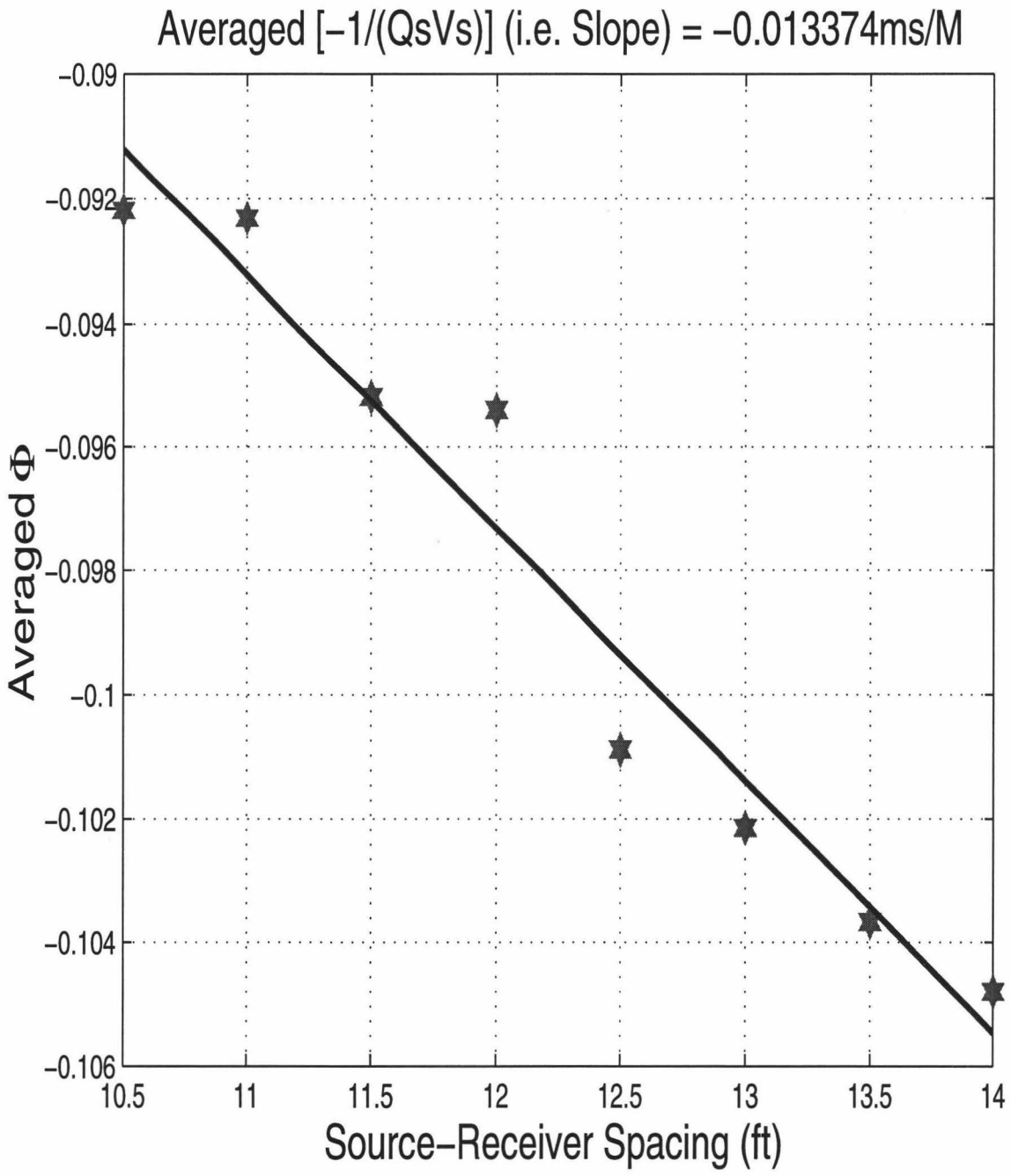

Figure 6.9: The mean value of $Q_S^{-1}(z)v_s^{-1}(z)$ over the depth range of 9680-11680 ft estimated from eight-receiver monopole waveform data. This value is used to correct the relative attenuation profile to absolute attenuation.

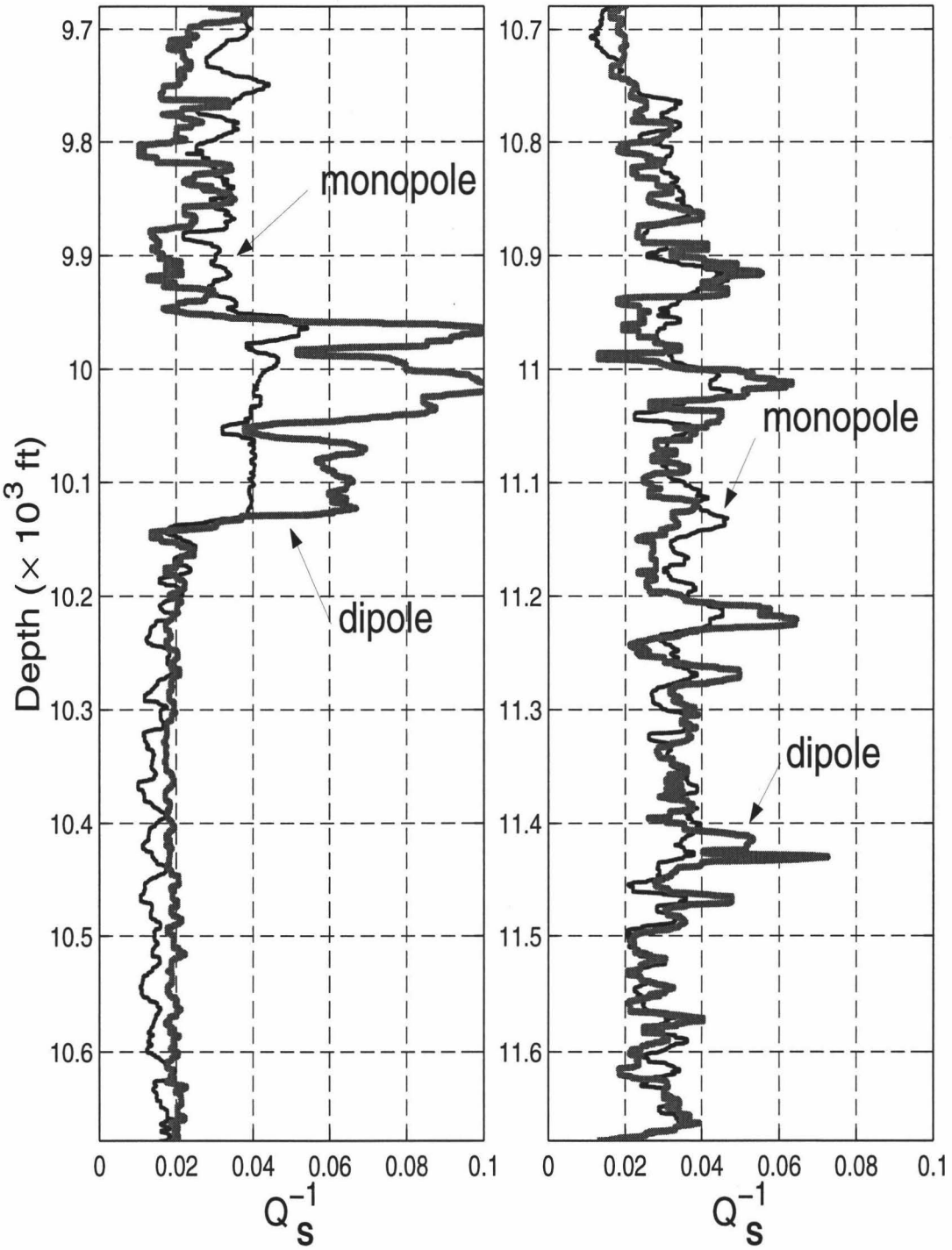

Figure 6.10: S-wave attenuation profiles from both monopole and dipole waveform data measured in the same well. The upper half depth range is shown in the left panel, and the lower part is shown in the right column.

6.7 REFERENCES

Aki K. and Richards, P. G., 1980, *Quantitative Seismology Theory and Methods*, W. H. Freeman and Company.

Cheng, C.H., Tang, X., Chundru, R., and Patterson, D., 1997, Analysis of formation shear wave anisotropy from cross-dipole acoustic logs, 3rd well logging symposium of Janpan processdings: Society of Professional Well Log Analysts, Japan, Chapter, 8p.

Cheng, C. H., Toksöz, M. N., and Wills, M. E., 1982, Determination of in situ attenuation from full waveform acoustic logs: *J. Geophys. Res.*, **87**, 5477-5484.

Cheng, C. H., Toksöz, M. N., and Willis, M. E., 1984, Reply to the comment on "Determination of in situ attenuation from full waveform acoustic logs: *J. Geophys. Res.*, **89**, 3400-3402.

Frazer, L. N., 1988, Quadrature of wavenumber integral, in Doornbos, D. J., Ed., SeismologicalAlgorithms: Academic Press Inc.

Frazer, L. N., Sun, X. H., and Wilkens, R. H., 1997, Changes in attenuation with depth in an ocean carbonate section: ODP sites 806 and 807, Ontong Java Plateau: *J. Geophys. Res.*, **102**, 2983-2997.

Kilmentos T., 1995, Attenuation of P- and S-waves as a method of distinguishing gas and condensate from oil and water: *Geophysics*, **60**, 447-458.

Kurkjian, A. L., 1986, Theoretical far-field radiation from a low-frequency horizontal point force in a vertical borehole, *Geophysics*, **51**, 930-939.

Kurkjian, A. L., and Chang, S. K., 1986, Acoustic multipoles in fluid-filled boreholes: *Geophysics*, **51**, 148-163.

Mallick, S. and Frazer, L. N., 1987, Practical aspects of reflectivity modeling: *Geophysics*, **52**, 1355-1364.

Schmitt, D.P., 1988, Shear wave logging in elastic formations: *J. Acoust Am*, **84**, 2215-2229.

Sun, X.H., X.M. Tang, and C.H. Cheng, 1999, *P*- and *S*-wave attenuation logs from sonic logging data, submitted to *Geophysics*.

Tang, X.M., and Chunduru, R.K., 1997, Inversion of shear-wave anisotropy from cross-dipole logging data-method and case studies, 67th Ann. Internat. Mtg., Soc. Expl. Geophys., Expanded Abstracts, 270-273.

Willis, M. E., and Toksöz, M. N., 1983, Automatic P and S velocity determination from full waveform digital acoustic logs, *Geophysics*, **48**, 1631-1644.